Nucleosynthesis in Common Envelope Accretion Disks: Probing the Mechanisms of Element Formation Around Neutron Stars

Alexander David Hall-Smith MPhys

PhD

The University of York
School of Physics, Engineering and Technology

December 2024

Abstract

This thesis will present the results from single zone Post Processed Nucleosynthesis simulations of Common Envelope accretion discs centred around either a neutron star to better understand the composition of the material that is produced and investigate the impact that different accretion rates, initial abundances and companion masses have on the resulting isotopic and element abundances. Accretion disks around neutron stars of mass $1.5\,\mathrm{M}_\odot$ and $2\,\mathrm{M}_\odot$ inside companion envelopes of $12\,\mathrm{M}_\odot$, $15\,\mathrm{M}_\odot$ and $20\,\mathrm{M}_\odot$ companions were analysed. This thesis will also present a comparison between post processing nucleosynthesis code reaction librararies, as well as a comparison between four different post processing nucleosynthesis codes for a range of different astrophysical environments.

Declaration of Intent

I, Alexander David Hall-Smith, declare that this thesis is a presentation of original work, and I am the soul author. This work has not previously presented for a degree or qualification at this university or elsewhere. All sources used in this work are acknowledged and appropriately referenced.

Contents

List of Figures

Chapter 1

Introduction and related physics

To simulate the nucleosynthesis inside a common envelope there is a wide variety of physics that must first be understood. This chapter explains the types of nuclear processes that may occur inside a common envelope and describes how to use nuclear physics to understand and simulate astrophysical objects.

1.1 Nuclear Physics in stars

1.1.1 Types of Nucleosynthesis

Stars maintain their shape and luminosity through a complex process of nuclear fusion and radioactive decay. Stars in the main sequence of the Hertzsprung-Russell diagram, like our sun, fuse hydrogen nuclei together to form helium or fuse hydrogen with carbon, nitrogen and oxygen in the CNO cycle. The temperature within the star dictates which process will dominate energy production, as shown in figure 1.1. Extreme environments, such as the accretion disk around a black hole or supernovae, reach temperatures in the Gigakelvin range, hundreds of times hotter than the core of our sun. When temperatures are in this extreme range different nuclear fusion processes can occur depending on the composition of the material and availability of neutrons, protons and α particles.

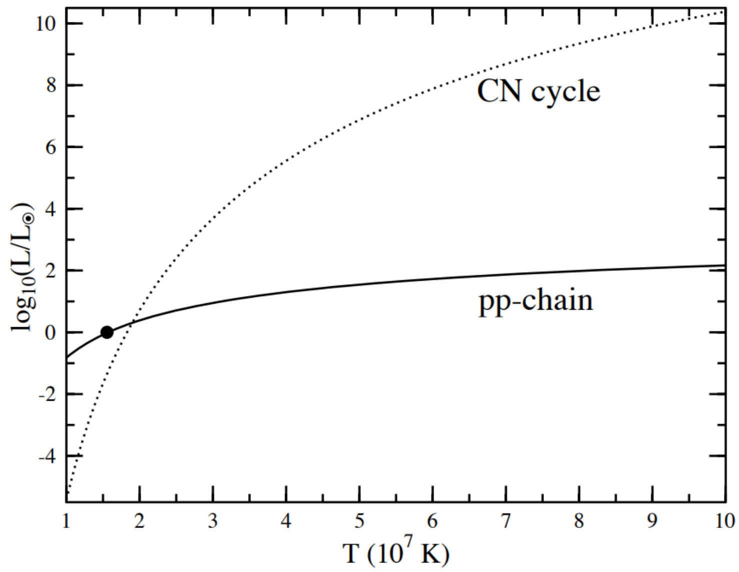

Figure 1.1: Energy production as a function of temperature for pp-chain and CNO nucleosynthesis. The dot signifies conditions in the solar core, taken from [2].

RP-process

In low temperature environments only a small fraction of available hydrogen will have enough energy to fuse with other low mass nuclei, and the resulting isotope will decay back to stability before another proton is able to fuse with the unstable nuclei.

The rapid proton capture process, known as the rp-process, occurs in environments with high temperatures, greater than 100 Megakelvin, and in material that contains a large fraction of hydrogen. This process follows a series of successive proton captures reaching isotopes near the proton drip line, then followed by fast β^+ decays with half-lives shorter than the proton capture rate. Due to the high flux of high energy protons the unstable nuclei with long half lives are not able to decay before fusing with another proton. This type of nucleosynthesis is believed to occur within X-ray bursts, as stated in [41] and [6], as this is process involves a neutron star accreting material from a companion where it falls to the neutron star surface and undergoes thermonuclear runaway. The rapid proton capture process ends in the tin tellurium cycle, as shown in figure 1.2, in which proton rich isotopes of tellurium (^{107}Te and ^{108}Te) decay via α particle emission to produce proton rich tin isotopes (^{103}Sn and ^{104}Sn) which then decay via β^+ emission. This produces isotopes of indium that follow proton captures and β^+ decays until it reaches tellurium and the process is then repeated.

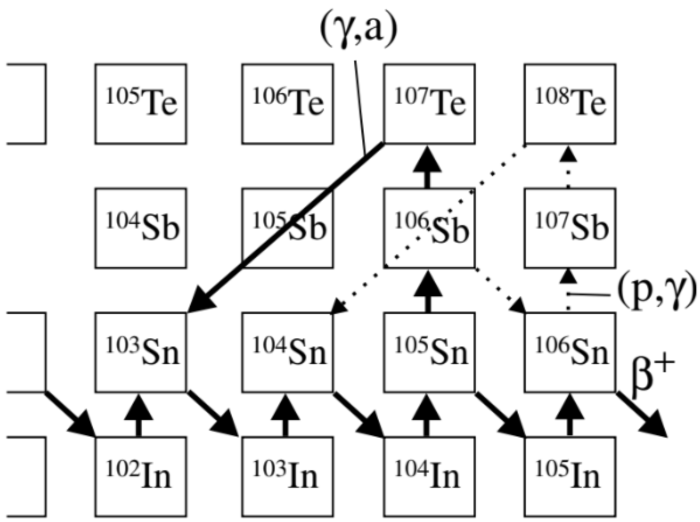

Figure 1.2: The tin tellurium cycle that ends the rapid proton capture process, The solid lines. Taken from [57]

The expected reaction pathways for the rp-process are shown in figure 1.3. This shows the reaction pathways that occur between hydrogen and krypton during rapid proton capture. It is important to note that the process does not just involve proton capture reactions, there are also α capture reactions that are important to the process. ^{18}Ne, ^{22}Mg and ^{30}S all undergo (α, p) reactions which are crucial for the rp-process to continue. ^{18}Ne is an important break out reaction from the hot CNO cycle, ^{22}Mg allows material to reach beyond the Ne, Na region and at low temperatures can delay the flow of material and ^{30}S has a beta decay half-life of 1.18 seconds meaning that at low temperatures it can limit the amount of material the flows to heavier elements. The initial composition of the material in figure 1.3 consists of mostly hydrogen as the study investigated hot hydrogen burning.

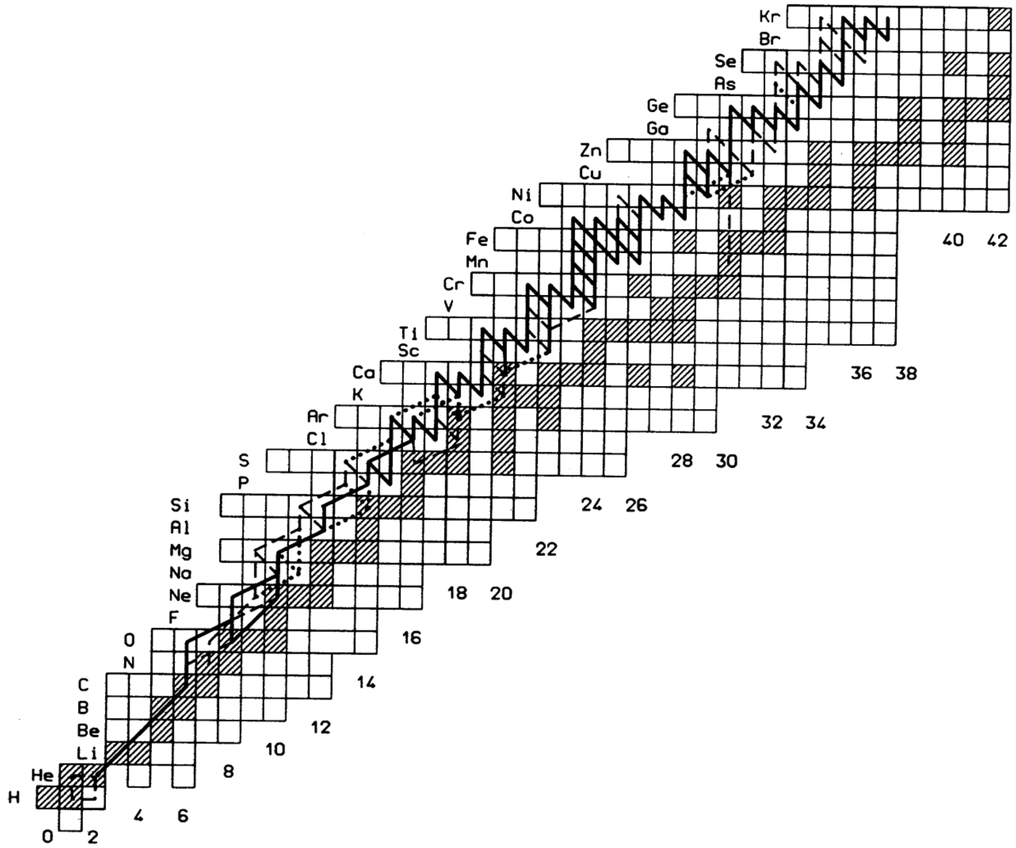

Figure 1.3: The full rp-process reaction chain for temperature T=1.5GK, density $\rho = 10^4$ g cm^{-3} and time t = 1000 seconds. Taken from [60].

α capture

If a main sequence star is nearing the end of its life it will transition into an Asymptotic Giant Branch (AGB) star. This means that the star begins fusing helium isotopes into carbon and oxygen. This requires much more energy to start, temperatures on the order of hundreds of Megakelvin are needed to trigger helium fusion, so this only occurs when the energy emitted from hydrogen fusion is no longer enough to sustain the stars shape, this causes the outer envelope to collapse towards the core, increasing the pressure inside the core and triggering helium fusion. The high temperature and density is required to overcome the coulomb separation between the α particle and the target nucleus. During α capture the isotopes produced can be unstable and decay back towards stability, if the density of α particles is high enough the unstable product can undergo α capture again before it decays back to stability.

S-process

The slow neutron capture process, also known as the s-process, can occur within low mass Asymptotic giant branch stars during thermal pulsation [40] or inside rotating massive stars [18]. These environments provide the right temperature range and neutron abundance for neutron capture reactions to occur slower than the subsequent beta decays. This produces isotopes near stability on the neutron rich side. The s-process only occurs inside environments with neutron densities of around $10^6 - 10^{11}$ cm^{-1} and is believed to synthesise approximately 50% of all observed elements heavier than iron. For the s-process to occur there needs to be mixing between the core with material from the surrounding helium envelope, this mixes neutrons produced by $^{13}\text{C}(\alpha, n)^{16}\text{O}$ (for AGB stars) or $^{22}\text{Ne}(\alpha, n)^{25}\text{Mg}$ (for massive stars) with the seed nuclei from the core. This process can occur for thousands of years during the lifetime of the star.

R-process

R-process nucleosynthesis typically occurs inside neutron rich environments and is identified by the rapid, successive capture of neutrons producing isotopes far into the neutron rich region of the nuclear chart. Unlike in the s-process the neutron captures occur faster than the β^- decays, producing isotopes close to the neutron drip line. For this to occur the neutron density must be extremely high, greater than 10^{20} cm^{-1}, and temperatures must be within the Gigakelvin range. Therefore, it is thought that this process can only occur inside compact object mergers. Gravitational wave observations conducted in [1] suggests that the r-process occurs inside neutron star mergers.

1.1.2 Reaction rates in the context of stars

Every star that we observe is primarily fuelled by nuclear fusion. During nuclear fusion nuclei of elements can collide to from new elements, releasing photons which interact with the surrounding material and eventually escape the bounds of the star to be observed. Astrophysicists trying to model the processes that can occur inside the star need to understand how the fusion of material occurs and what conditions are required. For this, reaction rates are measured in the lab or calculated using nuclear structure theory and combined to produce reaction rate tables. These tables dictate how a particular isotope will interact with any other isotope of interest at a particular temperature.

The interactions between two particles are dictated by the four fundamental forces, the strong force, the weak force, the electromagnetic force and the gravitational force. As the nuclei inside the star are in a plasma this means that there are no electrons in orbit around the nuclei, instead they travel through the plasma as free electrons. This removes the need to include the weak force when modelling two particle interactions. As well as this, the gravitational force does need to be considered as the affect of gravity between two nuclei is so small that it can be considered negligible. This leaves us with the strong nuclear force and the electromagnetic force to consider. At very small distances, less than 3 femtometres separation, the strong nuclear force causes the nuclei to be attracted to each other. However, at distances larger than this the positive charge of the two nuclei repel each other due to the electrostatic force, known as the Coulomb barrier.

To overcome this effect George Gamow proposed modelling the particles as a wave to understand the alpha decay that can be observed in naturally occurring radio nuclides [22]. This model was then adapted to investigate reactions between different particle species and quantum tunnelling is the solution to the coulomb barrier. Gamow calculated that the probability to penetrate the coulomb barrier is:

$$G(E) = exp^{-\frac{2\pi Z_1 Z_2 e^2}{hv}\sqrt{\frac{\mu}{2E}}} \tag{1.1}$$

Where Z_1 is the charge of one particle, Z_2 is the charge of the second, v is the relative velocity of the two particles, E is the energy of the two particles, e is the charge constant and h is planks constant. μ is the reduced mass of the two particles given by

$$\mu = \frac{m_1 m_2}{m_1 + m_2} \tag{1.2}$$

From equation (1.1) we can see that there is a dependence on the velocity of the particles. This can be assumed to be an ideal gas and will have a Maxwellian velocity distribution. Therefore, we can calculate the Gamow peak to be the product of the velocity distribution and the probability to penetrate the coulomb barrier, G(E).

During fission nuclei of heavy mass, radioactive isotopes break down to produce daughter nuclei and, depending on the reaction, either neutrons, protons, electrons or a combination of these.

1.2 What is Post Processing Nucleosynthesis

To identify different processes that are occurring inside different types of stars requires a combination of observation, experiments and theory. Post Processing nucleosynthesis codes are used to understand the internal process that can occur inside different astrophysical scenarios, specifically looking at the types of nucleosynthesis that can occur. This is a challenging task as each isotope that is being measured can have several methods of production and destruction, and networks inside PPN codes can range from a couple of hundred isotopes to several thousand. With respect to Common Envelope nucleosynthesis, PPN codes are being used to identify interesting and exotic isotopes of elements as this could be a new production site for elements that we can observe in our universe, but we don't currently know of their production sites. This can also be used to help identify the Common Envelope event as we can accurately observe stellar composition through spectroscopic analysis, so understanding the abundance ratios is important for identifying the neutron star common envelope.

Each PPN code is independently designed, and so the inner workings can often vary. However, they all follow the same basic method. Ordinary Differential Equations (ODEs) are created for each isotope to model how they can be produced or destroyed, depending on the temperature and density of the system at a particular time. As each isotope has multiple reactions that dictate the production/destruction a single ODE requires less computing power to calculate and accounts for the change in abundance of other isotopes. Then the ODEs are solved for each time-step, providing a new isotopic abundance for each time-step. As each code is independently developed different numerical solvers have been chosen to calculate the ODEs, the most common of which is the backward euler method, which uses the Newton-Raphson method to find the roots of the ODE. This method will be examined in further detail in chapter 4 along with the Bader-Deuflhard method and Gear's method.

To accurately model the nucleosynthesis that occurs inside a neutron star common envelope the input physics used in the PPN code must first be accurate. The main nuclear physics used in PPN codes are reaction rate tables. These dictate how a specific reaction to produce or destroy a specific isotope will vary as a function of temperature. Each reaction rate is not only dependent on the temperature of the system, but also on the mass and number density of the reactants involved. So for two isotopes i and j the reaction rate is given as:

$$R_{ij} = n_i n_j \langle \sigma v \rangle_{ij} \tag{1.3}$$

Where R_{ij} is the reaction rate, n_i and n_j are the number densities of isotopes i and j respectively and $\langle \sigma v \rangle_{ij}$ is the temperature dependant reaction cross-section between i and j. In PPN n_i and n_j are stated in the initial abundance or taken from the previously calculated time-step and the cross-section can be calculated by:

$$\langle \sigma v \rangle = \left(\frac{8}{\pi \mu} \right)^{1/2} \frac{1}{(kT)^{3/2}} \int_0^\infty \sigma(E)\, E\, e^{-E/kT}\, dE \tag{1.4}$$

Where E is the energy in the centre of mass system, σ(E) is the cross-section at energy E, T is the temperature of the system, k is the Boltzmann constant and μ is the reduced mass of the system, given in equation 1.2 [24] [52]. The cross-section at energy E, σ(E), can be determined both experimentally and through theory. Experimental measurements are compared with theoretical calculations and used to constrain optical model potentials and energy level densities, which then refine the theoretical calculations. Eventually theoretical models and experimental measurements can be combined to create an evaluated cross-section, which includes resonant effects that can influence the cross-section at different particle energies.

Reaction rates need to be measured accurately and the initial abundance of the scenario need to be found. Reaction rates can be measured experimentally and are further supplemented with theoretical rates for reactions that we cannot yet recreate in a laboratory condition. So it is important to ensure the reaction rate libraries are regularly updated with new physics. Accurate initial abundances can be taken from observation (for scenarios with progenitors that can be observed) or from stellar models of stable scenarios such as main sequence hydrogen burning or Asymptotic Giant Branch helium shell burning.

Chapter 2

Previous work investigating Neutron Star Common Envelope evolution

2.1 What are Common Envelopes?

The term common envelope was first used by [48] when discussing V471 Tau, a binary system in the Hyades cluster containing a $0.8\,\mathrm{M}_\odot$ white dwarf and a $0.8\,\mathrm{M}_\odot$ K-type main sequence (Referred to as a K-dwarf in the literature). He stated that this system may have originally been a long orbital period binary. The white dwarf was observed to be newly formed, meaning the progenitor had only recently left the main sequence and was originally a Red super giant of $2\,\mathrm{M}_\odot$ and $600\,\mathrm{R}_\odot$. For the two stars in the system to reach the close binary that was observed they must have undergone common envelope evolution, during which the orbiting compact cores of each star were heated due to the friction of the envelope. This dissipated the orbital energy into the envelope and brought the cores of the two stars much closer. He believed the end result to be a close binary located at the centre of a planetary nebula. Since this fundamental theory has been proposed the first neutron star-neutron star has been observed (GW170817). For this merger to occur within a Hubble time (the estimated lifetime of the current universe assuming constant expansion) the binary progenitor must have undergone a common envelope phase.
Common envelopes are a phase that can occur during a binary system's

lifetime when both stars orbit within a shared Common Envelope (CE). This is thought to be a precursor to neutron star mergers and Type 1a supernovae and an important evolutionary step in many binary systems [30]. If either star in a binary system expands past its Roche Lobe, such as expansion during the change from main sequence evolution towards the asymptotic giant branch, it will start to transfer material onto the surface of its companion. If the companion is sufficiently close this expansion and mass transfer can engulf the entire system in a single envelope of material.

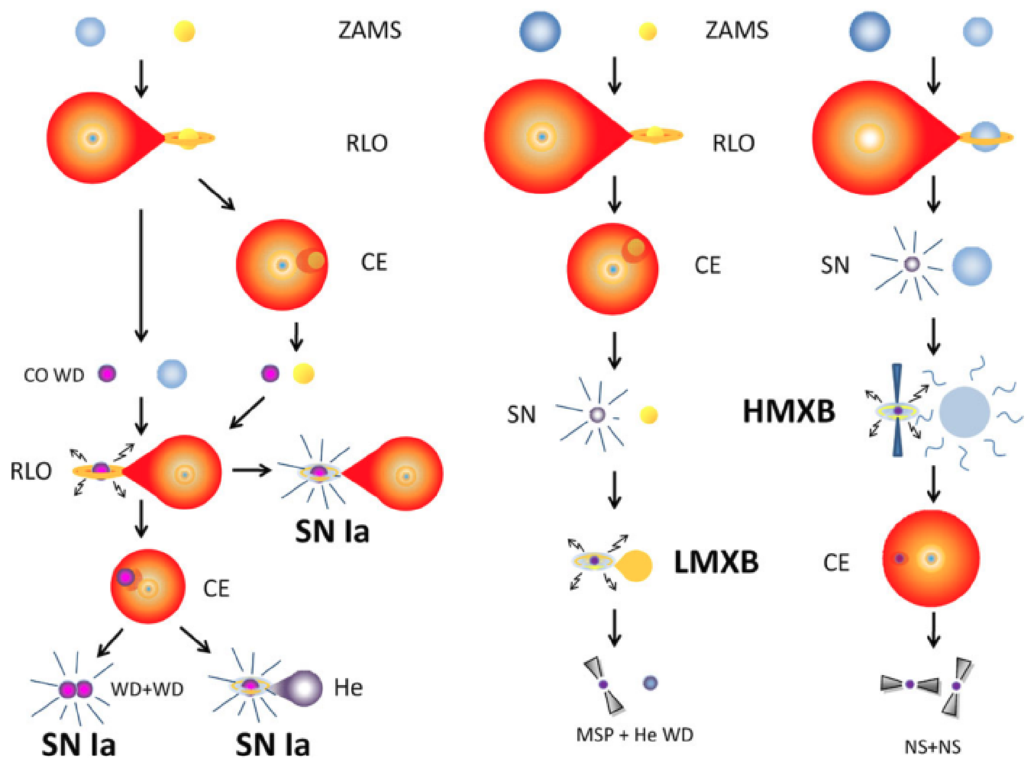

Figure 2.1: Different common envelope evolutions, taken from [28]. The final evolution Acronyms are as follows: ZAMS - Zero Age Main Sequence, RLO - Roche Lobe Overflow, CE - Common Envelope, SN - Super Nova, CO WD - Carbon Oxygen White Dwarf, HMXB - High Mass X-ray Binary, LMXB - Low Mass X-ray Binary, He - Helium star, MSP - Millisecond Pulsar.

CEs can form at many points during a binary systems evolution and do not always result in a compact binary system (such as a binary neutron star, a neutron star black hole binary or a binary black hole system) but can result in the compact remnant merging with the core of the companion. The recent observation of a neutron star merger with gravitational waves has highlighted the importance of understanding how the progenitor system has formed. For the neutron stars to merge within a Hubble time they must be separated by no more than $5R_{\odot}$, [8], and therefore there must have at least one common envelope event during the lifetime of the system to allow the stars to dissipate some of the orbital energy they carry and move closer to one another [16]. This work will investigate the nucleosynthesis that might occur inside the accretion disc that forms around the compact binary progenitor, looking at neutron stars of mass $1.5\,M_{\odot}$ and $2\,M_{\odot}$, orbiting in the envelope of giant phase $12\,M_{\odot}$, $15\,M_{\odot}$ and $20\,M_{\odot}$ companions.

During the CE phase the material from the companion does not fall directly onto the surface of the compact remnant but forms an accretion disk around the neutron star or black hole. This is due to the angular momentum carried by the accreted material as the compact remnant orbits through the envelope, [44]. As the material flows around the accretion disk it is subjected to high temperatures and pressures, which can trigger nucleosynthesis to occur inside the disk. As the material gets closer to the surface of the compact remnant the temperature and density climb higher into the Gigakelvin range, opening up new reaction channels, producing more exotic isotopes. However, due to the angular momentum carried by the material and the energy generated from nuclear fusion some material in the disk is ejected back into the rest of the envelope. It is this process that we aim to understand in more detail as the material that is not accreted onto the surface can then later be ejected into the Inter Stellar Medium (ISM) during the final ejection phase of the Giant star.

2.2 Previous study on NS CEE

The Common Envelope environment has been a system of interest over the past 50 years, since it was first used to explain the orbital period of the binary system V471 tau by [48]. In this groundbreaking paper Pacyzynski proposed that the change in orbital period was due friction between the white dwarf and the surrounding envelope. [19] looked at the outcomes of rapid infall of material onto a neutron star in an external medium. Two cases were examined, the first an atmosphere in pressure equilibrium above the surface of the neutron star, the second representing material freely falling from infinity. The system was then evolved using one and two-dimensional hydrodynamic codes, and it was concluded that these systems allow for hyper critical (otherwise known as "super Eddington") accretion to occur. This is due to the cooling effect from escaped neutrinos allowing the system to expel energy via neutrinos and not photons, decreasing the photon pressure on the accretion disc and allowing more material to fall towards the neutron star. This theory was then further developed in the context of hyper accreting black holes during gamma ray bursts, which has a similar driving mechanism as neutron stars or black holes during common envelope evolution. The study by [51] looks at steady state accretion in the form of a disk centred around a black hole of several solar masses. In this it was concluded that the neutrino cooling effect is dominant at distances bellow 10^8 cm away from the neutron star surface. Above this threshold energy released during accretion is trapped in the optically thick gas and the disk does not cool.

The work presented in this thesis is a continuation from [31], which looked at how different ejection methods impacted the abundance of material produced near the surface of the neutron star inside a common envelope. In this paper two different ejection methods were compared to investigate the impact they have on nucleosynthesis of material, as [19] concluded that some material would gain enough energy during infall to be ejected back into the surrounding medium and not settle onto the surface of the neutrons star. As the method of ejection was uncertain two models were compared at different stages of the common envelope evolution. The first looked at an instantaneous "bounce" where the accreted material is adiabatic and in free fall, then at a depth of 20 km away from the surface of the neutron star the material is ejected at escape velocity. The second method looks at a convective scenario where the material is in free fall until at a depth of 50 km from the neutron star surface, then a force is turned on that ejects the material. The temperature and density profiles were then run through a single zone post processing code and the resulting abundances showed that both proton rich and neutron rich nucleosynthesis can occur in the low z region, depending on the accretion rate and therefore dependent on the temperature and density of the chosen model.

With accreting neutron stars showing evidence for complex nucleosynthesis in [31] and the important hydrodynamic work conducted in [51] and [19] we can see that the accretion disk that forms inside the common envelope event is possibly a production site that can contribute to the galactic chemical evolution of the universe. However, the models investigated by [31] do not accurately model the flow of material in the accretion disk as this only looked at material in free fall. As the disk orbits the neutron star the angular momentum carried by the material in the disk will extend the time it takes for it to fall towards the surface.

2.3 Hydrodynamics and development of Neutron star Common Envelope trajectories

Figure 2.2 shows the path of the material investigated in this project. Material that is accreted into the surface of the neutron star is not of interest as it is trapped on the surface due to the extreme gravitational potential, so trajectories where material enters the accretion disk and passes close to the neutron star before being ejected back into the companion were studied.

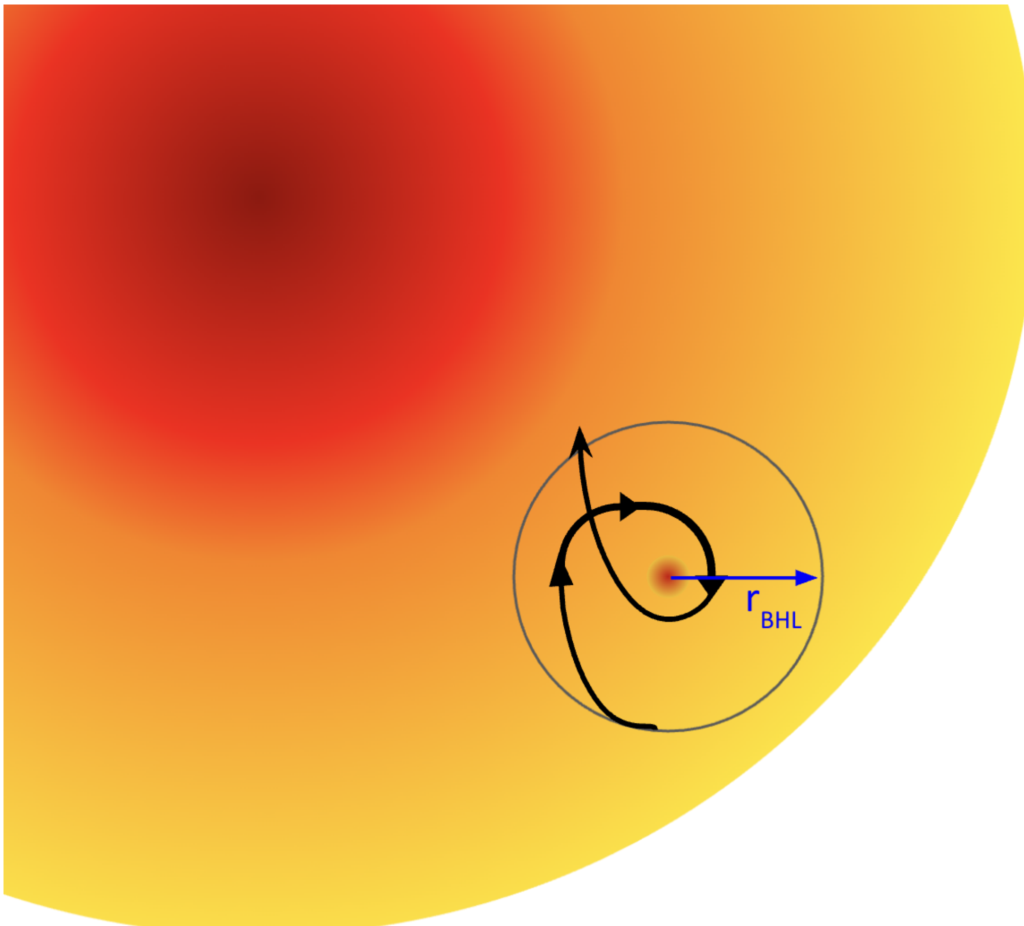

Figure 2.2: A cross-section of the neutron star common envelope showing the path of the material accreted from the companion towards the neutron star. r_{BHL} is the Bondi-Hoyle-Lyttleton radius of the accretion disk and the black arrows show the trajectory of the material around the neutron star before being mixed back into the companion envelope.

When a neutron star is engulfed in the expansion of a red giant companion there are many complex processes that dictate how material is accreted towards the neutron star. Following basic principles, as the neutron star enters the envelope of the companion the surrounding envelope is attracted to the compact object and flows towards the surface due to gravity. The accretion rate feeding the disk can be found using Bondi-Hoyle-Lyttleton equations [7]:

$$\dot{M}_{\rm BHL} = 4\pi r_{\rm BHL}^2 \rho (v^2 + c_s^2)^{1/2} \tag{2.1}$$

Where v is the speed of the neutron star relative to the envelope which will be similar to the orbital velocity of the neutron star, c_s is the speed of sound in the medium of the envelope, ρ is the density of the medium the neutron star is travelling through and $r_{\rm BHL}$ is the Bondi-Hoyle-Lyttleton in-fall radius, given by:

$$r_{\rm BHL} = \frac{GM_{\rm NS}}{(v^2 + c_s^2)} \tag{2.2}$$

$M_{\rm NS}$ is the mass of the Neutron star and G is the gravitational constant. Without the inclusion of angular momentum these equations only model material in free fall towards the surface of the neutron star, similar to the work done in [31]. [19] contains tabulated information of the infall rates and radii for a neutron star falling into different mass main sequence and AGB stars. The density and velocity gradient across the Bondi-radius leads to a net angular momentum inside the accreted material. This angular momentum drives the formation of a disk around the neutron star, which then in turn generates winds inside the disk which drive outflows, limiting the inflow. It is the outflows from the disk that can then mix with the surrounding envelope and later be ejected into the ISM and will be the main subject of investigation chapter 5.

[55] conducted hydrodynamic simulations of Bondi-Hoyle accretion in in-homogeneous mediums and developed a simple method of estimating the specific accretion angular momentum for wind fed X-ray sources. This approach can also be used for neutrons star common envelopes. To calculate the angular momentum, j_z, we can use the following:

$$j_z = \frac{\dot{J}_z}{\dot{M}_z} = \frac{1}{4}(6\epsilon_v - \epsilon_\rho)v \tag{2.3}$$

Where $\dot{J}_z$ is the angular momentum accretion rate (i.e. the amount of angular momentum transferred by the accreted material), $\dot{M}_z$ is the mass accretion rate and $\epsilon_{\rho,v}$ is the in-homogeneity parameter for the density and velocity:

$$\epsilon_{\rho,v} = \frac{r_{\mathrm{BHL}}}{H_{\rho,v}} \tag{2.4}$$

H_ρ is the scale height of the density and H_v is the scale height of the velocity. Using equations 2.1 to 2.4 we can obtain the angular momentum dependant accretion rate.

2.3.1 Developing CE trajectories

This process can be simplified into three stages; the in-fall of material, α-disk evolution and then outflow of material. During the in-fall phase the envelope material is assumed to be in free fall, accelerating due to the gravitational potential from the neutron star. During this phase the density of the material increases as a function of distance from the neutron star, $\rho_{\mathrm{infall}} \propto r^{-3}$. We assume the material is adiabatic and that radiation pressure dominates this phase. The entropy of the system is then:

$$S = \frac{T^3_{\mathrm{infall}}}{\rho_{\mathrm{infall}}} \tag{2.5}$$

Where T_{infall} is the temperature of the material. This phase will continue until the angular momentum provides enough support to equal the gravitational acceleration, at which point the material will form the accretion disk around the neutron star of radius r_{disk}.

$$r_{\mathrm{disk}} = j_z^2/(GM_{\mathrm{CO}}) \tag{2.6}$$

Depending on the common envelope scenario r_{disk} is between 10^7 cm and 10^9 cm from the neutron star surface. Once material has entered the disk it needs to lose angular momentum before it is able to accrete further towards the compact object. The viscosity of the disk is thought to be the main process through which angular momentum is dissipated, either through magnetic interactions or rotational instability, [10]. The α-disk assumption is standard practice for simulating viscous disks, representing viscosity as a constant value, α_{disk}. We take the α_{disk} solutions from [51] for our disk and use $\alpha_{\mathrm{disk}} = 0.01$ for our common envelope environment. Detailed disk calculations provide a range of values for α_{disk} dependent on the time and position throughout the disk. [51] provide a first order approximation for the disk conditions.

The outflows from the disk are driven by the viscous forces, however it is difficult to ascertain the amount of material that is ejected, with simulations showing ejecta in the range of a few percent of the total mass up to nearly complete ejection of the accreted material. It is also difficult to calculate where along the disk the most material is ejected, and so a grid of trajectories have been developed for each accretion rate with different inner radii reached before ejection due to the outflow wind. For the material to exit the disk it must reach the escape velocity, to simulate this two different wind models have been combined, an exponential and power-law evolution. A typical explosive supernova and r-process yield will result in either an accelerated ejection or free-streaming regime. As the ejecta is accelerated outward the density of the material will drop:

$$\rho = \rho_0 e^{\frac{-t}{\tau}} \tag{2.7}$$

Where ρ_0 is the initial density of the material, t is the time since ejection and τ is the dynamical timescale relative to the acceleration. Assuming constant entropy and assuming radiation pressure dominates during this phase the temperature, T, is found to be:

$$T = T_0 e^{\frac{-t}{3\tau}} \tag{2.8}$$

Where T_0 is the initial temperature. During the ejection we assume the material to move outwards with a constant velocity, following this assumption the temperature and density of the ejecta follow power law trajectories:

$$\rho = \rho_0 (t/\tau)^{-3}, \tag{2.9}$$

$$T = T_0 (t/\tau)^{-1} \tag{2.10}$$

Where τ is the expansion timescale, which is based on the velocity of the ejecta.

Figure 2.3 shows the temperature profile of the material as it proceeds through the accretion disk. The blue shows the material as it is in free fall towards the disk, the red section shows the period as the material orbits in the accretion disk, slowly falling towards the core. The green and yellow sections show the different winds that are turned on to eject the material.

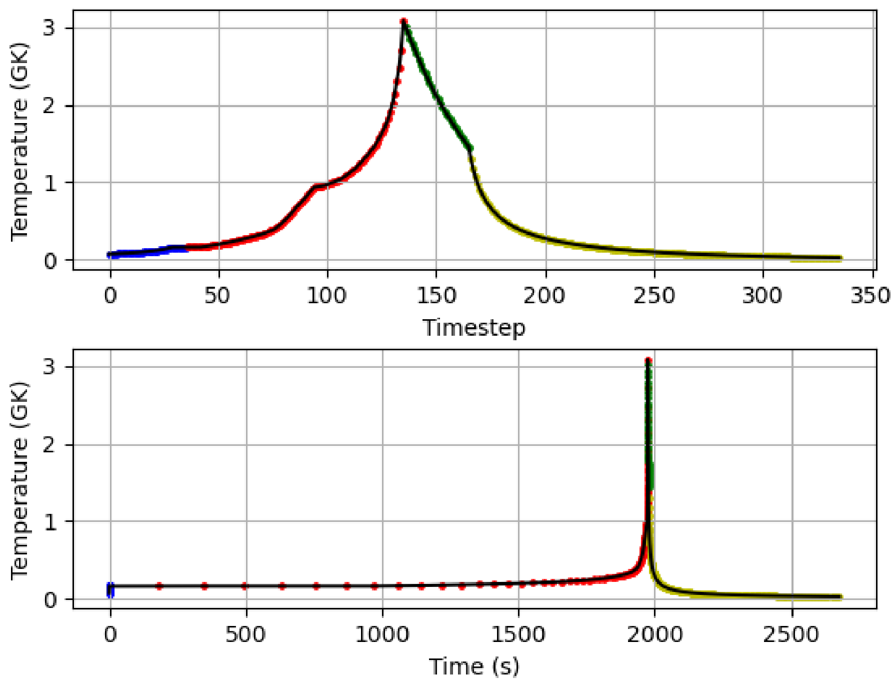

Figure 2.3: An example of the trajectories developed for this project. The top panel shows the temperature evolution of the system as time steps increase. The bottom panel shows the temperature evolution of the system as a function of time. This is for a $1.5M_{\odot}$ compact mass remnant with an accretion rate of $8 \times 10^{-5} M_{\odot} yr^{-1}$ and a minimum radius from the surface of the neutron star of 2.0355×10^{6} cm. The coloured points indicate which stage it is at. Blue indicates the period of free fall, red shows when α-disk evolution occurs, green shows the period of exponential ejection and yellow represents the power-law ejection.

Chapter 3

NuGrid reaction rate library comparison

This chapter will assess the impact of replacing outdated reaction rate libraries from NuGrid with current generation reaction rate data. The standard version of NuGrid still uses data published in 2001, since then many reactions have been experimentally recorded and refined and updated reaction libraries now contain more accurate reaction rate information.

3.1 Reaction rate libraries in the context of PPN

Post Processing Nuclear networks are used to simulate the nucleosynthesis that might occur in different stars and astrophysical scenarios. These consist of a network of isotopes that model the potential interactions at specific times, temperatures and densities along a hydrodynamic trajectory. To accurately model these interactions, temperature dependant reaction rates are stored in libraries. The information used in these libraries can come from a variety of sources such as the Joint Institute for Nuclear Astrophysics REACLIB [12] or STARLIB [56]. These are large compilations of reaction rates calculated using both experimental data and nuclear theory. Often PPN codes will use multiple different libraries to get a full range of interactions as one library my not cover the range of reaction types or the range of isotopes that need to be simulated. One example of a

PPN code that uses this technique is NuGrid.
NuGrid [49] is a privately developed software created by the NuGrid collaboration for the purpose of investigating hydrostatic burning, it has since been expanded to include explosive nucleosynthesis scenarios such as type 1a supernovae and core collapse supernovae. In NuGrid reaction rate information is mainly taken from the JINA Reaclib database [12]. It also contains supplementary reaction rate libraries from Iliadis 2001 proton capture study [27], NACRE [4] [63] and the Karlsruhe Astrophysical Database of Nucleosynthesis in Stars (KADoNiS) [15] as well as a custom-made reaction library labelled as VITAL which contains more complex reaction rates such as the triple α reaction or heavy isotope reactions like $^{16}O(^{16}O,p)^{31}Si$. Along with these particle interaction libraries, nuclear decay information such as branching ratios and decay probabilities are taken from [46] and [34].
The reaction flux data shown in [31] clearly shows evidence of proton and alpha capture reactions, pushing the path of material away from stability into the proton rich side of the nuclear chart. This area of experimental nuclear physics has been revolutionised in the past two decades, with radioactive ion beams being produced at facilities like Argonne National Laboratory with CARIBU, Vancouver's TRIUMF and ISOLDE at CERN. This has resulted in many new reaction rates being determined and published. As a result of these measurements the reaction libraries used in PPN software have become outdated, and the reaction cross-sections currently used in NuGrid are not up-to-date with the latest measurements and publications. To test the impact of these library changes four environments were investigated; a simple hydrostatic burn; a common envelope scenario; an X-ray burst trajectory; and an r-process like trajectory.

3.2 Updating the JINA Reaclib library

The NuGrid PPN code comes with the Joint Institute for Nuclear Astrophysics (JINA) Reaclib version 1.1, published on the 2^{nd} of April 2013, and contains 76,065 rates. JINA has released four more library compilations since Reaclib v1.1, the most recent of these is called the Default Reaclib library and was released on the 24^{th} of June 2021, and will be referred to as Reaclib 2021 from now on. Reaclib 2021 contains a total of 81,443 rates. Of these, 48,694 of these rates are taken from the same sources that Reaclib v1.1, 25,432 reaction rates have been updated to use data from publication between 2013 and 2020 and a further 7162 rates have been added to Reaclib 2021. Full details for the reaction data and the changes made between Reaclib v1.1 and Reaclib 2021 can be found at [12] 2,075 reaction rates that were in Reaclib v1.1 have been removed for Reaclib 2021. To understand the impact of these data changes each of the four test environments were simulated twice, once using the Reaclib v1.1 that comes as standard in NuGrid, and a second with the updated Reaclib 2021. A comparison between the final elemental mass fractions and isotopic mass fractions above 1×10^{-15} reveals the differences in the reaction libraries. The lower mass fraction limit of 1×10^{-15} was chosen as the contribution of isotopes below this limit can be considered negligible. This is equal to the convergence limit, so if predicted mass fractions are within 1×10^{-15} of the calculated mass fraction it is assumed to be correct, otherwise the time-step is split up into smaller increments and rerun.

3.2.1 Simple Hydrostatic Burn

The simple hydrostatic burn trajectory has a constant temperature of 55 MK, a constant density of 100 gcm^{-3} and a length of 38.5 years. This trajectory was run using solar mass fractions the initial composition of the material is 72.8% ^{1}H, 26.1% ^{4}He and the other 1.1% is made up of trace amounts of heavier seed nuclei.

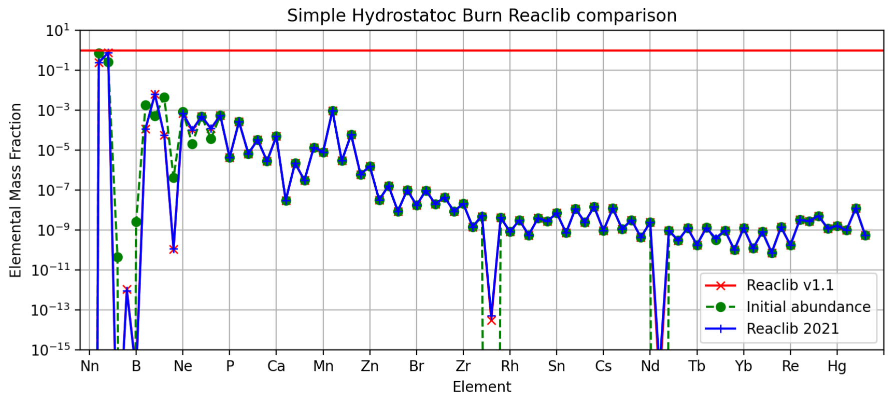

Figure 3.1: Final elemental abundances for the Simple hydrostatic burn trajectory. The blue crosses show the abundances produced when using updated Reaclib 2021, the red X's show the abundances as a result of using Reaclib version 1.1. The initial elemental abundance is represented by the green circles and dashed lines.

Figure 3.1 shows the final elemental abundances for the simple hydrostatic burn using both Reaclib v1.1 and Reaclib 2021. As this environment does not get hotter than 55MK the majority of the elements included in the initial abundance have the same final abundance and are unaffected over the course of the trajectory. As expected of a low temperature hydrogen rich environment the largest final mass fraction is helium, which is produced via a series of (p,α) reactions. There is also evidence of CNO nucleosynthesis, as ^{14}N is the waiting point of the CNO cycle the increase in ^{14}N and the decrease in both carbon and oxygen over the course of the trajectory are evident of nucleosynthesis in this region. From this figure there is no difference in elemental mass fraction when using Reaclib 2021 instead of Reaclib v1.1, this can be verified by examining the final isotopic mass fractions and comparing individual isotopic mass fractions.

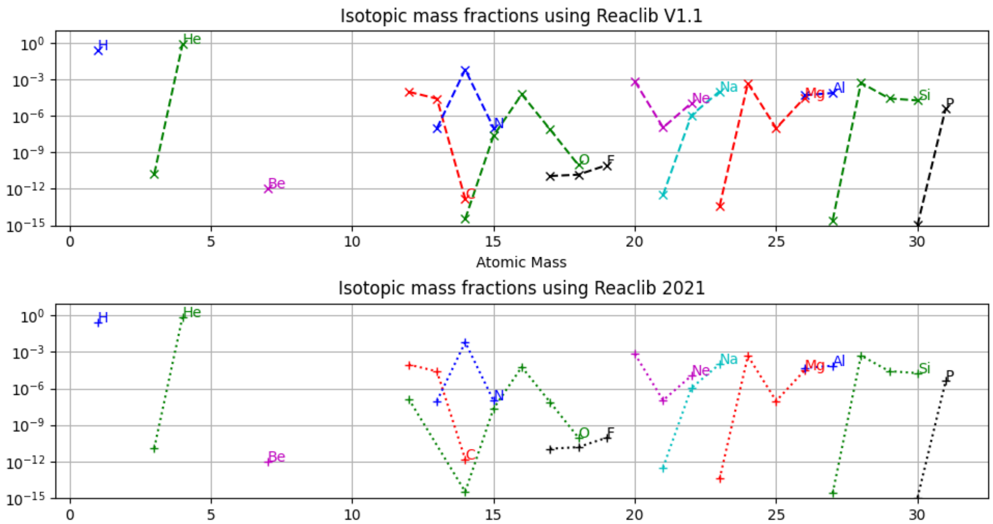

Figure 3.2: Final isotopic abundances for the Simple hydrostatic burn trajectory. The dashed lines show the abundances produced when using updated Reaclib version 1.1, the dotted lines show the abundances as a result of using Reaclib 2021.

Figure 3.2 shows the final isotopic mass fraction for the CNO region. When using Reaclib 2021 the abundance of ^{12}O is much larger than when using Reaclib 2021. The abundance of ^{12}O instantly jumps up to 5.322×10^{-11} after the first time-step and continues to grow until it reaches 1.374×10^{-7}. As this isotope is not included in the initial abundance and there are no expected reaction channels to produce this isotope in this environment and further investigation into the reaction flux shows no reactions producing ^{12}O, so it must be due to a computational error inside NuGrid. This abundance fraction is large enough to compete with the CNO isotopes that are produced and as ^{12}O is very proton rich and there are neutrons available it leads to (n, α) reactions and β decays back to stability.

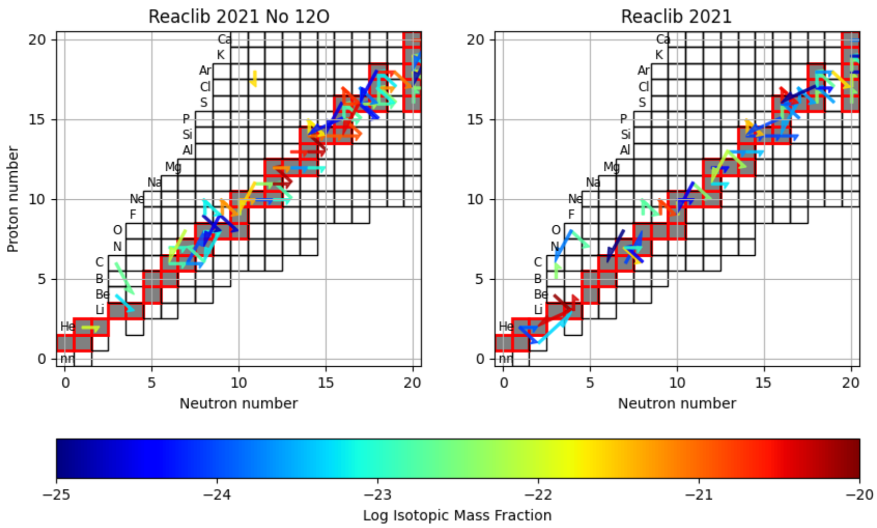

Figure 3.3: Reaction fluxes ($\frac{dY}{dt}$) for a simple hydrostatic burn using Reaclib 2021 with ^{12}O removed from the network (Left) and ^{12}O included in the network (Right). Limits of 1×10^{-25} to 1×10^{-20} have been placed to remove some of the strongest reactions and make the plot easier to read.

The neutrons used in destroying the ^{12}O are produced via two main reaction channels;

$$^{13}_{6}C + \alpha \longrightarrow ^{16}_{8} O + n \tag{3.1}$$

$$^{36}_{17}Cl + ^{2}_{1} H \longrightarrow ^{36}_{18} Ar + n \tag{3.2}$$

The neutron mass fraction produced from these reactions is small compared to the ^{12}O mass fraction, so most of the neutrons are destroyed via the ^{12}O(n,α)^{9}C. As these reactions still occur when ^{12}O is removed the reaction fluxes changes, as seen in figure 3.3. More neutron captures occur for isotopes just after the CNO region. For all subsequent reaction library tests and common envelope simulations ^{12}O was removed from the network.

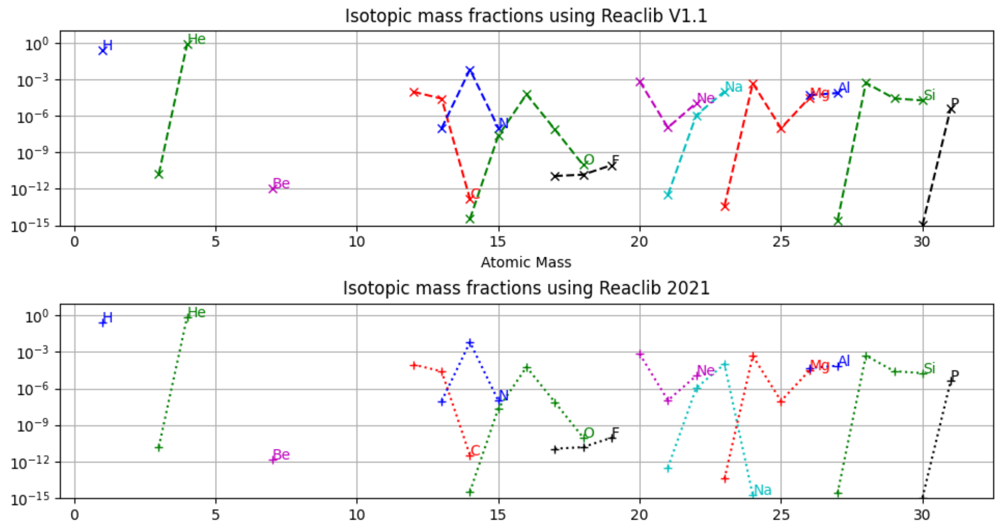

Figure 3.4: Final isotopic abundances for the Simple hydrostatic burn with ^{12}O removed from the network. The dashed lines show the abundances produced when using updated Reaclib version 1.1, the dotted lines show the abundances as a result of using Reaclib 2021.

The isotopic abundances for Reaclib without ^{12}O in the network are shown in figure 3.4. From this figure it is clear that the same mass fractions can be achieved for all the stable isotopes. The only difference that occurs when using Reaclib 2021 is a higher production of Na^{24}, this is because the neutron capture rate for ^{23}Na has been updated in Reaclib 2021 to include a low temperature resonance, increasing the production of ^{24}Na. As this isotope β decays to produce ^{24}Mg it will impact the Magnesium abundance, however the final mass fraction of ^{24}Na is only 8.196×10^{-15} and the final elemental mass fraction of Magnesium is 4.958×10^{-4} the contribution from ^{24}Na is negligible. Using Reaclib 2021 in place of Reaclib v1.1 provides the same elemental abundance distribution for a simple hydrostatic burn trajectory.

3.2.2 X-ray Burst

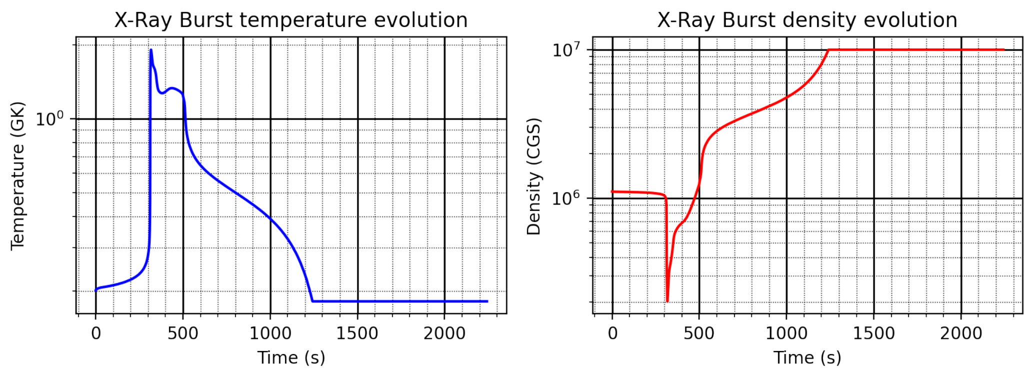

Figure 3.5: Temperature and density evolution for the X-ray burst trajectory.

The X-ray burst trajectory was taken from the SkyNet benchmarking publication [36]. The temperature and density evolution of the trajectory are shown in figure 3.5, with a peak temperature just under 2 GK, a peak density of 10^7 gcm^{-3} and a total length of 2243 seconds. The initial composition of the material is 88.7% ^{1}H, 11.2% ^{4}He with the other 0.1% consisting of seed nuclei.

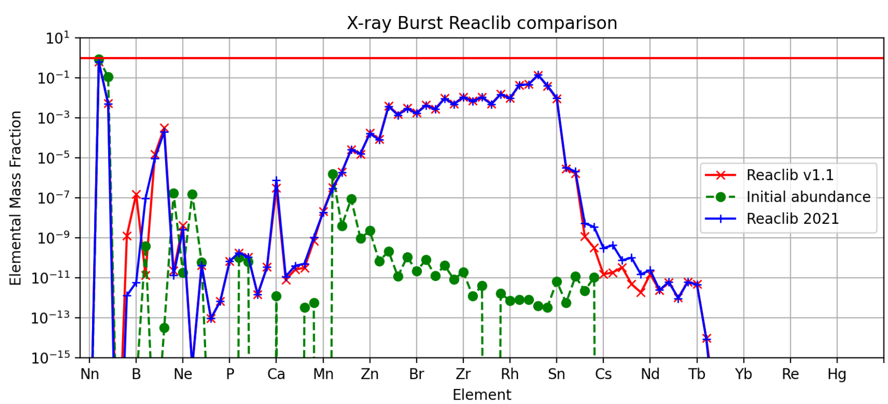

Figure 3.6: The elemental mass fraction distribution for an X-ray burst using both Reaclib v1.1 and Reaclib 2021, Similar to figure 3.2. The result from Reaclib 2021 is shown by the blue line, the result from Reaclib v1.1 is shown in red and the initial abundance is represented using the green dashed line.

Figure 3.6 shows the elemental mass fraction distribution at the end of the X-ray burst trajectory. Large differences of more than two orders of magnitude can be seen in the Beryllium and Boron mass fractions, where using Reaclib 2021 results in much lower mass fractions. The Boron mass fraction is made up of almost pure ^{8}B and is produced via proton capture on ^{7}Be. Less ^{7}Be is produced when using Reaclib 2021, and as a result less Boron is produced, as this library uses information from [13] for the ^{7}Li(p,n)^{7}Be and ^{7}Be(n,p)^{7}Li reactions. Inside Reaclib v1.1 this information is taken from [14] which uses theory to extend the reaction rate to astrophysically relevant energies. There is a large region between Nitrogen and Antimony where there is no difference in elemental mass fraction.

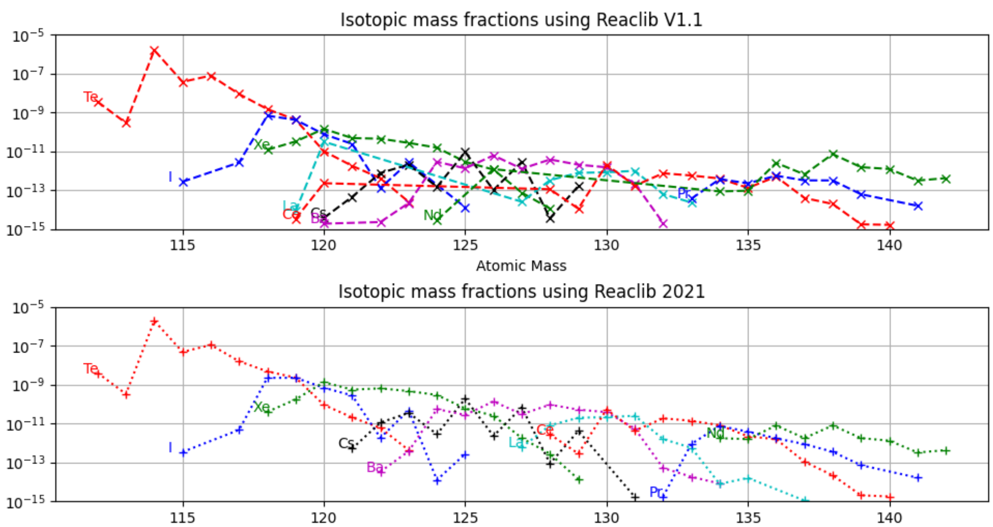

Figure 3.7: Final isotopic abundances for the X-ray burst trajectory in the region between Tellurium and Neodymium. The dashed lines show the abundances produced when using updated Reaclib version 1.1, the dotted lines show the abundances as a result of using Reaclib 2021. Different elements are shown using different colours.

There are substantial differences in elements between Iodine and Neodymium where Reaclib 2021 produces higher mass fractions. The final isotopic abundances shown in figure 3.7 show more proton rich isotopes of Caesium, Lanthanum, Cerium, Barium and Neodymium are produced with Reaclib v1.1 even though the total elemental mass fraction of these elements is lower. As this is a hydrogen rich environment, proton rich isotopes are expected to be produced, but they are very unstable, and therefore reaction information cannot be easily obtained through experiments. For both Reaclib 2021 and Reaclib v1.1 many of the reactions are calculated from theory rates, except for isotope decay information which is measured experimentally. The theoretical reaction rate data used in Reaclib 2021 has been revised and improved compared to Reaclib v1.1. For example the ^{26}Mg(p,n)^{26}Al rate is taken from [9] which was produced over 40 years ago in 1988, whereas the same rate in Reaclib 2021 uses [47] from 2011. Overall the final elemental mass fractions produced using Reaclib 2021 are very close to the results from Reaclib v1.1, however the updated fitting and newly included rates in Reaclib 2021 produce higher fractions of elements beyond the cadmium peak and the combination of theory and experimental data used in reactions producing and destroying ^{7}Be.

3.2.3 R-process environment

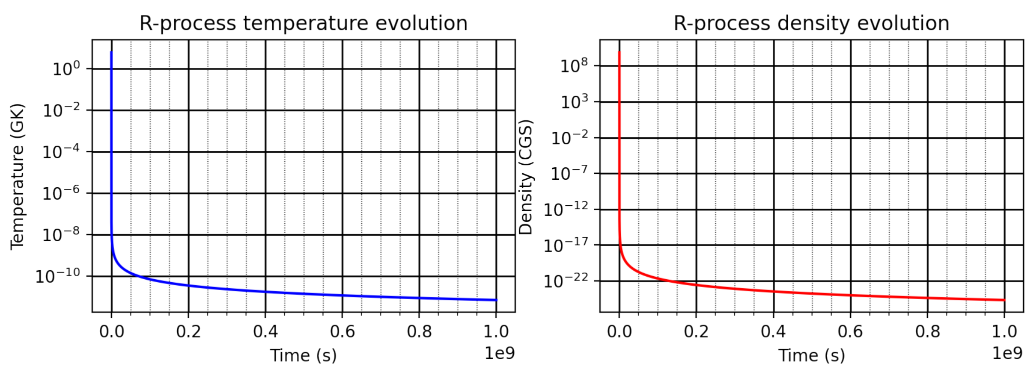

Figure 3.8: Temperature and density evolution for the r-process trajectory.

The temperature and density evolution for the r-process trajectory, again taken from the SkyNet benchmarking publication [36], are shown in figure 3.8. This follows the ejecta of a black hole-neutron star merger, with a high initial temperature and density that quickly cools as it expands. The initial composition consists of mostly neutrons, with an initial mass fraction of 99.9% neutrons and traces of other elements.

Figure 3.9 shows the final elemental mass fractions from the R-process trajectory taken from the SkyNet benchmarking publication [36].

Immediately it is clear that the result does not fit the expected mass fraction distribution for R-process nucleosynthesis. For R-process trajectories the initial abundance is composed mainly of neutrons and some seed nuclei, and the trajectory starts very hot and slowly cools. This leads to rapid neutron capture reactions, pushing the material towards the neutron drip line, followed by β^- decays back towards stability. During this process material forms high mass, neutron rich isotopes [43], [20] and [36].

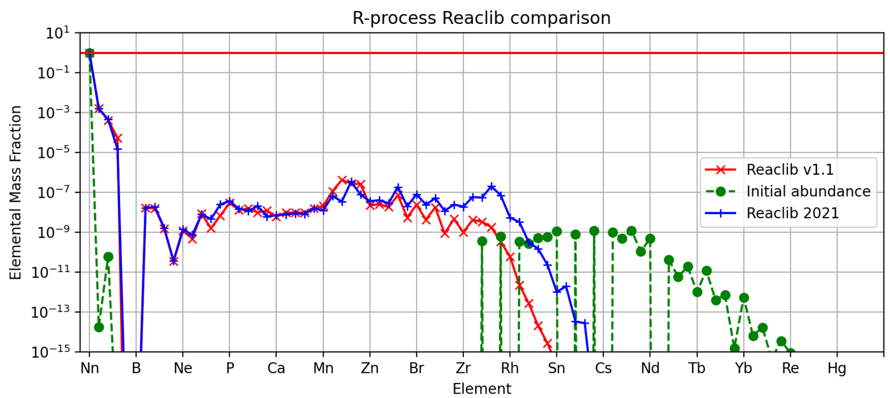

Figure 3.9: The elemental mass fraction distribution for an R-process like environment using both Reaclib v1.1 and Reaclib 2021, Similar to figure 3.2. The result from Reaclib 2021 is shown by the blue line, the result from Reaclib v1.1 is shown in red and the initial abundance is represented using the green dashed line.

As NuGrid has modelled this environment correctly it will not be used in further reaction library comparisons or PPN code comparisons. This is because the differences seen in figure 3.9 can not be directly attributed to the changes made in the reaction libraries. Before any further comparisons are made using the r-process trajectory the cause of this non-physical result must be understood and corrected.

3.2.4 Weak s-process

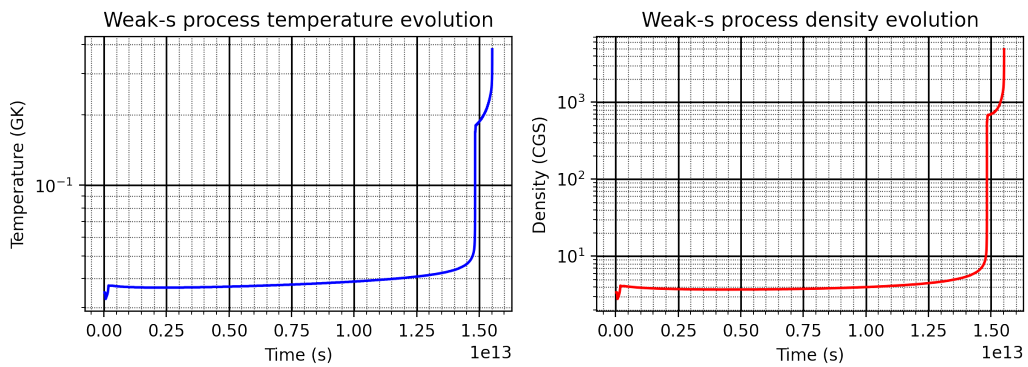

Figure 3.10: Temperature and density evolution for the weak s-process trajectory.

The weak s-process trajectory is taken from [45] and has been implemented into NuGrid as a test to ensure the network can repeatedly produce the expected resulting elemental and isotopic abundances produced in a slow neutron capture environment. The temperature and density evolution are shown in figure 3.10 and the initial composition of the material consists of 71.5% ^{1}H, 27.0% ^{4}He and 1.5% seed nuclei.

Comparing the results from the weak s-process environments probes the neutron capture and β^{-} decays close to the valley of stability. As the peak temperature of this trajectory is around 0.4 MK the nucleosynthesis that occurs in this environment follows closely to the valley of stability, most of these reactions have been determined experimentally as experiments recording reactions onto stable isotopes have been available since the 1950s [58]. Therefore, this environment is unlikely to produce large differences in isotopic or elemental mass fraction when using the different versions of Reaclib.

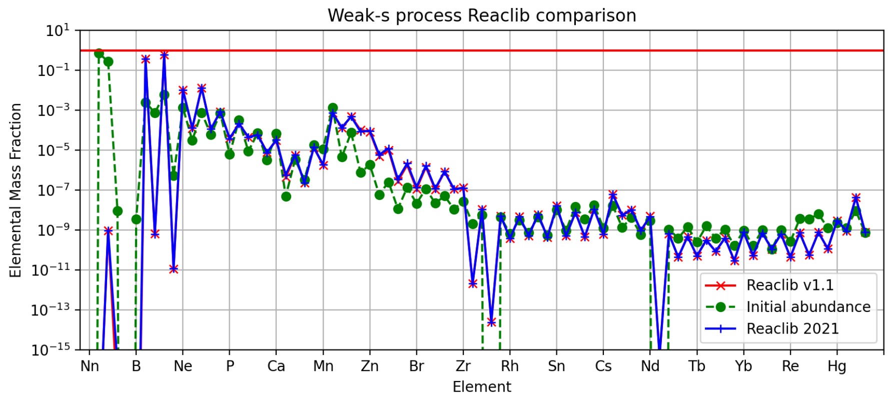

Figure 3.11: The resulting elemental mass fraction plots from using Reaclib v1.1, shown using red X's, and Reaclib 2021, shown using blue crosses. The initial abundance for both trajectories is shown using green dots.

Figure 3.11 shows the resulting mass fractions from each version of Reaclib, this is the second astrophysical environment to provide the same elemental mass fractions for both Reaclib 2021 and Reaclib v1.1. Further investigation into the reaction flux during the final time-step are shown in figure 3.12. This is the flux during the peak temperature of the trajectory, and it clearly shows the same reactions occurring at the same intensity in both runs. From this it is clear that using either reaction library will work for modelling slow neutron capture reactions close to stability.

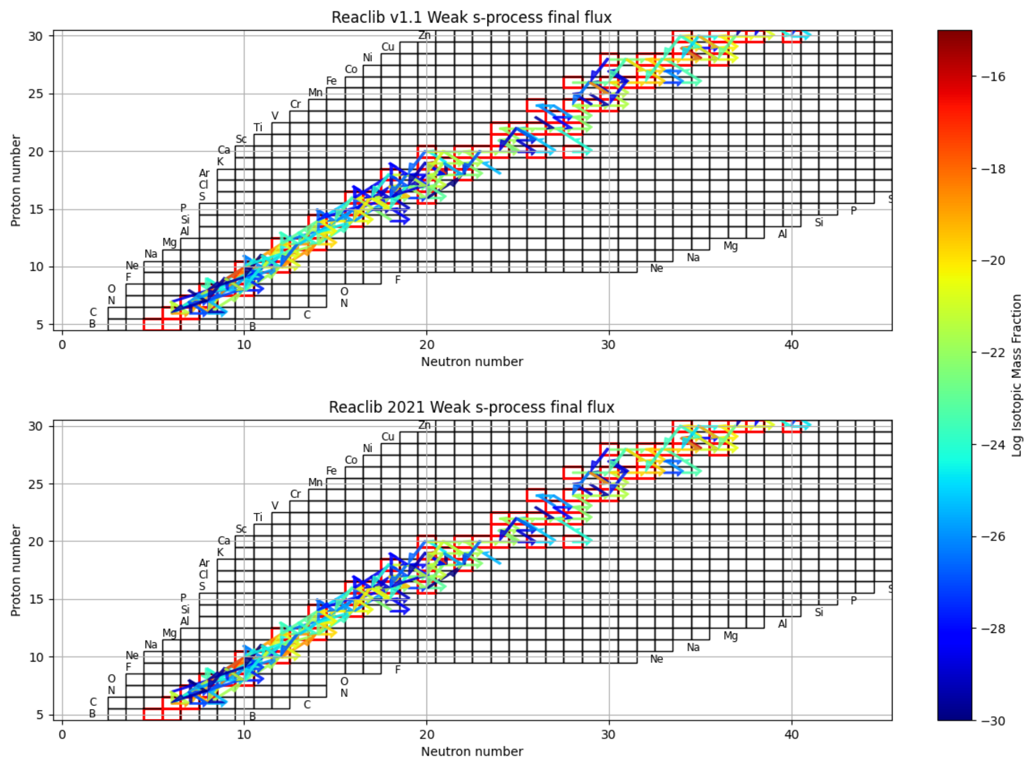

Figure 3.12: Reaction flux ($\frac{dY}{dt}$) for from the weak s-process environment using Reaclib v1.1 (Top) and Reaclib 2021 (Bottom). Stable isotopes are outlined in red.

3.2.5 Common envelope

As the common envelope phase can occur at different stages during a binary system evolution and the mass transfer process can vary as a result of many factors, it is not as well known with respect to the expected nucleosynthesis and resulting elemental or isotopic mass distribution. To best understand the impact updating the Reaclib library will have when simulating a common envelope environment two separate trajectories were investigated. The first trajectory has an accretion rate of $8 \times 10^{-5} \mathrm{M}_{\odot}\mathrm{s}^{-1}$ feeding the accretion disk and reaches distance of 2.5444×10^{6} cm from the neutron star surface before being ejected back into the envelope. The peak temperature reached by this trajectory is 2.2238 GK, similar temperatures are reached in all the trajectories with accretion rates lower than

$64 \times 10^{-5} M_{\odot} s^{-1}$ at varying inner radii. The second trajectory has an accretion rate of $128 \times 10^{-5} M_{\odot} s^{-1}$ and get to 1.0422×10^{6} cm from the neutron star surface. This trajectory was chosen as it has a much higher peak temperature of 8.7877 GK. The high accretion rate trajectories, $128 \times 10^{-5} - 1024 \times 10^{-5} M_{\odot} s^{-1}$, all reach similar temperatures. These two trajectories can be used to understand what the impact that updating the version of Reaclib can have on a broad range of trajectories while only looking at two specific peak temperatures. The initial abundance used in each trajectory is extracted from information regarding the separation and subsequent position of the neutron star inside the envelope and the composition of the material feeding the disk at that position.

Common envelope with $8 \times 10^{-5} M_{\odot} s^{-1}$ accretion rate

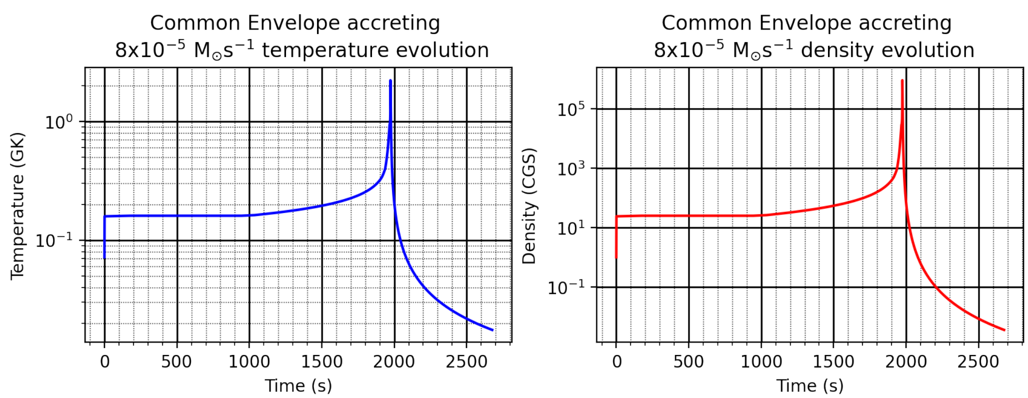

Figure 3.13: Temperature and density evolution for the common envelope accreting $8 \times 10^{-5} M_{\odot} s^{-1}$ trajectory.

The temperature and density evolution for the $8 \times 10^{-5} M_{\odot} s^{-1}$ accretion rate common envelope trajectory is shown in figure 3.13 and shows a peak temperature of 2.1 GK. The initial composition of the material is shown in green in figure 3.14. The initial composition consists of 97.8% ^{4}He. The full details of how the initial compositions were calculated are given in chapter 5.

The final elemental abundances of the $8 \times 10^{-5} M_{\odot} s^{-1}$ accretion rate common envelope trajectory are shown in figure 3.14. Like with the weak s-process trajectory, the final elemental mass fractions from using Reaclib

2021 are the same as those produced using Reaclib v1.1. This indicates that the updated reaction rate information used in Reaclib 2021 does not change the reaction channels used or the rate of nucleosynthesis through these reaction pathways. For some reactions along stability the same reaction rate is used as there have not been any changes for these stable isotope reactions since the release of Reaclib v1.1.

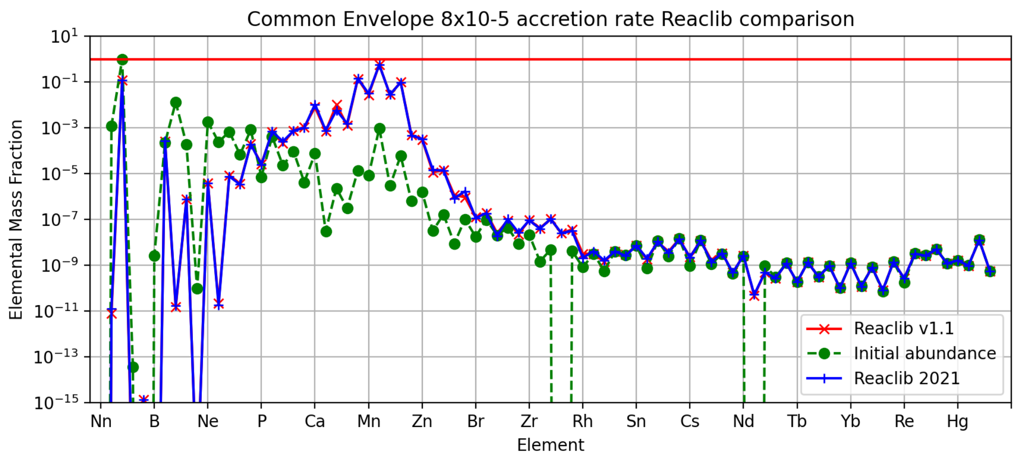

Figure 3.14: Final elemental abundances for a common envelope with $8 \times 10^{-5} M_{\odot} s^{-1}$ accretion rate. Results from Reaclib v1.1 are shown in red, results from Reaclib 2021 are shown in blue and the initial abundance used for both is shown in green.

The reaction flux at the peak temperature is shown in figure 3.15. The main production mechanisms that occur inside the common envelope at this accretion rate and inner radius are alpha and proton capture reactions. At this temperature and density the differences in Reaclib 2021 and Reaclib v1.1 do not impact the nucleosynthesis that is occurring. There are some minor differences in the magnitude of the reaction flux, For example the ^{44}Ti(p, γ)^{45}V reaction is slightly weaker when using Reaclib 2021 and the inverse reaction is not active. However, when using Reaclib v1.1 the ^{44}Ti(p, γ)^{45}V and ^{45}V(γ, p)^{44}Ti reactions are in equilibrium. This is what causes the slightly higher titanium mass fraction when using Reaclib v1.1 that can be seen in figure 3.14. While there are some differences in the resulting elemental mass fractions the impact of changing the Reaclib version does not significantly change the result but for longer trajectories or larger time periods this may lead to differing results.

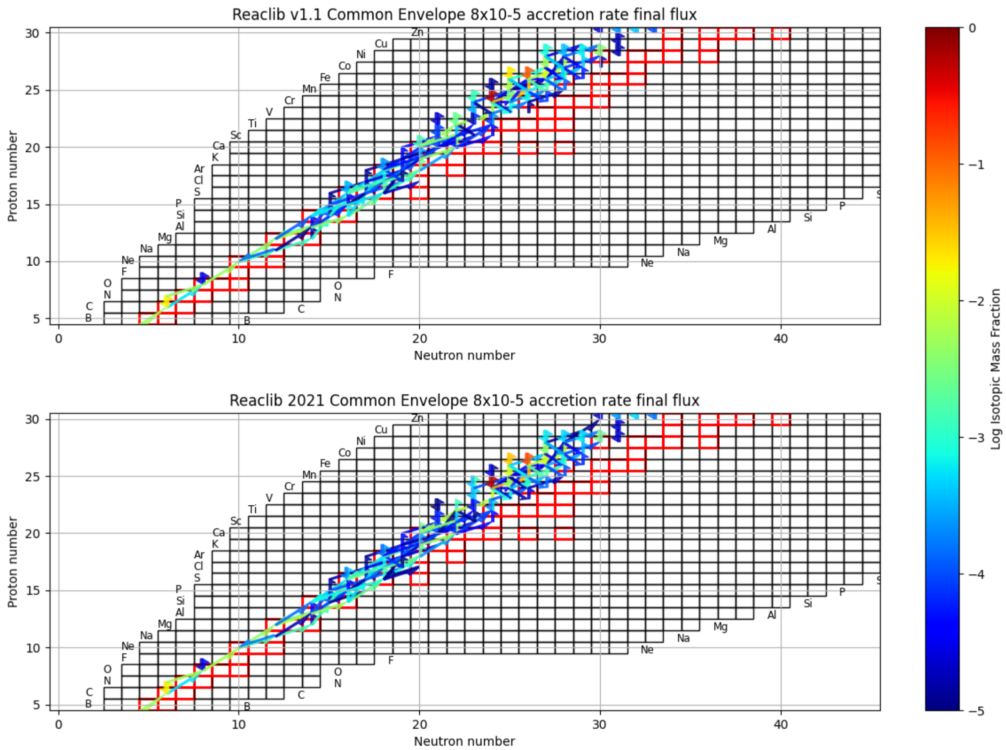

Figure 3.15: Nucleosynthetic flux ($\frac{dY}{dt}$) for a common envelope with $8 \times 10^{-5} M_{\odot} s^{-1}$ accretion rate during the peak temperature (2.2GK). The flux from using Reaclib v1.1 is shown in the top figure, flux from using Reaclib 2021 is shown in the bottom figure.

Common Envelope with $128 \times 10^{-5}\mathrm{M}_{\odot}\mathrm{s}^{-1}$ accretion rate

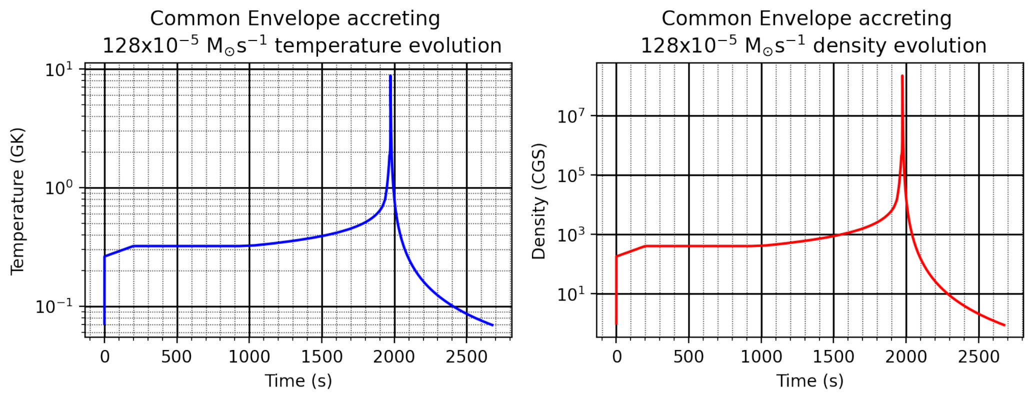

Figure 3.16: Temperature and density evolution for the common envelope accreting $128 \times 10^{-5}\mathrm{M}_{\odot}\mathrm{s}^{-1}$ trajectory.

The temperature and density evolution for the common envelope accreting $128 \times 10^{-5}\mathrm{M}_{\odot}\mathrm{s}^{-1}$ are shown in figure 3.16. This trajectory has a peak temperature of 9 GK, well within the NSE temperature range. The initial elemental mass fractions of the material are shown in figure 3.17, this uses a solar initial mass fractions, like in the simple hydrostatic burn case, with an initial composition of 72.8% ^{1}H, 26.1% ^{4}He and the other 1.1% is made up of trace amounts of heavier seed nuclei.

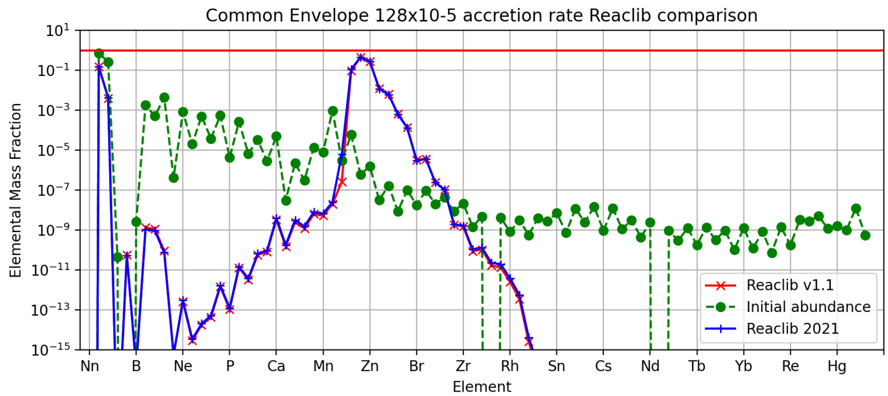

Figure 3.17: Final elemental mass fractions for the common envelope with $128 \times 10^{-5} M_{\odot} s^{-1}$ accretion rate. Results from Reaclib v1.1 are shown in red and the results from Reaclib 2021 are shown in blue. The initial abundance used in both runs is shown in green.

This higher accretion rate trajectory has a peak temperature of 8.7 GK, reaching Nuclear Statistical Equilibrium (NSE) temperatures. Figure 3.17 shows the final elemental mass fractions using both versions of Reaclib. Like the previous Common envelope trajectory, there is very good agreement in the results from both Reaclib v1.1 and Reaclib 2021 for almost all elements. However, when using Reaclib 2021, the final mass fraction of Cobalt is over an order of magnitude higher than the mass fraction produced using Reaclib v1.1.

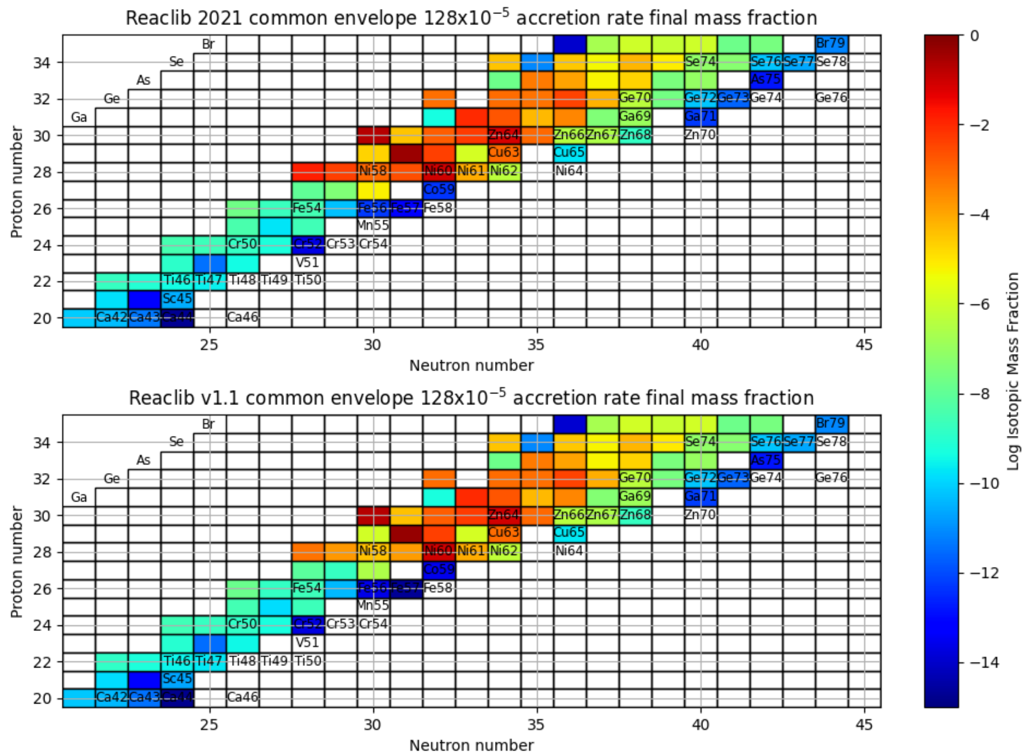

Figure 3.18: Final isotopic mass fractions for a common envelope with $128 \times 10^{-5} M_{\odot} s^{-1}$ accretion rate. Results from Reaclib v1.1 are top, results from Reaclib 2021 are bottom. Stable isotopes are labelled.

Further investigation into the individual isotopic mass fractions for the Iron peak elements is shown in figure 3.18 and reveals that the distribution of mass around the Iron peak is not the same for both reaction libraries. When using Reaclib 2021 the final ^{57}Co mass fraction is 24.8 times larger than the ^{57}Co mass fraction produced using Reaclib v1.1. The main contribution to the increased ^{57}Co mass fraction is the ^{57}Fe(p,n)^{57}Co, however in Reaclib v1.1 the ^{57}Co(p,α)^{54}Fe is much stronger, destroying more of the ^{57}Co and leading to a larger difference in mass fraction. Further investigation into the reaction flux shows that the difference is not due to a single reaction rate change, but stems from a variety of different reaction channels being used as a result of different isotopic mass fractions at the peak temperature. As the strength of each reaction varies as a result of isotopic mass fraction the slight differences in the isotopic masses that occur as the temperature slowly increases up to 8.7 GK result in the different reaction pathways that are shown in figure 3.19. In Reaclib 2021 many of the rates that were used in Reaclib v1.1 are still included but have been refitted to avoid non-physical behaviour. Reaclib 2021 also includes shell model calculations for reactions far from stability in the proton rich region of the nuclear chart. The combination of these changes lead to different reaction channels being used.

This trajectory highlights some of the problems that can occur when using older reaction libraries to model high temperature and density astrophysical environments. While the resulting elemental mass fractions are very similar the isotopic composition of the material is quite different. To ensure all high temperature scenarios are being modelled as accurately as possible the Reaclib 2021 reaction rate library will be the default choice and all further results will be calculated using this.

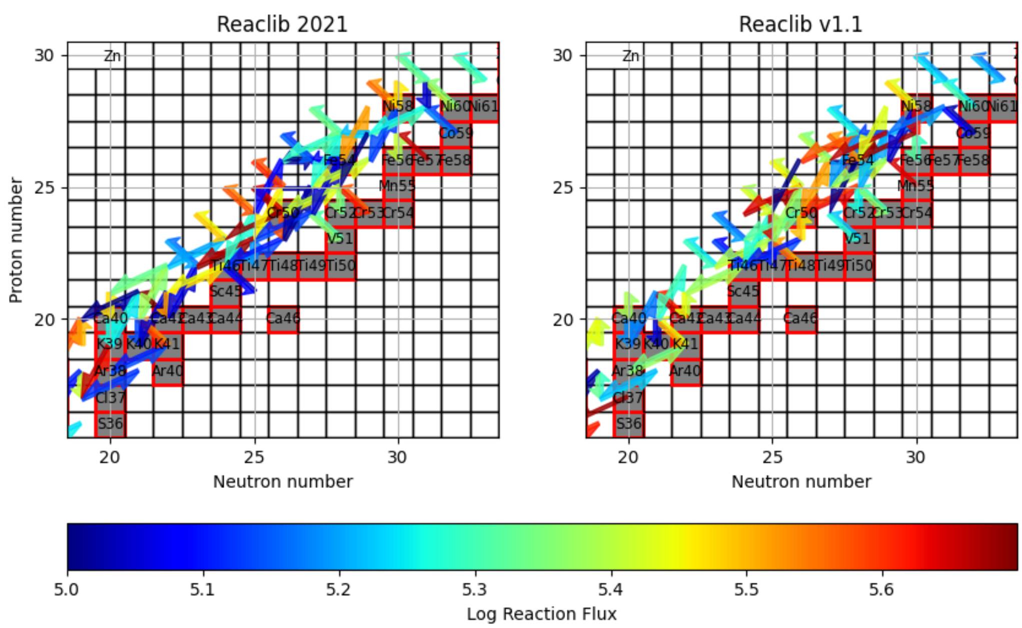

Figure 3.19: Reaction fluxes ($\frac{dY}{dt}$)at the peak temperature of 8.7 GK inside a common envelope accreting material at $128 \times 10^{-5} \mathrm{M}_{\odot} \mathrm{s}^{-1}$. Reaction fluxes produced using the Default Reaclib 2021 are shown on the left, reaction fluxes produced using Reaclib v1.1 are shown on the right.

3.3 Removing supplementary libraries

When NuGrid was first released in 2008 there was not a single Reaction rate library that contained all the rate information needed to simulate the full range of nucleosynthesis that was desired. This led to multiple reaction rate libraries being included to supplement the Reaclib v0.5 that NuGrid initially used. Now that Reaclib 2021 is installed three of the supplementary libraries are outdated and should be removed; the Iliadis 2001 proton capture study [[27]], the NACRE compilation of charged particle interactions [3] and the VITAL library. The NACRE and Iliadis 2001 publications have both been superseded by the NACRE II update [63] and by charged particle thermonuclear reaction rate study from [26]. The VITAL library is a custom-made reaction library built specially for NuGrid. It contains 117 reaction rates and is used as a supplementary library as well as a customisable list for users to add new reactions to the network. Consequently, some of the rates that are used in the VITAL library do not have alternative libraries to read from and so certain VITAL rates must remain in the network.

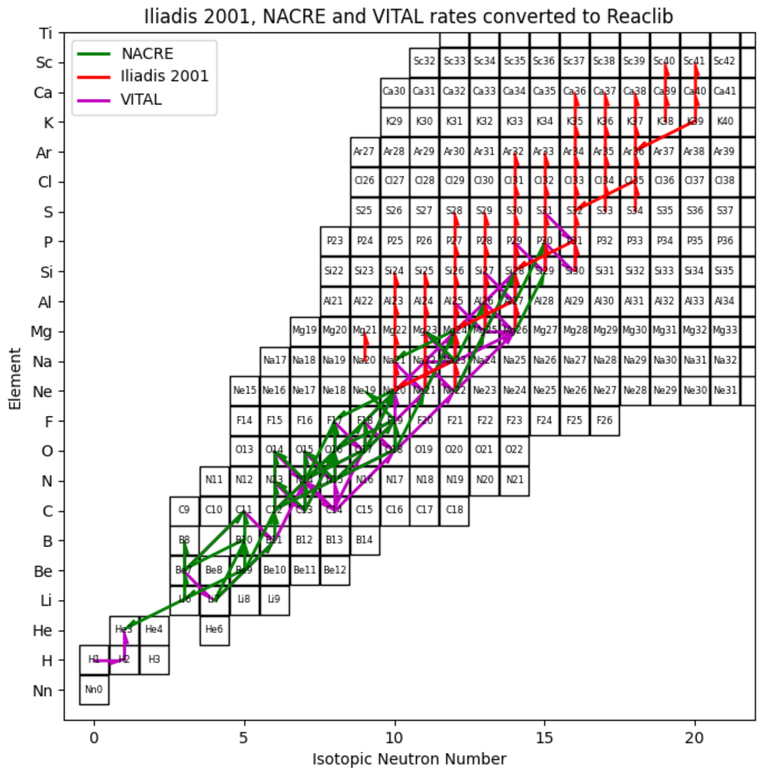

Figure 3.20: A chart of isotopes showing which reactions use nuclear reaction rate data from Iliadis 2001, NACRE and VITAL which will be converted to use nuclear reaction rate data from Reaclib 2021.

Figure 3.20 shows the reactions that can use reaction rate data from JINA Reaclib 2021 but are set to use the Iliadis 2001, NACRE and VITAL libraries in NuGrid. These are mainly charged particle reactions, such as proton or α-particle captures, or decay reactions like β^+ or α decays. From figure 3.15 it is clear that the reaction channels used in the low accretion rate common envelope test environment are using reaction data from these now defunct libraries. To guarantee a fair comparison between different post processing codes in the next chapter the networks must use the same reaction libraries and so each reaction using data from one of the aforementioned supplementary libraries was converted to use data from JINA Reaclib 2021. This section will assess the impact that this conversion has on the resulting isotopic and elemental abundance data.

3.3.1 Simple Hydrostatic burn

The elemental mass fraction distribution shown in figure 3.21 shows that for this constant temperature and density trajectory there is very little impact from removing the supplementary libraries. Only Beryllium, Oxygen and Fluorine have significant differences in the resulting mass fractions. The Fluorine mass fraction varies when converting the NACRE library only, whereas the Beryllium mass fraction is impacted by converting each reaction library to Reaclib, however when all the supplementary libraries are converted to Reaclib 2021 the final Beryllium abundance is the same as the standard library compilation.

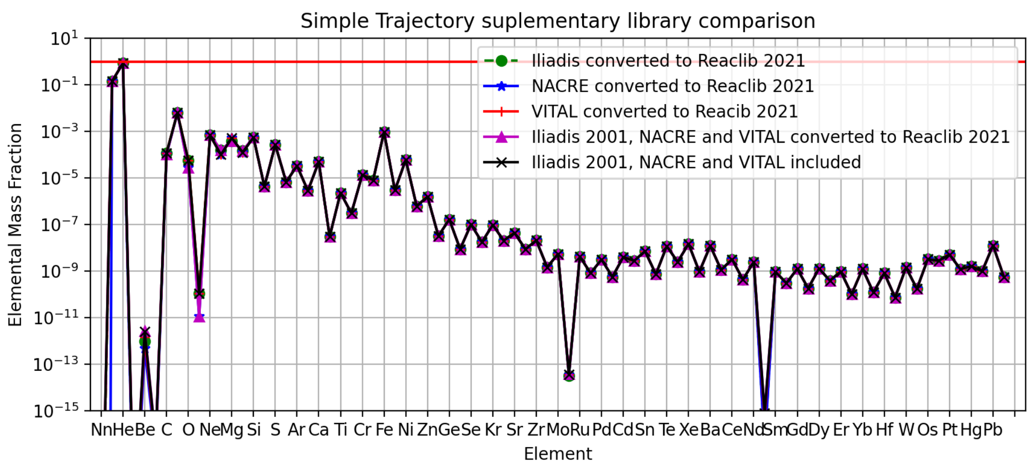

Figure 3.21: Final elemental mass fractions for a simple hydro static burn in NuGrid. Green circles show the results when using Reaclib 2021 in place of Iliadis 2001. Blue Stars show the results when using Reaclib 2021 in place of NACRE rates. Red crosses show the final mass fraction when using Reaclib 2021 in place of VITAL rates (where possible). Magenta triangles show the results when using Reaclib 2021 in place of Iliadis 2001, NACRE and VITAL, and black X's show the results when using Iliadis 2001, NACRE and VITAL alongside Reaclib 2021.

Further investigation into the isotopic mass fractions are shown in figure 3.22. From this it is clear that the Fluorine abundance is lower when using the updated rate information from Reaclib 2021. This results in a lower final mass fraction for $^{17,18\&19}$F and $^{16\&17}$O. The difference in these isotopic abundances comes from using JINA Reaclib 2021 reaction data for

$^{16}O(p,\gamma)^{17}F$, taken from [25], and $^{17}O(p,\gamma)^{18}F$ taken from [26]. These reactions are normally taken from the NACRE database when using NuGrid. As the material leaves the CNO cycle it follows a series of proton capture reactions on oxygen isotopes and then β decays back to stability. The isotopic mass fraction of beryllium varies when removing each reaction library. The isotope with the largest mass fraction is ^{7}Be and so the variation seen in the elemental mass fraction is due to the variation seen in ^{7}Be shown in figure 3.22. The reaction rate data used to model production and destruction of this isotope is only taken from the VITAL and JINA Reaclib libraries, so the variation seen when removing NACRE and Iliadis 2001 is not expected. However, the main production method for ^{7}Be is from:

$$^{3}_{2}He + \alpha \longrightarrow ^{7}_{4} Be \tag{3.3}$$

which means ^{7}Be is directly related to the availability of ^{3}He and ^{4}He. Each library contains reaction rate data that does impact the helium abundances and from figure 3.22 it is evident that the ^{3}He and ^{4}He mass fractions follow the same pattern of change as ^{7}Be. It is also evident that when all the supplementary libraries are converted to Reaclib 2021 that the final isotopic abundances of helium and beryllium are the same as when they are included.

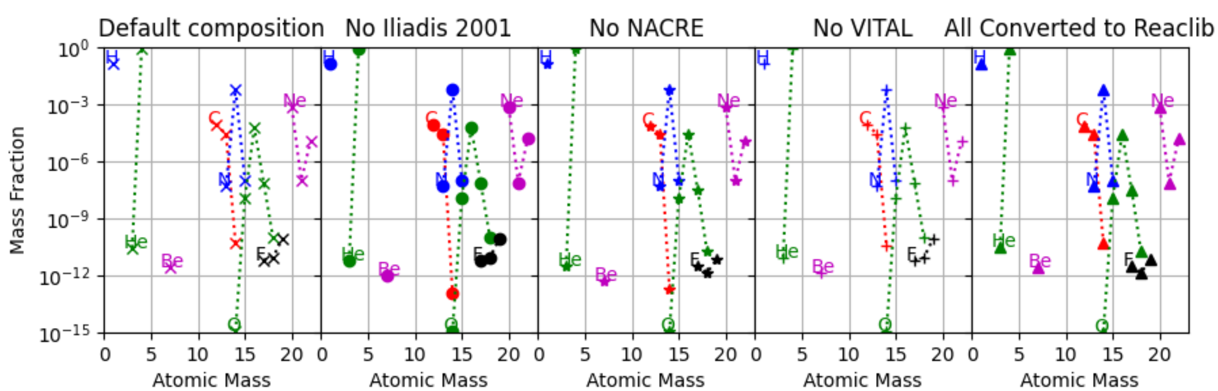

Figure 3.22: Isotopic abundance mass fractions for a simple hydrostatic burn using different Library compilations. Isotopes of different elements are shown using different colours and connected via dotted lines.

3.3.2 X-ray burst

The final elemental mass fraction for an X-ray burst trajectory with each supplementary library removed is shown in figure 3.23. The effect of converting supplementary libraries to JINA Reaclib 2021 is only seen in elements heavier than magnesium and lighter than manganese. Figure 3.20 shows that there are a large number of Iliadis 2001 reaction rates used in the same region where there are differences in elemental mass fraction. The differences seen in figure 3.23 are only seen in tests where the Iliadis 2001 reaction rates information is removed.

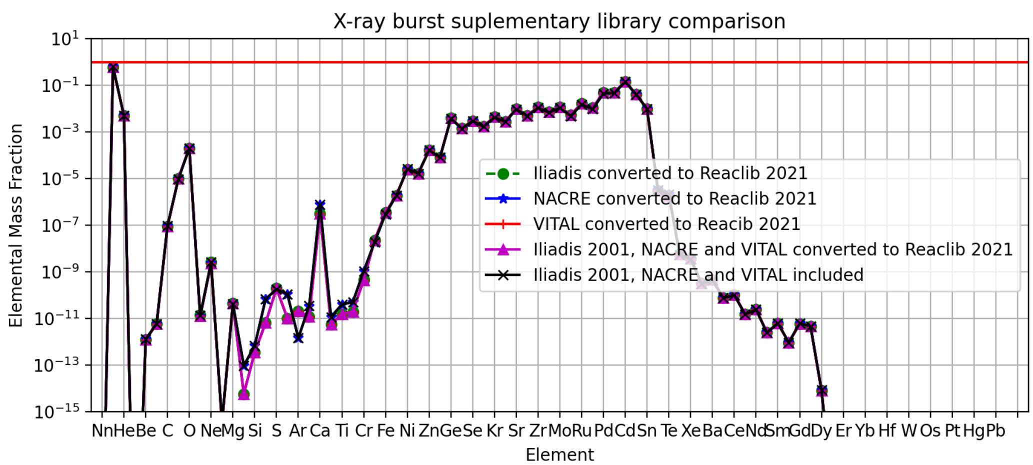

Figure 3.23: Final elemental mass fractions for the standard library composition (Black X's), Iliadis 2001 rates converted to Reaclib 2021 (Green circles), NACRE converted to Reaclib 2021 (Blue stars), Vital rates converted to Reaclib 2021 where possible (Black crosses) and all three converted to Reaclib 2021 where possible (Magenta triangles)

The final isotopic mass fractions for isotopes between magnesium and manganese are shown in figure 3.23. This clearly shows that only removing the VITAL or NACRE libraries does not cause any variation in isotopic mass fractions, figures 3.24.C and 3.24.D. but both instances where Iliadis 2001 is removed result in lower mass fractions for isotopes of aluminium, phosphorus, chlorine and potassium along with higher mass fractions for more proton rich isotopes' argon, potassium and calcium.

Further investigation into the isotopic abundances for isotopes between Magnesium and Manganese is shown in figure 3.24. Comparing the default library composition, figure 3.24.A, to the new composition with Iliadis 2001, NACRE and VITAL removed there are many differences in the isotopic mass fractions. Both isotopes of Aluminium result in lower mass fractions when using the pure Reaclib 2021 compilation, seen in figure 3.24.E, this can also be seen in figure 3.24.B when all Iliadis 2001 rate information is removed. The reduced Aluminium mass fractions come from updated proton capture rates on ^{24}Al and ^{25}Al in Reaclib 2021, which are taken from [37] and [48] respectively. The next isotopes that differ are ^{28}P to ^{30}P, ^{31}Cl to ^{35}Cl and ^{36}K and ^{37}K. Once again the difference is only seen when removing Iliadis 2001 rate information and comes from Reaclib containing proton capture information from [26], which was released 10 years after the Iliadis 2001 publication. Overall for the X-ray burst trajectory the differences in mass fraction for these isotopes come mainly from removing the Iliadis 2001 rate information, which is a necessary process to ensure the software is correctly modelling the nuclear physics.

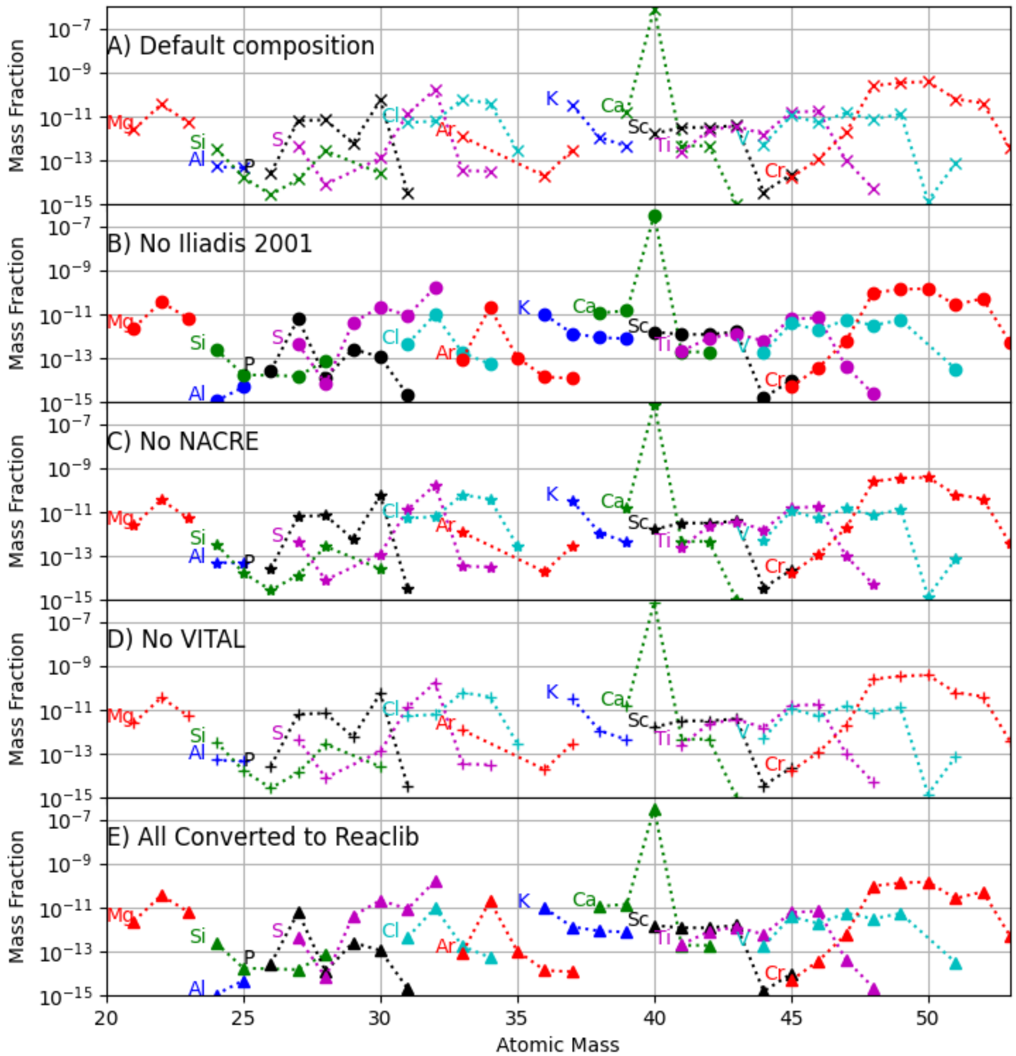

Figure 3.24: Resulting isotopic mass fractions between Magnesium and Manganese for an X-ray burst trajectory using; A) The standard supplementary library compilation in NuGrid with Reaclib 2021, B) All Iliadis 2001 reaction library rates converted to Reaclib 2021, C) All possible NACRE rates converted to Reaclib 2021, D) All possible VITAL rates converted to Reaclib 2021, and E) all possible VITAL, NACRE and Iliadis 2001 rates converted to Reaclib 2021.

3.3.3 Weak-s process

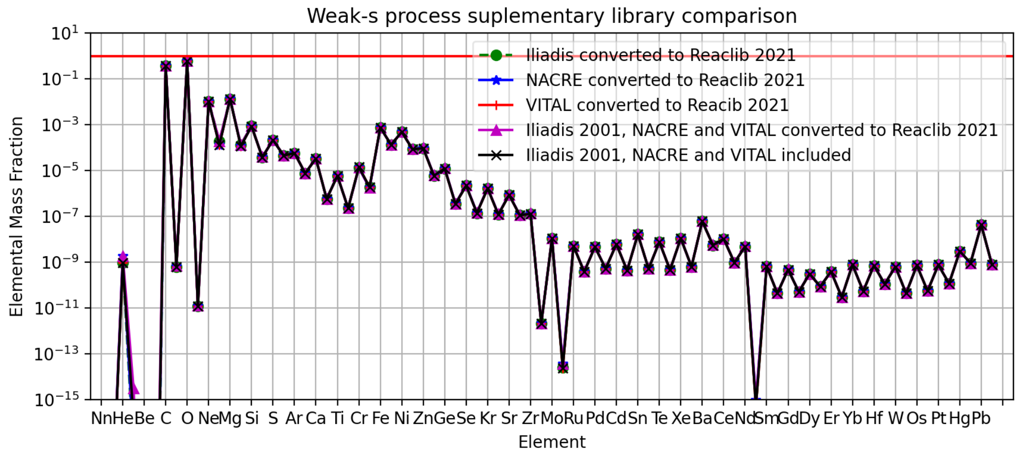

Figure 3.25: Elemental mass fractions for a weak-s process trajectory using different library configurations. Results from the Iliadis 2001 rate information converted to Reaclib 2021 are shown in green, all possible NACRE rate information converted to Reaclib 2021 are shown in blue, all possible VITAL rate information converted to Reaclib 2021 are shown in red, all possible Iliadis 2001, NACRE and VITAL rate information converted are shown in magenta and the standard library configuration using Reaclib 2021 is shown in black.

The weak-s process trajectory flux, shown in figure 3.12, does not use many of the reaction channels that are shown in figure 3.20. Therefore, removing the Iliadis 2001, NACRE and VITAL rate information will not have a large impact on the final elemental abundances. This can be seen in figure 3.25 as each elemental abundance is the same regardless of the library configuration. There is one exception to this, the Lithium mass fraction produced when using the pure Reaclib 2021 library compilation (all supplementary libraries converted to Reaclib 2021) is large enough to pass the 1×10^{-15} mass fraction threshold. This comes from a new ^{7}Be β^+ decay rate from [37] which replaces the 1988 VITAL rate which is taken from [9]. The Helium mass fraction is also higher when NACRE rate information is removed. This is due to the $^6\text{Li}(p, \alpha)^3\text{He}$ rate information is now taken from [50]. This shows that, depending on the environment, different reaction libraries within NuGrid can impact different regions of the nuclear chart.

3.3.4 Common envelope

Like in section 3.2.5 the common envelope environment has been evaluated over two different accretion rates, these are the same trajectories used in the previous Reaclib version comparison. The first has an accretion rate of $8 \times 10^{-5}\mathrm{M}_{\odot}\mathrm{s}^{-1}$ and a peak temperature of 2.2 GK, the second has an accretion rate of $128 \times 10^{-5}\mathrm{M}_{\odot}\mathrm{s}^{-1}$ and a peak temperature of 8.7 GK.

Common envelope with $8 \times 10^{-5}\mathrm{M}_{\odot}\mathrm{s}^{-1}$ accretion rate

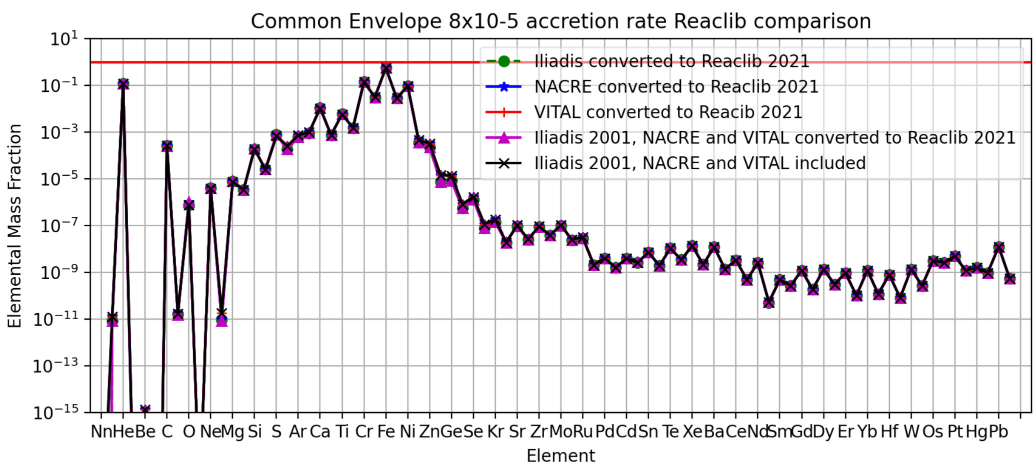

Figure 3.26: Elemental mass fractions for different library configurations simulating a common envelope trajectory with an accretion rate of $8 \times 10^{-5}\mathrm{M}_{\odot}\mathrm{s}^{-1}$. Iliadis 2001 rates converted to Reaclib 2021 are shown in green, all possible NACRE rates converted to Reaclib 2021 are shown in blue, all possible VITAL rates converted to Reaclib 2021 are shown in magenta and the standard library configuration using Reaclib 2021 is shown in black.

From figure 3.26 it is clear that converting rate information from the Iliadis 2001, NACRE and VITAL libraries separately to Reaclib 2021 does not have a large impact on the final elemental mass fractions. However, when all three supplementary libraries are removed the combined effect reduces the mass fraction of Sodium, Zinc, Gallium, Germanium and Arsenic. The largest difference is in the Gallium elemental mass fraction. When using the standard supplementary library set up the mass fraction is 1.431×10^{-5}, converting the NACRE and VITAL rates to Reaclib 2021 also produces the same mass fraction (within 1% of the same value), however when the Iliadis rate information is removed this drops to 7.638×10^{-6}. This is still within a factor of two and as the Iliadis 2001 rates are outdated this must be the more accurate value.

Common envelope with $128 \times 10^{-5} M_{\odot} s^{-1}$ accretion rate

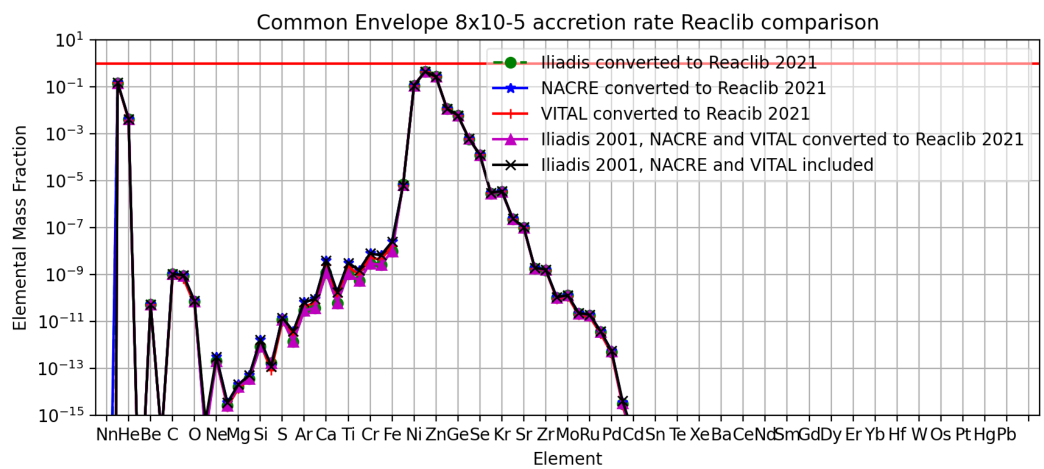

Figure 3.27: Elemental mass fractions for different library configurations simulating a common envelope trajectory with an accretion rate of $128 \times 10^{-5} M_{\odot} s^{-1}$. Iliadis 2001 rates converted to Reaclib 2021 are shown in green, all possible NACRE rates converted to Reaclib 2021 are shown in blue, all possible VITAL rates converted to Reaclib 2021 are shown in magenta and the standard library configuration using Reaclib 2021 is shown in black.

The resulting mass fractions from different supplementary libraries are shown in figure 3.27. Changing the source of reaction rate information has a large impact on elements between Silicon and Cobalt. These elements are destroyed during NSE via rp-process nucleosynthesis, and from figure 3.27 it is evident that removing the outdated Iliadis 2001 rate information has a large impact for this region. Further investigation into the isotopic abundances, as shown in figure 3.28, confirms that removing Iliadis 2001 results in lower mass fractions for all isotopes in this region. Removing all possible VITAL rates has a similar effect but to a much lesser extent. As the VITAL supplementary library was designed for users to add complex and regularly updated reaction rate information that was not included in the original Reaclib v0.5 that NuGrid was designed around. Reaclib 2021 now contains most of the same rates that VITAL was designed for and as VITAL has not been updated since the release of Reaclib 2021 it contains some outdated information now.

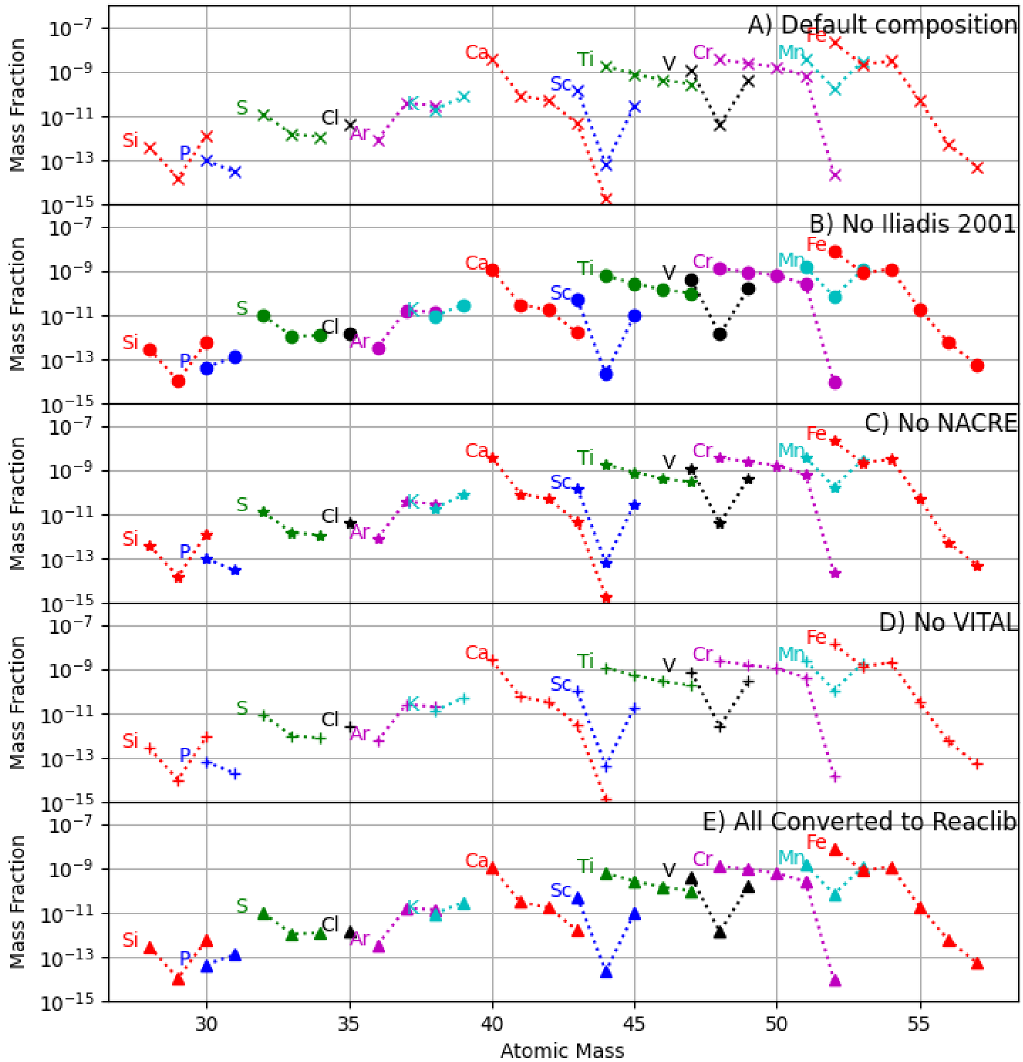

Figure 3.28: Isotopic mass fractions for isotopes between Silicon and Iron for a common envelope with a $128 \times 10^{-5} \mathrm{M}_{\odot} \mathrm{s}^{-1}$ accretion rate using; A) the standard reaction library compilation used in NuGrid, B) all Iliadis 2001 reaction rate information replaced with Reaclib 2021, C) all possible NACRE reaction rate information replaced with Reaclib 2021, C) all possible VITAL reaction rate information replaced with Reaclib 2021 and E) all possible Iliadis 2001, NACRE and VITAL rate information replaced with Reaclib 2021.

3.3.5 Final Library composition

From the results produced in this chapter all further PPN runs have been run using Reaclib 2021 and the supplementary libraries from Iliadis 2001, NACRE and VITAL have been removed, and reaction rate information is taken from Reaclib 2021. This is because the version of Reaclib that NuGrid comes with, Reaclib v1.1, was published 8 years before Reaclib 2021 and contains outdated reaction rate information. There is little impact for the example trajectories that produce isotopes along the valley of stability or in the proton rich region of the nuclear chart.

Of the supplementary libraries, almost all the reaction rate information from these was removed. This is because the Iliadis 2001 rates are two decades old and have become outdated. Most of the NACRE rate information was removed as this was included in NuGrid before the NACRE II [63] reevaluation of rate information was released, and this release is included in Reaclib 2021. Approximately 60% of the VITAL rates were removed, which is the most that can be removed from NuGrid. This is because the VITAL library contains over 40 reaction rates for complex reactions (such as the triple α reaction) that are not included in the Reaclib 2021 library. In total all 51 reactions from Iliadis 2001, 45 out of 51 reactions from NACRE and 74 out of 117 VITAL reactions were converted to use Reaclib 2021.

Chapter 4

Comparing different Post Processing Codes

This chapter will investigate how different PPN codes model a variety of environments. A detailed description on how each code models the changes in isotopic mass fractions is given. Each code is compared to NuGrid, as this software provides the most information regarding reaction processes used during the simulations.

4.1 Nuclear network code details

Four different nuclear network codes were used in this comparison study, to investigate the effects of the different numerical solvers and screening implementations can have on final abundances for the four different scenarios used previously. The reaction rate libraries in each code have been adapted or converted to use the default Reaclib 2021 library to make sure that any differences in the results do not come from different input physics, and each scenario investigated has the same initial abundance (the simple hydro static burn, the common envelope, X-ray burst and weak s-process trajectory). This chapter will provide a review of how each code models isotopic abundance changes, what changes have been made to the reaction libraries and how each code simulates the coulomb screening. This effect is required when looking at charged particle interactions inside plasma as the reacting nuclei are the same charge and repel each other due to the coulomb interaction. SkyNet is the only code to use a different screening method not built from first principles, but based on statistical averages of the screening effect from different contributions. Further details as to how screening is calculated for each code are given in the next sections.

4.1.1 NuGrid

NuGrid uses a high order Bader-Deuflehard method, [5], to calculate the resulting abundance of each isotope. This method models the production and destruction of a single isotope, i, in the form of an equation dependent on the abundance of the isotope, Y_i.

$$\frac{dY_i}{dt} = \sum_j R_{ji} Y_j - \sum_k R_{ik} Y_i \tag{4.1}$$

Where R_{ji} is the reaction rate transforming isotope j into the product i and R_{ik} is the reaction rate destroying isotope i to produce isotope k. This is summed for all possible production and destruction methods to get the total change in isotope abundance, $\frac{dY_i}{dt}$. For a given abundance, $Y(t)$, at time, t, the abundance at the next time-step, $t + \Delta t$, can be predicted using the following equation:

$$Y_i^{(0)}(t + \Delta t) = Y_i^0 + \Delta t \cdot \frac{dY_i}{dt} \tag{4.2}$$

Equation 4.2 is then used to estimate the abundance at time t + Δ t, but as this is an explicit equation it is only dependent on the state of the system at time t. As there is still nucleosynthesis happening at time t +Δt the abundance change at time t +Δt will also impact the isotopic abundance at this time step. From equation 4.2 and using equation 4.1 for time t + Δt the following equation can be used to model $Y_i(t + \Delta t)$.

$$Y_i(t + \Delta t) = Y_i(t) + 2\Delta t \left(\left(\frac{dY_i}{dt} \right)_t + \left(\frac{dY_i}{dt} \right)_{t+\Delta t} \right) \tag{4.3}$$

The roots of equation 4.3 can then be found using the iterative Newton-Raphson process to find $Y_i(t + \Delta t)$. This is repeated until the solution has converged to within a specified mass fraction threshold, which is set to 1×10^{-15} in NuGrid. If the difference in time, Δt, is too large the solution will not converge within the specified number of iterations. If this occurs Δt is broken up into sub time-steps and the process is repeated. Therefore, low temperatures with little activity and very large time-steps can be processed.

For each time-step that is calculated the uncertainty in the calculated isotopic mass fraction is the same as the convergence criteria, $1{\times}10^{-15}$. If the mass fraction at each time-step was independent of the previous mass fraction the final uncertainty would simply be:

$$\sqrt{u_0^2 + u_1^2 + \cdots + u_x^2} \tag{4.4}$$

Where u is the uncertainty at each time-step and x is the total number of time-steps, resulting in $\sqrt{x} \times 10^{-15}$. However, as isotopic mass fraction is directly linked to the mass fraction of isotopes at the previous time-step this uncertainty is carried forward throughout the simulation, potentially compounding the effect. Therefore, the final uncertainty in isotopic mass fraction is the sum of isotopic uncertainty across the length of the trajectory, $x \times 10^{-15}$. Due to the number of time-steps in the different trajectories this results in uncertainties between $1.3 - 2.6 \times 10^{-12}$ for isotopic mass fractions and on the order of $\times 10^{-11}$ for elemental mass fractions. This error does not take into account the statistical uncertainties inside the code, such as the uncertainty in reaction rates and temperature grid resolution.

NuGrid calculates the screening effect via the Path Integral Monte Carlo (PIMC) method, outlined in [41] and verified by [11]. Unlike the classical mechanical approaches where the particle is described by a single trajectory, the PIMC method describes the particle using a series of paths that have a specific probability for the particle to take. When looking at two interacting particles the interaction energy is calculated for every possible path that they might take and a statistical average is calculated. The PIMC method also simulates surrounding ions, the collective response of these ions provide more information about the reaction that is being simulated. It is also important to include these ions when looking at screening as the motion of surrounding particles will cause fluctuations in the screening potential.

4.1.2 PRISM

Designed at Los Alamos National Laboratory for investigation into rare earth materials produced through the r-process [43], PRISM was designed to probe the limits of neutron rich nucleosynthesis. It has also been designed for testing new nuclear physics in these scenarios [42], with an adaptable nuclear physics input. For this work the network size been modified to match the network in NuGrid. The standard network size in PRISM contains 13262 isotopes ranging between Hydrogen and $Z = 133$ with the distribution of isotopes predominantly on the neutron rich side of stability. The new network has been reduced to 5234 isotopes ranging from Hydrogen to Bismuth with an equal distribution of isotopes on the proton and neutron rich side, to match the network size and shape used in NuGrid. PRISM comes with a copy of the JINA Reaclib v2.1 which has been updated to the default Reaclib for a fair comparison. Atomic mass data information is taken from [62] and nuclear decay properties are taken from [32].

The relative abundance in PRISM is calculated as a function of isotope mass, proton number and time, and it is normalised via the following convention:

$$\sum_{\forall(Z,A)} Y(Z,A,t) \times A = 1 \tag{4.5}$$

The evolution of $Y(Z,A,t)$ can be modelled via a series of equations that correspond to the nuclear processes that occur at specific time during the evolution. For each possible reactant and product this results in two associated differential equations:

$$\left\{ \forall_i \in \{R_1, ..., R_N\} \, \frac{dY(Z_i, A_i, t)}{dt} - = \lambda(t)\rho^{N-1} \prod_{j=R_1,...,R_N} Y(Z_i, A_i, t) \right\} \tag{4.6}$$

and

$$\left\{ \forall_i \in \{P_1, ..., P_M\} \, \frac{dY(Z_i, A_i, t)}{dt} + = P(i)\lambda(t)\rho^{N-1} \prod_{j=R_1,...,R_N} Y(Z_i, A_i, t) \right\} \tag{4.7}$$

Where R_i is the reactant, N is the number of reactants, $\lambda(t)$ is the reaction rate as a function of temperature and time, ρ is a density at time t and $P(i)$ is the average number of times that the nuclear species (Z_i, A_i) is produced every time the process occurs. Using the information from the reaction libraries each of the quantities related to each process are known and a series of differential equations can be found that fully determine the evolution of $Y(Z, A, t)$ as long as the initial conditions, $Y(Z, A, t = 0)$, are known.

PRISM uses a different numerical solver to calculate the evolution of $Y(Z, A, t)$. The Newton-Raphson method is used to find the roots to a first order implicit backward Euler equation, producing a square matrix of dimension N, where N is the number of isotopes in the network. Then, using the PARIDISO matrix solver it calculates the change in abundance between each time-step [35].

Screening in PRISM has not been as extensively tested due to the environment it has been designed for. As r-process reactions consist of mainly neutron capture, screening is not a priority as there are no coulomb barriers to overcome with neutral particles. The screening method comes from [11], but it has only been implemented for two body reactions, so higher multiplicity reactions (such as the triple alpha reaction) do not undergo screening treatment.

4.1.3 SkyNet

SkyNet uses the same network solving method as PRISM, using the Newton-Raphson method to find the roots of first order backward Euler equations for a matrix of isotopes. Full details of the method used can be found in [36] but simply put, this method creates a series of equations to calculate the composition at a specific time. Vector $\mathbf{Y}(t) = Y_i(t)$ where $Y_i(t)$ is the relative abundance of nuclear species i at time t. After some time-step Δt the change in composition vector can be written as:

$$\dot{\mathbf{Y}}(t + \Delta t) = \frac{\mathbf{Y}(t + \Delta t) - \mathbf{Y}(t)}{\Delta t} \tag{4.8}$$

which can then in turn be interpreted as:

$$\mathbf{0} = \dot{\mathbf{Y}}(\mathbf{x}, T(t+\Delta t), \rho(t+\Delta t)) - \frac{\mathbf{x} - \mathbf{Y}(t)}{\Delta t} = \mathbf{F}(\mathbf{x}, T(t+\Delta t), \rho(t+\Delta t) \tag{4.9}$$

Where $\mathbf{x} = \mathbf{Y}(t + \Delta t)$ is the unknown composition after $t + \Delta t$ time. Using the trajectory information, $T(t)$ and $\rho(t)$ are known and so the function $0 = \mathbf{F}(\mathbf{x}, T, \rho)$ becomes a root finding problem. Here SkyNet implements the Newton-Raphson method to find the root to $\mathbf{F}(\mathbf{x}, T, \rho)$ at every time-step. SkyNet evolves the isotopic abundance over the course of the simulation, however it does not store individual isotopic abundances, instead the final output provides abundance and mass fraction information for an atomic mass range and final abundances for each atomic charge and mass. To convert between isotopic abundance and isotopic mass fraction the following expression is used:

$$X_i = \frac{Y_i \cdot m_i}{\Sigma_j Y_j \cdot m_j} \tag{4.10}$$

Where Y_i is the abundance of isotope i, m_i is the atomic mass of the isotope, X_i is the calculated mass fraction and j is the total number of isotopes in the network.

The screening method used in SkyNet is outlined in [36]. This screening effect is not derived from first principles. The screening effect is calculated separately for weak, intermediate and strong screening and then a dimensionless correction parameter is applied to ensure the correct screening method is used at the correct temperature or charge regime, as shown in Figs 4.1. Weak screening occurs when the coulomb interaction energy is much lower than the surrounding thermal energy, for this the electrostatic Poisson-Boltzmann distribution is solved to find the chemical potential correction factor. Intermediate and strong screening occurs when there is sufficient density or when looking at highly charged particle interactions.

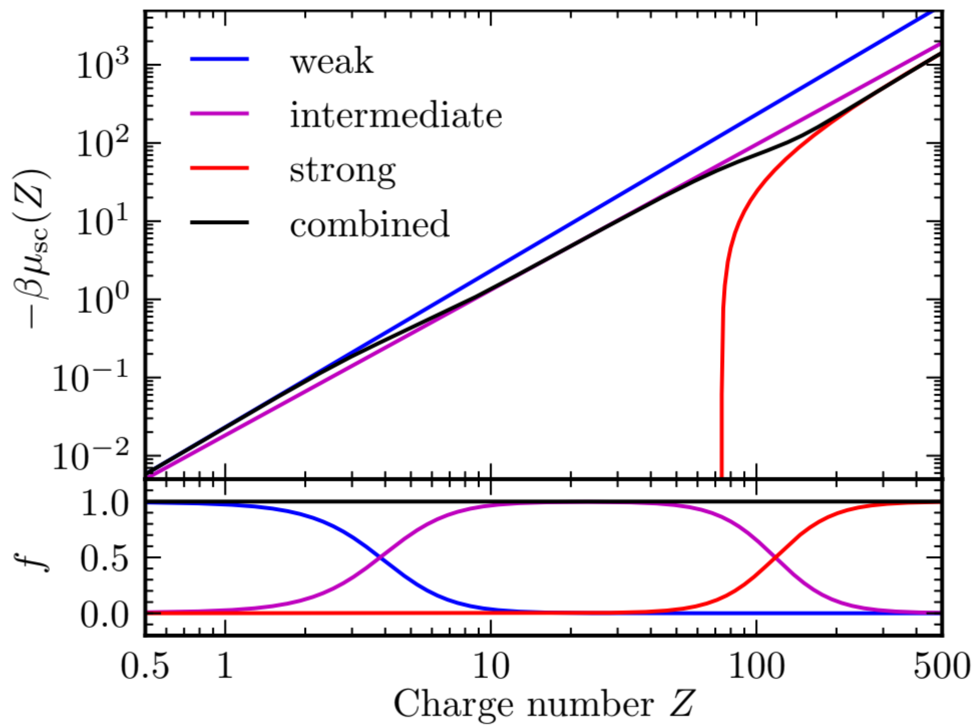

Figure 4.1: Charged particle screening [36]

SkyNet contains tabulated β-decay rates as a function of both temperature and electron fraction for both β^+ and β^- decays based on [21] and [33].

4.1.4 Nucleo

Nucleo [38] is the final code used in this comparison. This software is based on code originally developed by Nicos Prantzos in the 1990s, since then it has been updated extensively by Christian Illiadis and others at North Carolina State University to provide functionality for reaction rate studies. In 2009 it was upgraded to include tabular reaction rate inputs which allow for sensitivity studies as shown in [17] and [38].

The ODE solver was originally based on the Wagoner 2-step semi-implicit algorithm from [61]. From work done in [39] it has since been upgraded to use Gear's backward differential formulas from [23] and is coupled with the sparse matrix solver `MA48` which is an updated version of the packages specified by [59]. This upgrade has increased the speed and accuracy of the ODE solver. The new method uses the abundance from the previous time-step and extrapolates a nucleosynthesis time-step. This is then followed by a Newton-Raphson correction for an approximate implicit differential method. As a result of the more accurate predictive nucleosynthesis step, large time-steps can be processed with smaller correction factors. Due to the prediction-correction this method allows for the computation of numerical errors, like the Bader-Deuflhard method. Nucleo is designed to read the StarLib reaction rate tables, however for these tests it instead used the default Reaclib reaction rate library that has been converted to a tabulated form. This code is not designed as an all-purpose nucleosynthesis code, has not been designed to handle r-process nucleosynthesis and is not an adaptive network. As a result of this each scenario has a separate network constructed. Each network only contains the isotopes needed for nucleosynthesis flow in that specific environment and the r-process trajectory has not been simulated inside Nucleo. As a result of this a direct comparison between Nucleo and the other codes cannot be made as the largest network that can be used only has 1,500 isotopes, less than a third of the size of the networks used in NuGrid, PRISM and SkyNet.

4.2 PPN code comparison results

To understand the impact that different Post Processing Networks can have on a selected environment, a detailed analysis of the elemental and isotopic abundances for each scenario was undertaken. NuGrid, PRISM and Nucleo provide isotopic abundance outputs, whereas SkyNet provides abundances as a function of proton number or mass number. Nucleo uses specific networks that are much smaller than the other three codes, therefore it may limit the production of isotopes if the nucleosynthesis reaches the network boundary. For each environment the elemental mass fraction from PRISM, SkyNet and Nucleo were compared to the NuGrid results.

4.2.1 Simple Hydrostatic burn

The elemental mass fraction for a simple hydro-static burn run is shown in fig 4.2. For this low temperature and density environment the main nucleosynthetic process that occurs is p-p chain reactions, leading to high Helium mass fractions, which is seen across all the codes. The largest difference in mass fraction is seen at Beryllium. Nucleo produces a much higher mass fraction when compared to NuGrid and SkyNet, whereas PRISM destroys all the available Beryllium resulting in a mass fraction below the threshold limit of 1×10^{-15}. There are also significant differences in the unstable elements Technetium and Promethium. Due to the low temperature there is very little nucleosynthesis occurring in this region and so the difference in these elements is likely a result of different references used the for the decay libraries of unstable nuclei. Overall the networks produce a similar pattern of elemental mass fractions.

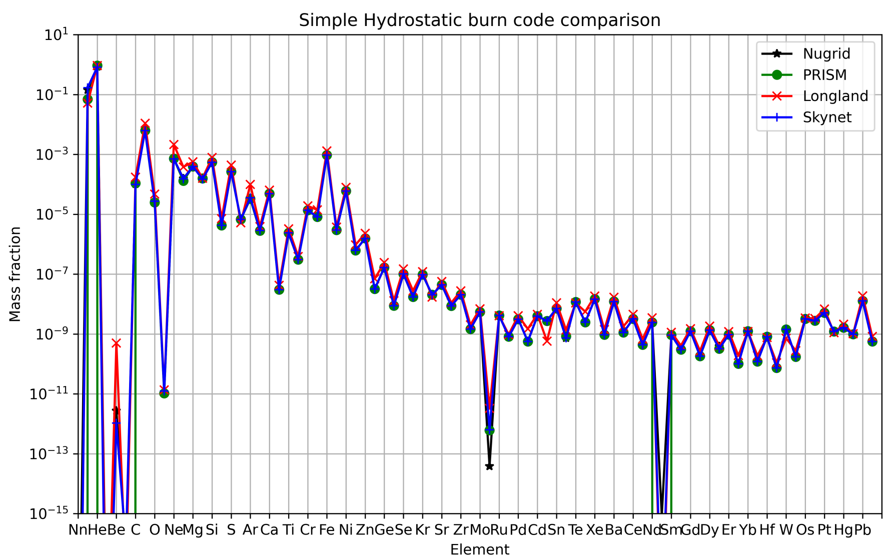

Figure 4.2: Final Elemental mass fractions for a simple hydro-static burn using NuGrid (Black), PRISM (Green), Nucleo (Red) and SkyNet (Blue).

To understand the difference in the elemental mass fractions the ratio of difference is shown in fig 4.3. For this the elemental mass fraction produced in PRISM, SkyNet and Nucleo are divided by the elemental mass fraction in NuGrid to produce a ratio of mass fractions. The left side of figure 4.3 shows elements below Carbon, where the most nucleosynthesis occurs for this trajectory. SkyNet, PRISM and Nucleo produce a Helium mass fraction to within 10% of the mass fraction produced by NuGrid. Both PRISM and Nucleo produce helium mass fractions of 0.921 and 0.930 respectively, whereas NuGrid and SkyNet result in 0.848 and 0.821. The larger mass fractions in PRISM and Nucleo are due to the different screening methods that they use. Both PRISM and Nucleo use a simpler screening method compared to NuGrid and SkyNet. The helium mass fraction is the largest mass fraction of all elements in the system as expected for p-p chain scenarios. The Hydrogen mass fractions are all within an order of magnitude, however PRISM and Nucleo both end with less than half the amount of Hydrogen compared to NuGrid and SkyNet, as in both PRISM and Nucleo more hydrogen is fused to produce the larger helium mass fractions. The neutron mass fraction from Nucleo, SkyNet and PRISM are all under-produced when compared to NuGrid, however the final neutron mass fraction is below the threshold in all four of the codes and so this difference can be disregarded. The Beryllium mass fraction has the largest disparity across all four of the codes. With Nucleo producing over 100 times the amount seen in NuGrid, SkyNet producing half the amount and PRISM completely destroying it all. This is due to the different decay information that the codes use, as the beryllium that is produced is unstable ^{7}Be and ^{8}Be, as well as the different screening methods.

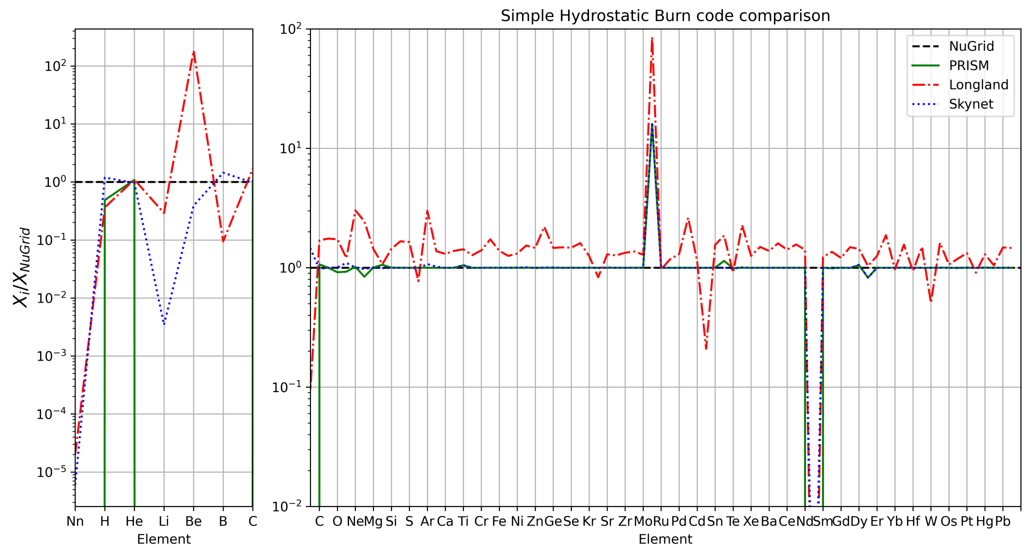

Figure 4.3: Ratios of elemental mass fractions for PRISM (Green), SkyNet (Blue), and Nucleo (Red) compared to NuGrid (Black dashed horizontal line) are shown. This represents the over or under production of each element when compared to the NuGrid mass fraction. Elements below Carbon are shown in the left figure, and elements above Carbon are shown on the right.

Looking at elements above Carbon, figure 4.3 shows that the results from PRISM and SkyNet match extremely well with the NuGrid elemental mass fractions. All other discrepancies between PRISM and NuGrid within this region have a mass fraction within 20% of the NuGrid value. However, Nucleo produces higher mass fractions for all elements other than Lithium, Boron, Chlorine, Rubidium, Indium and Tungsten. The exact cause for the differences seen in Nucleo are still not understood and require further investigation. Both Technetium and Promethium have significantly different mass fractions in figure 4.2, as these elements do not have any stable isotopes the difference in mass fractions is likely due to the different references used for decay data for unstable nuclei. Overall, NuGrid, PRISM and SkyNet all produce very similar mass fraction distributions for elements above carbon, however Nucleo shows differences for each element and does not agree with the other codes for this simple trajectory.

4.2.2 X-ray Burst

The final elemental mass fractions for an X-ray burst are shown in figure 4.4. From this it is clear that each code models the X-ray burst environment very differently, but there are some trends that can be seen across different codes.

SkyNet is the only network to destroy all the available Hydrogen during the trajectory, whereas NuGrid and PRISM end the simulation with almost the same mass fraction and Nucleo results in approximately 20% of the original Hydrogen mass fraction.

SkyNet is also the only network to produce intermediate mass elements between Neon and Calcium. During the trajectory SkyNet fuses the hydrogen with seed nuclei from the initial composition to produce isotopes. This region is expected to see an increase in mass fraction when compared to the initial abundance of the system, however as NuGrid, PRISM and Nucleo all result in a much lower mass fraction for this region it highlights the impact of the different screening method used in SkyNet. As SkyNet uses a combined screening effect which changes as a result of isotope charge, figure 4.1, and temperature, whereas the other codes use screening methods that vary only as a function of temperature. This means that for elements greater than neon the screening effect in SkyNet is weaker than the screening effect in the other three codes.

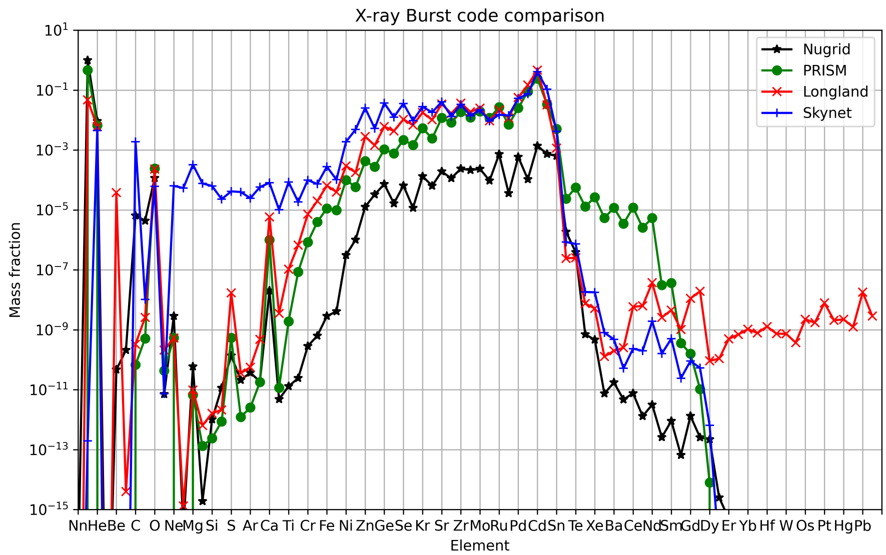

Figure 4.4: Final elemental mass fractions for an X-ray burst trajectory. NuGrid is shown using black stars, PRISM is shown using green circles, Nucleo is shown using red X's and SkyNet is shown using blue crosses.

NuGrid, PRISM and Nucleo all produce a peak at Calcium, this is due to the ^{40}Ca isotope. It is doubly magic, meaning the proton and neutron shells are closed, and adding another nucleon to the nucleus requires more energy as it will be unpaired and in a much higher energy level. As the trajectory evolves material is trapped in the stable ^{40}Ca until the temperature is high enough to produce ^{41}Sc, but other isotopes in the same mass region still undergo nucleosynthesis.

The most abundant element in all networks (other than Hydrogen) is Cadmium. As this is a high temperature (1.91 GK), proton rich scenario rp-process nucleosynthesis is expected to occur, producing material up to the Tin Tellurium cycle. All four codes produce the same elemental mass fraction shape, however NuGrid is approximately two orders of magnitude smaller for all element between Zinc and Cadmium, as seen in figure 4.5. Further analysis reveals NuGrid shows a higher ratio of proton emission to β^+ decay from unstable isotopes near the proton drip line, therefore resulting in the high hydrogen mass fraction and lower mass fraction for elements up to Tin.

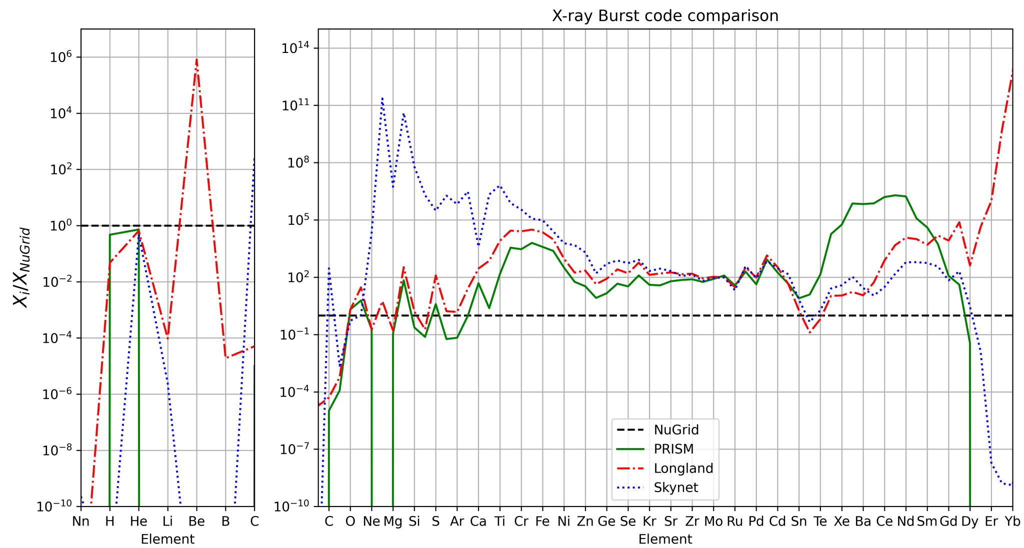

Figure 4.5: Ratios of elemental mass fractions for PRISM (Green), SkyNet (Blue), and Nucleo (Red) compared to NuGrid (Black dashed horizontal line) are shown. This represents the over or under production of each element when compared to the NuGrid mass fraction. Elements below Carbon are shown in the left figure, and elements above Carbon are shown on the right.

For elements beyond the Tin Tellurium cycle there is a sharp decline in mass fraction, as seen in NuGrid and SkyNet (with NuGrid once again showing mass fractions three to four orders of magnitude below SkyNet), PRISM however shows a significant mass fraction for elements up to Neodymium before sharply declining. While there will be some nucleosynthesis for elements in this region this is still higher than expected as there are no seed nuclei in the initial abundance and the Tin Tellurium cycle limits proton captures. Nucleo also shows evidence of continued nucleosynthesis beyond Tin, with elements up to Bismuth being produced. This is due to the smaller network in Nucleo. As this network does not reach as far into the proton rich side of the nuclear chart as the other codes. In Nucleo material reaches the network boundary and is instantly β^+ decayed, but in NuGrid, PRISM and SkyNet the material is able to continue capturing protons and produce nuclei that may decay via proton or α emission.

Overall the four codes produced similar patterns of elemental mass fraction, but with significant differences in different mass regions. Low mass fractions for intermediate elements are seen in NuGrid, Nucleo and PRISM. High mass fractions for elements between Nickel and tin are seen in all codes but NuGrid underproduces these isotopes by three orders of magnitude compared to the other codes. A sharp decrease in mass fraction for elements above tin is seen in NuGrid, Nucleo and SkyNet, with PRISM showing much higher mass fractions for elements between tin and Neodymium. Elemental mass fractions for elements heavier than dysprosium are below threshold in NuGrid, PRISM and SkyNet but are much higher in Nucleo. NuGrid is the only code to show evidence of all four trends.

4.2.3 Weak s-process

Like with the r-process scenario, the weak s-process scenario has only been run in NuGrid, PRISM and SkyNet. The three codes produce similar mass fraction distributions for elements heavier than carbon and lighter than barium, as shown by Figure 4.6. There are large differences in the low mass isotopes up to and including Boron. For most elements the mass fraction ratio is near 1, showing very similar mass fractions, however a few elements do not fit this trend, such as nitrogen with SkyNet only producing 14% of the mass fraction NuGrid produces. For elements between Nickel and Antimony both SkyNet and PRISM produce the same mass fractions, whereas NuGrid under-produces elements within this range, except Niobium.

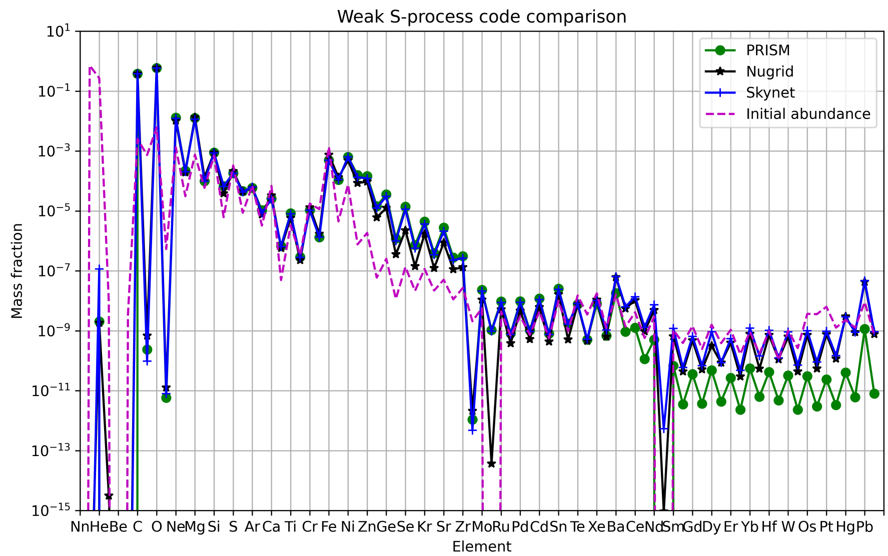

Figure 4.6: Final elemental mass fractions for a weak s-process trajectory. NuGrid is shown using black stars, PRISM is shown using green circles and SkyNet is shown using blue crosses.

For all elements above Barium PRISM produces elemental mass fractions over an order of magnitude lower than NuGrid and SkyNet. As this is a low temperature and low density trajectory and the material in this region consists of stable isotopes in the initial composition it is not expected for this to vary much from the initial mass fractions. The reduced elemental mass fractions come from neutron captures onto stable nuclei which then decay into lower mass nuclei via proton, or alpha emission. This results in excited states in the daughter nuclei which can then decay via the same emission, even if the daughter nuclei is stable in the ground state. As PRISM is designed for r-process nucleosynthesis it incorporates decays from excited state nuclei in detail.

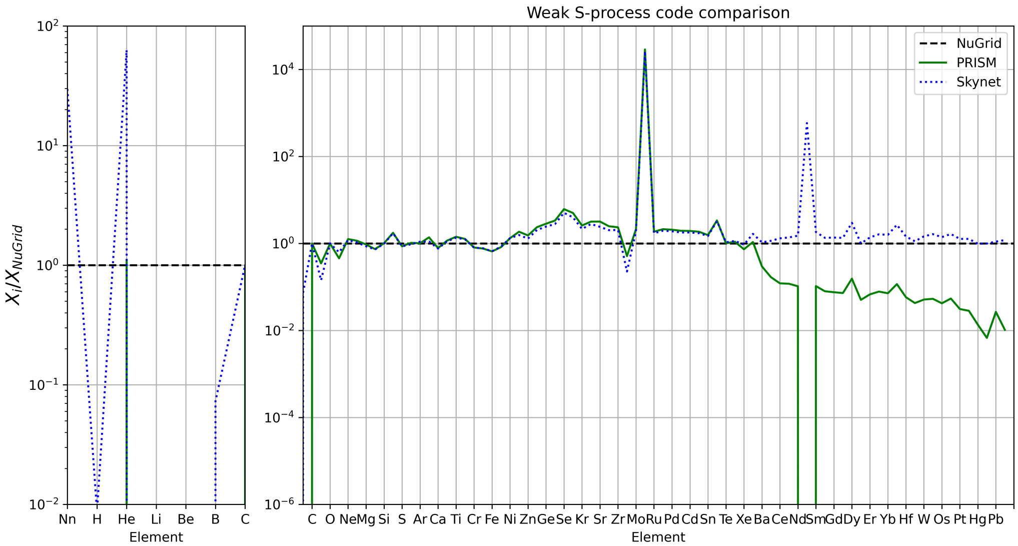

Figure 4.7: Ratios of elemental mass fractions for PRISM (Green) and SkyNet (Blue) compared to NuGrid (Black dashed horizontal line) are shown. This represents the over or under production of each element when compared to the NuGrid mass fraction. Elements below Carbon are shown in the left figure, and elements above Carbon are shown on the right.

Figure 4.7 shows the ratio of elemental mass fraction from both SkyNet and PRISM compared to NuGrid and other than elements below carbon and the unstable elements Technetium and Promethium there is clear consistency across the codes.

Figure 4.7 shows the ratio of elemental mass fraction from both SkyNet and PRISM compared to NuGrid, and shows that the mass fractions for elements heavier than carbon are all within a factor of 10, with the exception of technetium and promethium (again the difference in these elements is due to the different decay data used in each code). However, the destruction of isotopes above Barium in PRISM highlights the importance of ensuring these environments are run in more than one post processing network.

4.2.4 Common envelope with $128 \times 10^{-5} M_{\odot} s^{-1}$ accretion rate

The final environment used in the code comparison are common envelope accretion disk trajectories. For the $128 \times 10^{-5} M_{\odot} s^{-1}$ trajectory the peak temperature reached is 8.78 GK. As this is a relatively new scenario the type of nucleosynthesis that occurs is not fully known. The resulting elemental mass fractions are shown in figure 4.8 and each code shows a similar shape. All codes destroy a large fraction of elements between carbon and cobalt but to different extents. NuGrid has the highest fraction of elements in this region, followed by SkyNet, then Nucleo and PRISM has the lowest fraction in this region. For elements between Nickel strontium are produced but with PRISM having the largest mass fractions. Followed by SkyNet and Nucleo, which both have very similar mass fractions, and then NuGrid with the lowest mass fractions for elements in this region. This is a result of the temperature evolution of the trajectory. The material is quickly heated to 3 GK, before steadily climbing up to 8.78 GK. During this rapid proton capture reactions produce elements heavier than iron and destroy elements bellow iron until it reaches NSE, at which point the elements heavier than iron undergo photodissociation and are then destroyed via the inverse production reaction, proton emission. The most abundant element in SkyNet, PRISM and Nucleo is zinc with mass fractions of 0.344, 0.344 and 0.363 respectively, but the most abundant element in NuGrid is copper with a mass fraction of 0.466. The mass fraction of zinc in NuGrid is 0.270, which means that SkyNet and PRISM produce 127% of this and Nucleo produces 135% of this.

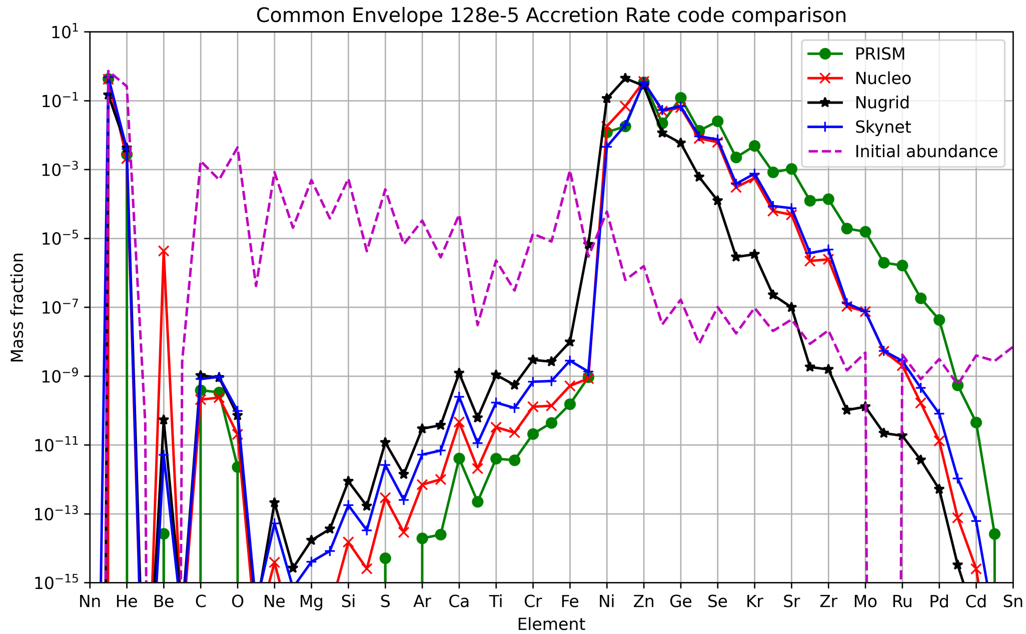

Figure 4.8: Final elemental mass fractions for a common envelope accreting $128 \times 10^{-5} M_{\odot} s^{-1}$. NuGrid is shown using black stars, PRISM is shown using green circles, Nucleo is shown using red X's and SkyNet is shown using blue crosses.

Figure 4.9 shows the extent of the differences produced by Nucleo, SkyNet and PRISM when compared to NuGrid. From this it is clear that SkyNet produces elemental mass fractions between neon and iron that are an order of magnitude smaller than the mass fractions produced by NuGrid, Nucleo produces elemental mass fractions nearly two orders of magnitude smaller for this range of elements. In PRISM, between Oxygen and Argon, excluding Sulphur, and all elements above Indium are below the mass fraction threshold, and are assumed to have zero contribution to the total PRISM mass fraction. SkyNet is the only code that produces a very small fraction of neutrons, and as NuGrid does not produce neutrons figure 4.9 shows a peak in SkyNet. However, the mass fraction of neutrons in SkyNet is 1.52×10^{-37}, which is smaller than the convergence criteria (therefore smaller than the associated uncertainty) and can be disregarded.

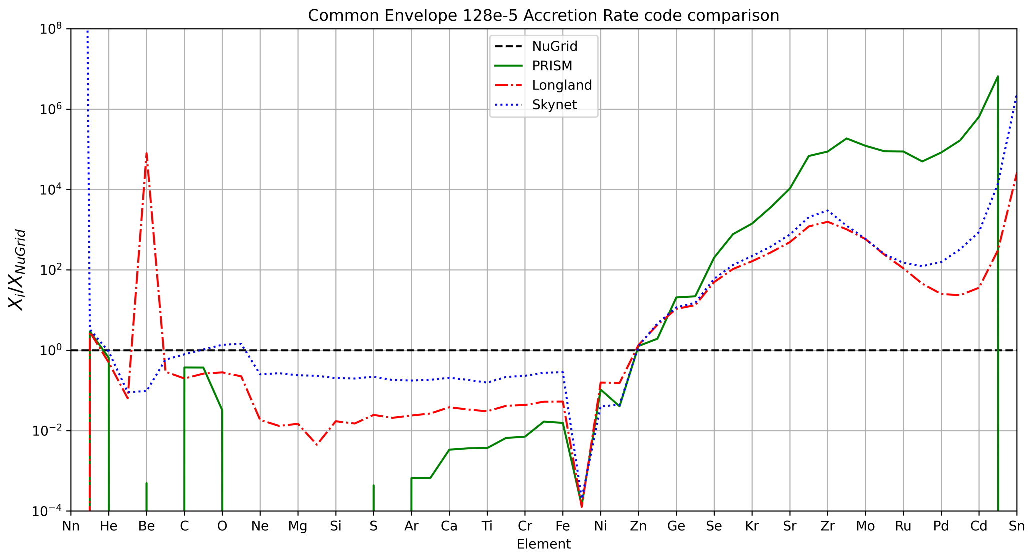

Figure 4.9: Ratios of elemental mass fractions for PRISM (Green), SkyNet (Blue), and Nucleo (Red) compared to NuGrid (Black dashed horizontal line) are shown. This represents the over or under production of each element when compared to the NuGrid mass fraction. Elements below Carbon are shown in the left figure, and elements above Carbon are shown on the right.

Overall the elemental mass fraction shape produced in NuGrid, PRISM, SkyNet and Nucleo are the same. However, there are significant differences, greater than an order of magnitude, between the codes. This highlights how these post processing codes can vary when modelling extreme environments such as this common envelope. If the results from PPN codes are then used to study galactic chemical evolution (GCE) the choice of code may significantly impact the GCE study.

4.2.5 Common envelope with $8 \times 10^{-5} M_{\odot} s^{-1}$ accretion rate

The final scenario used in this comparison is a low accretion rate common envelope accretion disk. Figure 4.8 shows the final mass fractions for a common envelope with $8 \times 10^{-5} M_{\odot} s^{-1}$ feeding the accretion disk with a peak temperature of 1.69 GK. This trajectory has a much lower peak temperature and so does not enter NSE, but proton captures are still the dominant reactions. NuGrid, PRISM and SkyNet all produce the same mass fraction pattern. There are some small differences in mass fractions, for example the Vanadium abundance lowest in NuGrid, but SkyNet produces 10% more than NuGrid and PRISM produces 24% more vanadium than NuGrid.

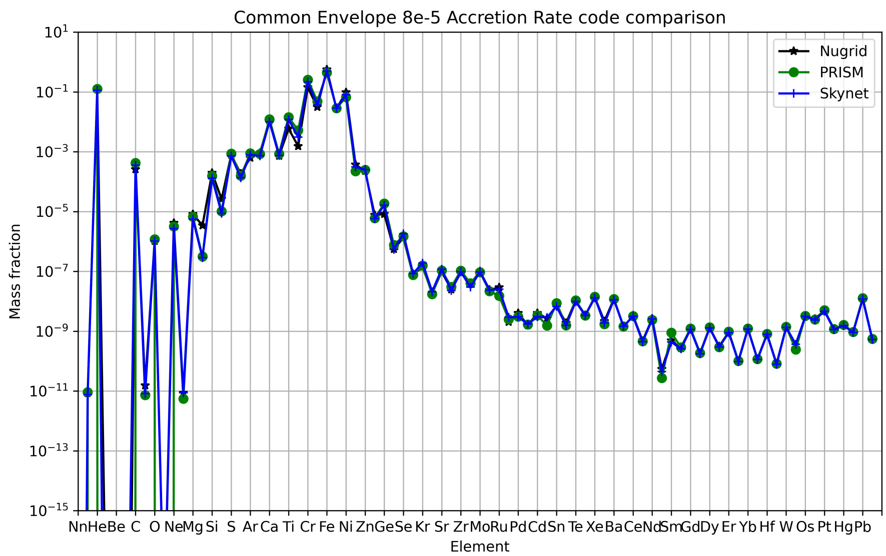

Figure 4.10: Final elemental mass fractions for a common envelope accreting $8 \times 10^{-5} M_{\odot} s^{-1}$. NuGrid is shown using black stars, PRISM is shown using green circles and SkyNet is shown using blue crosses.

Figure 4.11 shows the ratio of elemental mass fraction produced in SkyNet and PRISM compared to NuGrid. Unlike the previous scenarios (not including the simple hydro-static burn trajectory) this trajectory produced elemental mass fractions for elements above Carbon that are within an order of magnitude of NuGrid. The largest discrepancies are with the Nitrogen and Aluminium mass fractions. The Nitrogen abundance in all three codes is below the mass threshold, therefore PRISM assumes this as zero contribution and does not have a ratio within an order of magnitude. The difference in Aluminium mass fraction is a result of NuGrid containing a decay for the ^{26}Al meta-stable state from [46] that is not included in SkyNet or PRISM.

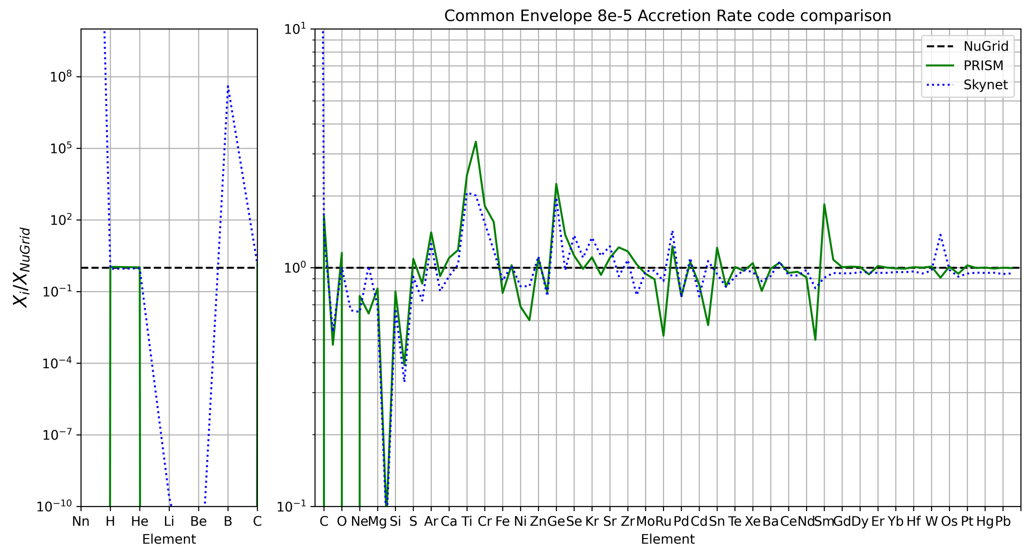

Figure 4.11: Ratios of elemental mass fractions for PRISM (Green) and SkyNet (Blue) compared to NuGrid (Black dashed horizontal line) are shown. This represents the over or under production of each element when compared to the NuGrid mass fraction. Elements below Carbon are shown in the left figure, and elements above Carbon are shown on the right.

4.3 Conclusions from PPN code comparisons

As seen in this chapter there are many factors to consider when using Post Processing Nucleosynthesis networks and choosing the correct network for a specific scenario is important. Each code used in this comparison was carefully adapted to use the same input nuclear physics and the same size network. However, most users of software such as these will not be aware of the impact that different reaction rate libraries may have, or how significant the differences may be when using a different network for the same scenario. All the subsequent common envelope data presented was produced using NuGrid, as there is more functionality than the other three codes. NuGrid provides detailed reaction flux data for each time-step of the simulation, as well as providing isotopic mass fractions for each isotope in the network at each time-step. SkyNet only provides elemental or isobaric mass fractions for the final time-step, and only stores the proton, neutron and alpha particle mass fraction evolution. PRISM was designed for neutron rich nucleosynthesis and evidence from [31] shows that proton rich nucleosynthesis may occur during common envelope accretion. Nucleo was not used as the maximum network size is limited to 1500 isotopes, whereas NuGrid can run 5200 isotopes in the network.

Chapter 5

Nucleosynthesis Results in Common Envelope Scenarios

This chapter presents the results for a range of common envelope trajectories where the accretion rate, neutron star mass, angular momentum and initial composition are varied. Depending on the accretion rate and initial composition different reaction pathways are used, and at large accretion rates the same isotopic and elemental mass fraction distributions are reached as the high accretion rates lead to NSE.

5.1 Description of the common envelope trajectories

As neutron star common envelopes are an active area of research the nucleosynthetic processes that occur inside the accretion disk are not well known, and so distinguishing the resulting explosion at the end of the CE phase from other supernova is currently not possible. Further understanding of the composition of the material ejected back into the envelope from the accretion disk will provide an insight into the possible observables that can come from the explosions at the end of the common envelope phase. Studies such as [31] and [29] have investigated the accretion process and provide a preliminary look into the type of material that can be ejected but focus more on the accretion and ejection processes. This chapter will further investigate the nucleosynthetic processes and resulting elemental and isotopic mass distributions using trajectories developed from [31] with the inclusion of angular momentum of the accreted material.

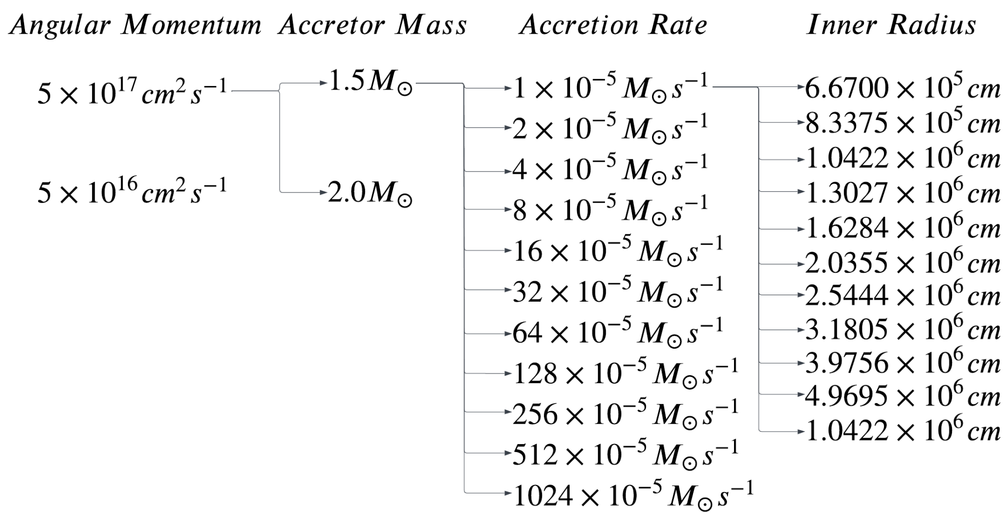

Figure 5.1: A flow chart breaking down the different aspects of each common envelope trajectory run.

Figure 5.1 shows the components of each trajectory run. Two different angular momenta were investigated, each for two different neutron star masses coming to four different scenarios. Each of these scenarios has 11 different potential accretion rates depending on the separation of the neutron star and its companion. Each of these accretion rates form an accretion disk around the neutron star, as disk winds eject material at different points within the disk each accretion rate is broken down into ten different inner radii where material is then ejected. Figure 5.2 shows how the different inner radii impact the shape of the temperature and density evolution of a trajectory.

During the development of the trajectories, it was assumed that across the length of the trajectory the mass of the neutron star remains unchanged. To account for this each trajectory run is not treated as a completed evolution of the CE system, but instead used as a tracer trajectory, looking at a snapshot of the accreted material and seeing how it evolves in a steady state scenario (i.e. no change in neutron star mass or change in angular momentum). Therefore, each trajectory investigated is not a complete component of the CE evolution, but a snapshot investigating how the composition of a packet of material that is accreted into the disk at a specific rate will change.

5.2 Contribution to ejecta from different inner radii

During accretion approximately 10 to 20% of the accreted material is ejected along the axis of rotation [20]. As the material falls towards the neutron star surface a fraction of the material is heated to beyond escape velocity and able to escape the accretion disk. This ejecta is the focus of this study as the material will be mixed into the envelope which is then ejected into the interstellar medium at the end of the common envelope phase. Understanding the composition of the

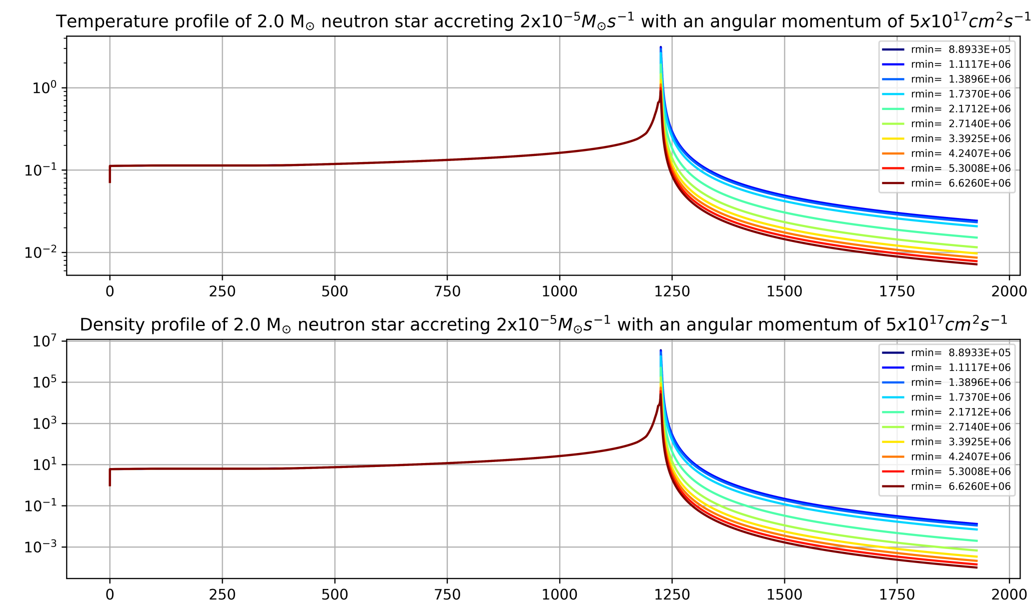

Figure 5.2: Temperature (GK) and density (gcm) against time (seconds) for a 2.0 M$_\odot$ neutron star accreting $2 \times 10^{-5} M_\odot s^{-1}$ and an angular momentum of $5 \times 10^{17} cm^2 s^{-1}$.

During the common envelope phase the accretion disk ejects some material from the disk as it falls towards the neutron star, leading to constant winds from the accretion disk back into the envelope. To model this ten different inner radii are assumed. At each of these points the material is ejected via turbulent winds from inside the disk and cools as it returns to the envelope. As the material falling in the disk follows the same path the trajectories are similar, as shown by figure 5.2, but the peak temperature reached increases for each trajectory that gets closer to the neutron star surface and the material ejected at each inner radii cools to a different final temperature. Elemental mass fractions ejected at ten different inner radii for a $2M_{\odot}$ neutron star accreting $2\times10^{-5}M_{\odot}s^{-1}$ with an angular momentum of $5\times10^{17}cm^2s^{-1}$ are shown in figure 5.3. The plot in the top left of the figure shows the elemental mass fractions from material ejected closest to the surface of the neutron star and the plot in the bottom right of the figure shows the results from material ejected at the furthest point from the neutron star. From this it is clear that as the material approaches the the neutron star nucleosynthesis destroys low mass isotopes and the bulk of the material is pushed further up the nuclear chart.

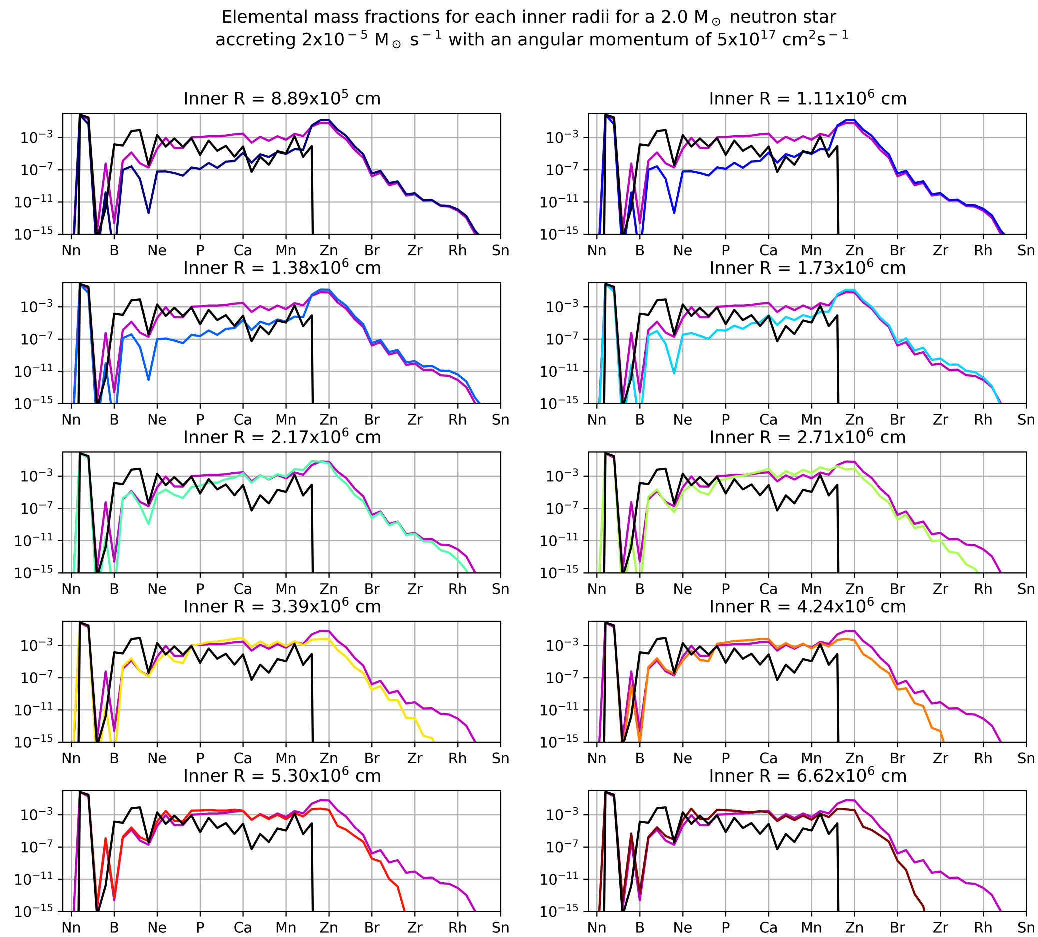

Figure 5.3: Elemental mass fractions for each inner radii for a 2.0 $M_\odot$ neutron star accreting $2 \times 10^{-5} M_\odot s^{-1}$ and an angular momentum of $5 \times 10^{17} cm^2 s^{-1}$ The black line in each plot shows the initial abundance of the trajectory and the magenta lines show the averaged elemental mass fraction across all inner radii.

The contribution from each inner radius model is assumed to be equal and so an average mass fraction can be calculated, as shown in each plot by the magenta line. The average shows that the material produced closest to the neutron star surface does not produce the largest mass fraction of heavy elements such as rhodium and palladium, these elements are produced when the material is ejected $1.38{\times}10^6$cm away from the neutron star surface. It is also clear that the contribution to isotopes below iron is mostly from trajectories that do not get closer than 2.17×10^6cm to the neutron star. The four largest inner radii trajectories produce very similar mass fraction distributions for elements between silicon and calcium, as shown by the plateau. These trajectories produce equal mass fractions of calcium and iron, but trajectories with inner radii closer to the neutron star produce higher mass fractions of iron group elements and the silicon to calcium region is destroyed. The average mass fraction (shown in magenta in figure 5.3) preserves the plateau between silicon and calcium seen at high inner radii while also showing the larger zinc mass fraction seen in the innermost radii. Even though these trajectories follow the same initial temperature and density evolution they reach different peak temperatures and cool the material at different rates during ejection. Overall the average mass fraction accurately represents the final composition of the ejected material mixed back into the envelope.

The maximum temperatures of these trajectories varies between 0.910 GK and 3.11 GK, which is below the expected NSE temperature region. As many high accretion rate trajectories have peak temperatures within the NSE temperature range the amount of time spent in NSE may affect the resulting final elemental and isotopic mass fractions. Figure 5.4 shows the temperature and density profile of a $2\mathrm{M}_{\odot}$ neutron star accreting $512\times10^{16}\mathrm{M}_{\odot}s^{-1}$ with an angular momentum of $5\times10^{16}cm^2s^{-1}$. This is a lower angular momentum trajectory and so the material spends more time in the accretion disk and is able to reach higher temperatures as a result. The peak temperatures range from 3.638 GK up to 12.41 GK. This range spans the expected NSE temperatures however as NuGrid is only able to post process material up to 10 GK the closest four inner radii (8.89×10^5 to 1.74×10^6cm) must be excluded from the average as these exceed this temperature limit.

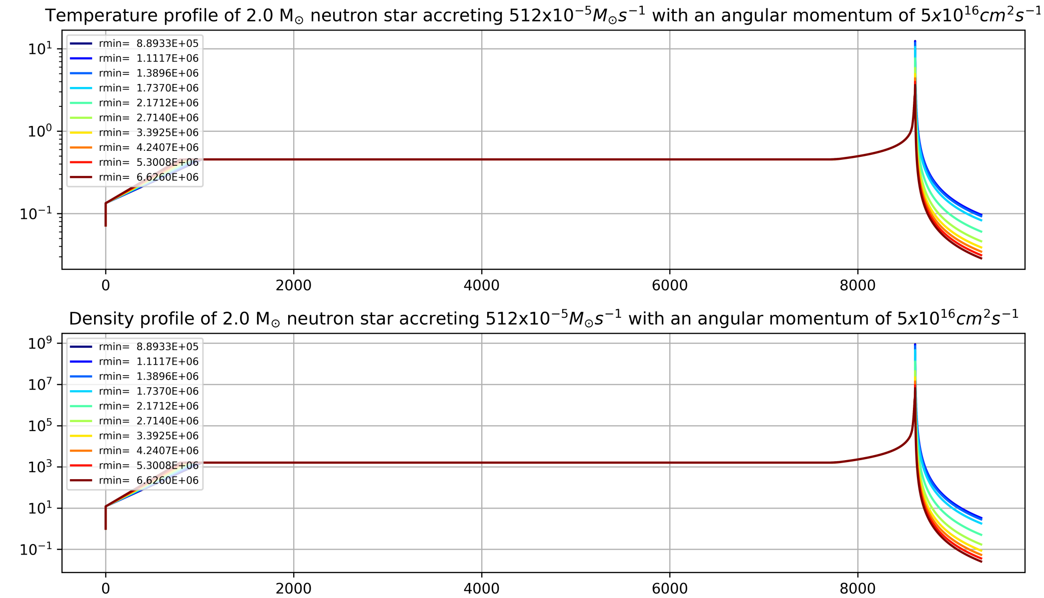

Figure 5.4: Temperature and density evolution for a 2.0 $M_\odot$ neutron star accreting $512 \times 10^{-5} M_\odot s^{-1}$ and an angular momentum of $5 \times 10^{16} cm^2 s^{-1}$.

The final elemental mass fractions for the six inner radii with peak temperatures below 10 GK are shown in figure 5.5. Nickel has the largest mass fraction at every inner radii, and it is clear that for inner radii between 3.39×10^6 cm and 6.62×10^6 cm almost identical elemental mass fraction distributions are produced. For the lowest two inner radii, elements between boron and nickel are destroyed and elements above nickel are produced. Like before with the $2 \times 10^{-5} M_\odot s^{-1}$ accretion rate trajectory the resulting average mass fraction distribution preserves details produced from individual inner radii, in figure 5.5 the average mass fraction for elements above zinc is much higher than the mass fractions produced for all inner radii other than 2.71×10^6cm. As material is ejected constantly during free fall through the accretion disk this average ensures that these elements are included in the final composition of the material. Overall the average represents the composition of material ejected from the accretion disk very accurately.

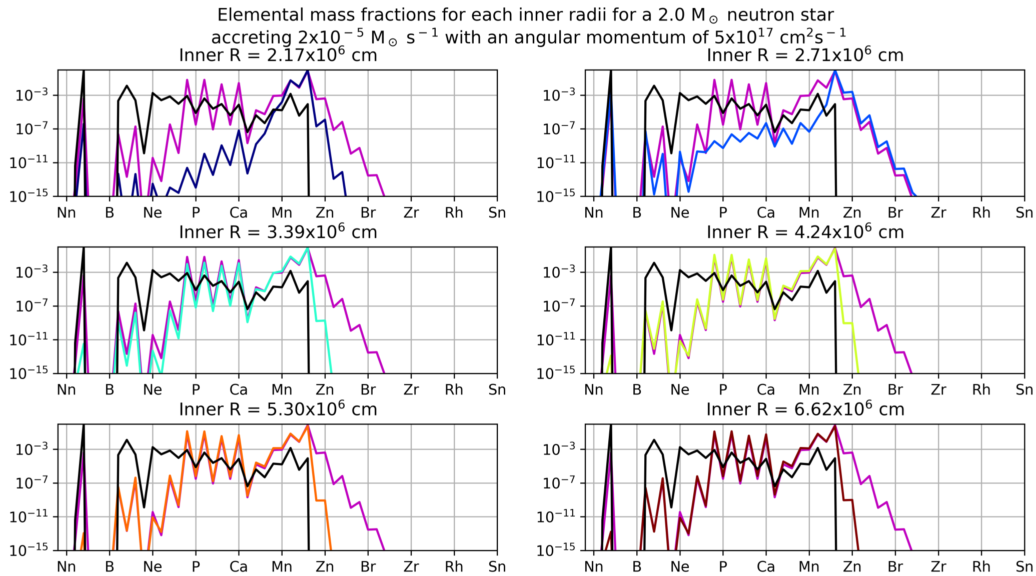

Figure 5.5: Elemental mass fractions for each inner radii for a 2.0 $M_\odot$ neutron star accreting $512\times10^{-5}M_\odot s^{-1}$ and an angular momentum of $5\times10^{16}cm^2s^{-1}$. The black line in each plot shows the initial abundance of the trajectory and the magenta lines show the averaged elemental mass fraction across all inner radii.

Further investigation into the reaction flux, as shown in figure 5.6, show that not all inner radii reach full NSE. These plots show the integrated reaction flux at the peak temperature, around the nickel region for reactions within two orders of magnitude of the reaction with the highest flux. For the inner radii larger than 3.39×10^6cm it is not in full NSE as there are still unbalanced forward and reverse reactions such as the ^{54}Fe(p,γ) and the ^{65}Ni(γ,p), for which the inverse proton emission does not occur. The reaction flux seen in the left most plot of figure 5.6 is for the 2.17×10^6cm inner radius and demonstrates the expected flux for the NSE state. The central plot shows the flux for the next inner radius out and from this it is clear that at the peak temperature conditions are close to NSE with many forward and reverse reactions being balanced, however there are still unbalanced (p,n) and (n,p) reactions between isotopes of cobalt and nickel and the ^{53}Fe(p,n) reaction is only active in the forward direction.

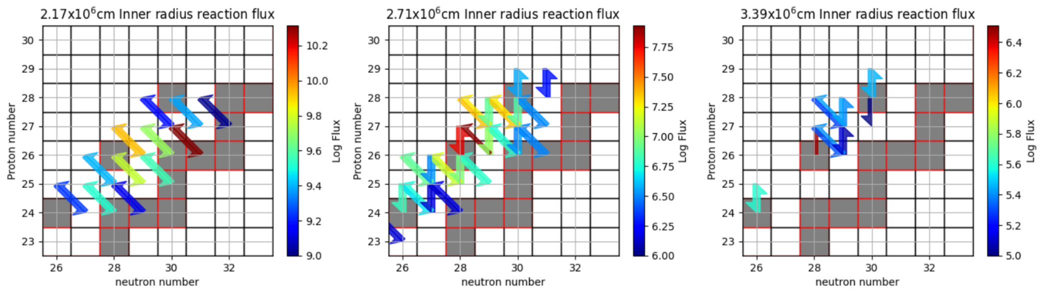

Figure 5.6: Integrated reaction fluxes ($\Sigma \frac{dY}{dt}$) for three different inner radii for a 2.0 M$_\odot$ neutron star accreting $512 \times 10^{-5} M_\odot s^{-1}$ and an angular momentum of $5 \times 10^{16} cm^2 s^{-1}$. The boxes in grey show stable isotopes.

From figures 5.5 and 5.6 it is clear that the high peak temperatures and densities can lead to NSE nucleosynthesis, however each trajectory that has a peak temperature within the NSE temperature range cannot be assumed to produce the same elemental and isotopic mass fractions. The averaged elemental mass fraction is still required for NSE trajectories, however as the NSE data will produce high mass fractions of iron peak elements separate averages will be taken for NSE and non-NSE mass fraction distributions.

5.3 Initial abundance variations for different age and mass companions

The common envelope scenario studied in this investigation consists of a neutron star and a companion expanding as it enters the core helium burning phase. As the companion star expands and engulfs the neutron star to form a common envelope, the quantity and composition of the material entering the accretion disk surrounding the neutron star is dictated by the position of the neutron star inside the common envelope relative to the core of the companion. Two different masses of neutron star were investigated, $1.5M_\odot$ and $2M_\odot$, each modelled inside a companion envelope of 12, 15 and $20M_\odot$ at three different times after the companion has undergone expansion into the red supergiant phase. The age of the companion stars as they expand is shown at the top of figures 5.7, 5.8 and 5.9. Each age will be referred to as either early, mid or late phase expansion as these points occur at different times for the different companion masses.

Early phase expansion occurs when a $12M_\odot$ star is 1.7582×10^7 years old, when a $15M_\odot$ star is 1.256×10^7 years old and when a $20M_\odot$ star is 8.746×10^6 years old. Mid phase expansion occurs when a $12M_\odot$ star is 1.7597×10^7 years old, when a $15M_\odot$ star is 1.257×10^7 years old and when a $20M_\odot$ star is 8.780×10^6 years old. Then the late expansion phase occurs when a $12M_\odot$ star is 1.7604×10^7 years old, when a $15M_\odot$ star is 1.258×10^7 years old and when a $20M_\odot$ star is 9.028×10^6 years old.

For each combination of neutron star mass, angular momentum, companion mass and companion age a set of trajectories for eleven accretion rates have been calculated using Bondi-Hoyle accretion approximations as detailed in section 2.3. The accretion rate is dictated in part by the density of the material in the common envelope, which is directly dependant by the radial position of the neutron star relative to the core of the companion. Using MESA stellar models for massive stars taken from [54] exact compositions can be calculated for each accretion rate across all companion masses and ages after expansion. Figures 5.7, 5.8 and 5.7 show the distribution of hydrogen and helium as a function of distance from the core of a $12M_\odot$ star as it undergoes expansion into the core helium burning phase. Table 5.1 shows the accretion rate, radial position inside the companion star and hydrogen mass fraction for all common envelopes assessed. For some of the highest accretion rates there are no positions within the envelope that can provide the required mass transfer due to limitations as a result of the Bondi-Hoyle accretion rate, and so these will not be included in the final analysis.

The resulting isotopic and elemental mass fraction distributions can be grouped into three main classifications: those that reach NSE, those that do not and those accretion rates that partially enter NSE. NSE can be identified by looking at the ratio of isotopic mass fraction at the peak temperature compared to the isotopic ratio just before the peak temperature. The left figure in figure 5.10 shows the ratio of isotopic mass fractions at the peak temperature compared to ten time-steps before it for a trajectory entirely in NSE. For NSE trajectories this type of ratio will show material flow from unstable nuclei back to stability. In the case of the common envelope this is seen in the form of unstable proton rich isotopes being destroyed and stable isotopes being produced, as shown by the large over production ratios for isotopes along the valley of stability. It is also crucial to highlight the creation of isotopes on the proton rich side of the valley of stability within the germanium to krypton range. These isotopes

Table 5.1: Given accretion rate and closest corresponding accretion rate, radial distance and hydrogen mass fraction from [54] MESA data.

	M12								
	early phase			mid phase			late phase		
Accretion Rate in trajectory $M_\odot s^{-1}$	Acc Rate in MESA $M_\odot s^{-1}$	Log Radius $\frac{R}{R_\odot}$	H mass fraction	Acc Rate in MESA $M_\odot s^{-1}$	Log Radius $\frac{R}{R_\odot}$	H mass fraction	Acc Rate in MESA $M_\odot s^{-1}$	Log Radius $\frac{R}{R_\odot}$	H mass fraction
1.000×10^{-5}	1.007×10^{-5}	3.341	7.064×10^{-1}	1.006×10^{-5}	2.183	5.937×10^{-1}	1.011×10^{-5}	1.443	4.025×10^{-1}
2.000×10^{-5}	2.041×10^{-5}	1.769	6.824×10^{-1}	1.989×10^{-5}	1.232	4.526×10^{-1}	2.000×10^{-5}	8.206×10^{-1}	3.673×10^{-1}
4.000×10^{-5}	4.042×10^{-5}	9.528×10^{-1}	4.930×10^{-1}	$4.001\times10^{-5}1$	6.519×10^{-1}	3.672×10^{-1}	4.006×10^{-5}	7.077×10^{-1}	1.914×10^{-1}
8.000×10^{-5}	8.074×10^{-5}	5.899×10^{-1}	3.172×10^{-1}	7.991×10^{-5}	5.824×10^{-1}	1.766×10^{-1}	7.994×10^{-5}	5.330×10^{-1}	1.476×10^{-1}
1.600×10^{-4}	1.608×10^{-4}	5.254×10^{-1}	1.385×10^{-1}	1.591×10^{-4}	4.408×10^{-1}	1.037×10^{-1}	1.605×10^{-4}	4.002×10^{-1}	9.599×10^{-2}
3.200×10^{-4}	3.188×10^{-4}	4.363×10^{-1}	4.631×10^{-2}	3.142×10^{-4}	3.553×10^{-1}	3.401×10^{-2}	3.195×10^{-4}	3.196×10^{-1}	3.572×10^{-2}
6.400×10^{-4}	6.394×10^{-4}	3.731×10^{-1}	1.084×10^{-3}	6.394×10^{-4}	3.018×10^{-1}	1.527×10^{-3}	6.393×10^{-4}	2.745×10^{-1}	2.182×10^{-3}
1.280×10^{-3}	1.271×10^{-3}	3.006×10^{-1}	1.338×10^{-6}	1.294×10^{-3}	2.554×10^{-1}	5.779×10^{-8}	1.285×10^{-3}	2.363×10^{-1}	1.273×10^{-8}
2.560×10^{-3}	2.554×10^{-3}	1.947×10^{-1}	4.041×10^{-16}	2.569×10^{-3}	2.045×10^{-1}	7.782×10^{-18}	2.582×10^{-3}	1.939×10^{-1}	3.815×10^{-18}
5.120×10^{-3}	N/A	N/A	N/A	5.126×10^{-3}	1.329×10^{-1}	$1.215\times10^{-1}2$	5.114×10^{-3}	1.402×10^{-1}	1.233×10^{-12}
1.024×10^{-2}	N/A	N/A	N/A	N/A	N/A	N/A	1.024×10^{-2}	4.761×10^{-2}	1.640×10^{-20}

	M15								
	early phase			mid phase			late phase		
Accretion Rate in trajectory $M_\odot s^{-1}$	Acc Rate in MESA $M_\odot s^{-1}$	Log Radius $\frac{R}{R_\odot}$	H mass fraction	Acc Rate in MESA $M_\odot s^{-1}$	Log Radius $\frac{R}{R_\odot}$	H mass fraction	Acc Rate in MESA $M_\odot s^{-1}$	Log Radius $\frac{R}{R_\odot}$	H mass fraction
1.000×10^{-5}	1.001×10^{-5}	2.811	7.064×10^{-1}	9.890×10^{-6}	2.218	5.351×10^{-1}	9.980×10^{-6}	1.934	4.604×10^{-1}
2.000×10^{-5}	2.000×10^{-5}	1.618	5.358×10^{-1}	2.001×10^{-5}	8.541×10^{-1}	4.604×10^{-1}	2.002×10^{-5}	8.498×10^{-1}	4.604×10^{-1}
4.000×10^{-5}	3.998×10^{-5}	5.493×10^{-1}	4.669×10^{-1}	3.815×10^{-5}	4.620×10^{-1}	3.490×10^{-1}	4.005×10^{-5}	4.294×10^{-1}	4.566×10^{-1}
8.000×10^{-5}	7.558×10^{-5}	5.413×10^{-1}	2.299×10^{-1}	8.853×10^{-5}	4.599×10^{-1}	8.142×10^{-2}	8.199×10^{-5}	3.983×10^{-1}	2.265×10^{-1}
1.600×10^{-4}	1.594×10^{-4}	5.080×10^{-1}	6.149×10^{-2}	1.578×10^{-4}	4.011×10^{-1}	4.532×10^{-2}	1.588×10^{-4}	3.878×10^{-1}	6.733×10^{-2}
3.200×10^{-4}	3.227×10^{-4}	4.375×10^{-1}	9.891×10^{-3}	3.241×10^{-4}	3.473×10^{-1}	8.074×10^{-3}	3.281×10^{-4}	3.422×10^{-1}	2.276×10^{-2}
6.400×10^{-4}	6.421×10^{-4}	3.763×10^{-1}	5.019×10^{-5}	6.350×10^{-4}	3.080×10^{-1}	2.854×10^{-5}	6.423×10^{-4}	3.107×10^{-1}	4.520×10^{-4}
1.280×10^{-3}	1.280×10^{-3}	3.003×10^{-1}	2.721×10^{-14}	1.276×10^{-3}	2.628×10^{-1}	1.095×10^{-14}	1.280×10^{-3}	2.741×10^{-1}	6.641×10^{-16}
2.560×10^{-3}	2.558×10^{-3}	1.730×10^{-1}	1.752×10^{-12}	2.557×10^{-3}	2.039×10^{-1}	6.323×10^{-13}	2.555×10^{-3}	2.244×10^{-1}	1.223×10^{-13}
5.120×10^{-3}	N/A	N/A	N/A	5.119×10^{-3}	1.137×10^{-1}	0.000	N/A	N/A	N/A

	M20								
	early phase			mid phase			late phase		
Accretion Rate in trajectory $M_\odot s^{-1}$	Acc Rate in MESA $M_\odot s^{-1}$	Log Radius $\frac{R}{R_\odot}$	H mass fraction	Acc Rate in MESA $M_\odot s^{-1}$	Log Radius $\frac{R}{R_\odot}$	H mass fraction	Acc Rate in MESA $M_\odot s^{-1}$	Log Radius $\frac{R}{R_\odot}$	H mass fraction
1.000×10^{-5}	9.936×10^{-6}	2.258	5.946×10^{-1}	9.999×10^{-6}	1.421	5.152×10^{-1}	1.001×10^{-5}	$1.215\times10^{+}0$	5.147×10^{-1}
2.000×10^{-5}	2.002×10^{-5}	1.019	5.071×10^{-1}	1.995×10^{-5}	5.386×10^{-1}	4.797×10^{-1}	1.992×10^{-5}	5.672×10^{-1}	4.724×10^{-1}
4.000×10^{-5}	3.838×10^{-5}	6.387×10^{-1}	3.492×10^{-1}	4.085×10^{-5}	4.675×10^{-1}	3.251×10^{-1}	4.081×10^{-5}	4.999×10^{-1}	2.932×10^{-1}
8.000×10^{-5}	8.653×10^{-5}	6.357×10^{-1}	8.885×10^{-2}	9.504×10^{-5}	4.544×10^{-1}	9.980×10^{-2}	8.000×10^{-5}	4.773×10^{-1}	1.411×10^{-1}
1.600×10^{-4}	1.594×10^{-4}	5.830×10^{-1}	2.312×10^{-2}	1.608×10^{-4}	4.460×10^{-1}	8.620×10^{-3}	1.613×10^{-4}	4.571×10^{-1}	2.377×10^{-2}
3.200×10^{-4}	3.196×10^{-4}	5.108×10^{-1}	2.704×10^{-4}	3.212×10^{-4}	4.113×10^{-1}	1.276×10^{-4}	3.200×10^{-4}	4.225×10^{-1}	2.964×10^{-8}
6.400×10^{-4}	6.413×10^{-4}	4.188×10^{-1}	3.216×10^{-10}	6.409×10^{-4}	3.697×10^{-1}	2.145×10^{-15}	6.429×10^{-4}	3.711×10^{-1}	1.047×10^{-17}
1.280×10^{-3}	1.282×10^{-3}	2.668×10^{-1}	2.108×10^{-12}	1.277×10^{-3}	3.099×10^{-1}	1.284×10^{-13}	1.280×10^{-3}	2.896×10^{-1}	9.595×10^{-13}
2.560×10^{-3}	N/A	N/A	N/A	2.559×10^{-3}	1.384×10^{-1}	0.000	2.559×10^{-3}	1.456×10^{-1}	2.950×10^{-20}

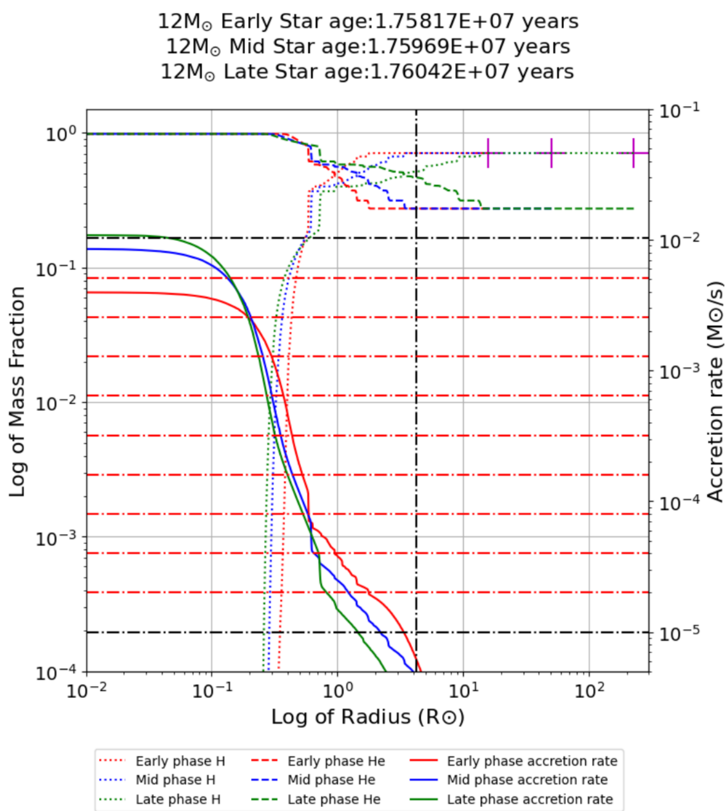

Figure 5.7: The mass fraction of Hydrogen (dotted lines) and Helium (dashed lines) and the associated accretion rate (solid lines) as a function of distance to the centre of the $12M_{\odot}$ companion as it undergoes expansion into the core helium burning phase. The horizontal black dot dashed lines show the accretion rate limits with the red dot dashed lines showing each accretion rate. The vertical black dot dashed line shows the radius of the star before undergoing expansion. The magenta crosses show where the outer radius is at each stage in the expansion.

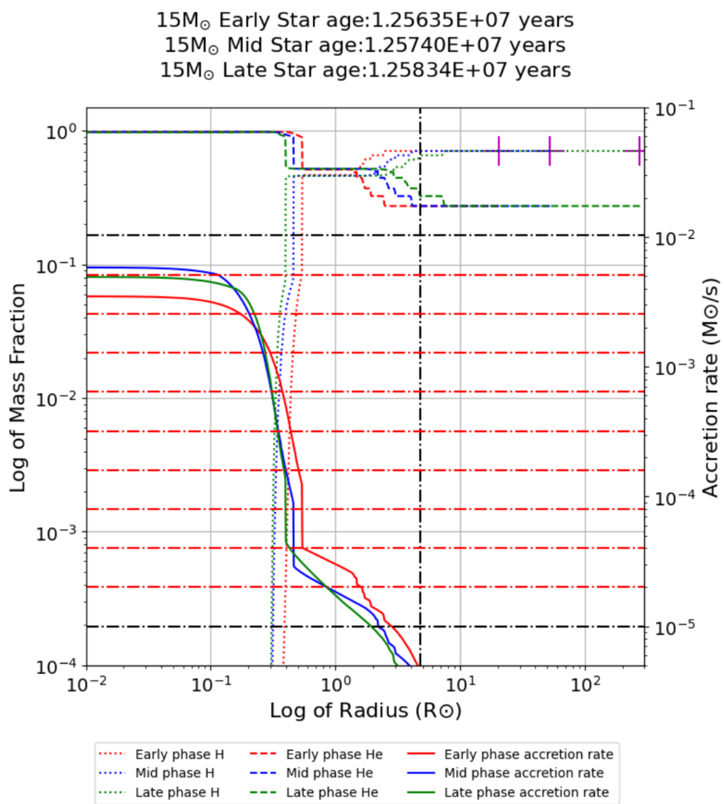

Figure 5.8: The mass fraction of Hydrogen (dotted lines) and Helium (dashed lines) and the associated accretion rate (solid lines) as a function of distance to the centre of the 15M$_\odot$ companion as it undergoes expansion into the core helium burning phase. The horizontal black dot dashed lines show the accretion rate limits with the red dot dashed lines showing each accretion rate. The vertical black dot dashed line shows the radius of the star before undergoing expansion. The magenta crosses show where the outer radius is at each stage in the expansion.

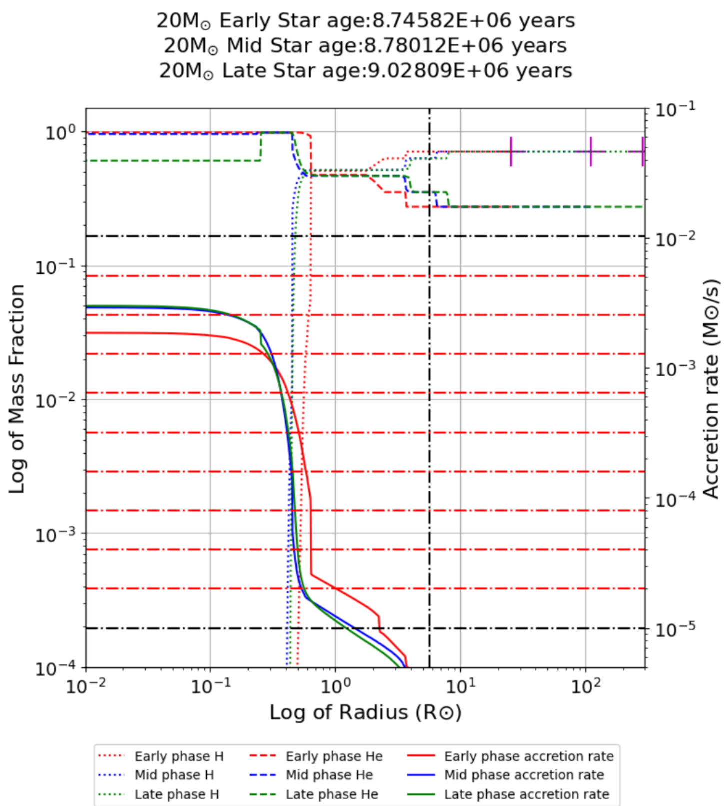

Figure 5.9: The mass fraction of Hydrogen (dotted lines) and Helium (dashed lines) and the associated accretion rate (solid lines) as a function of distance to the centre of the $20M_{\odot}$ companion as it undergoes expansion into the core helium burning phase. The horizontal black dot dashed lines show the accretion rate limits with the red dot dashed lines showing each accretion rate. The vertical black dot dashed line shows the radius of the star before undergoing expansion. The magenta crosses show where the outer radius is at each stage in the expansion.

are generated during nuclear statistical equilibrium (NSE) but have a minimal mass fraction prior to reaching peak temperature, leading to significant overproduction ratios.

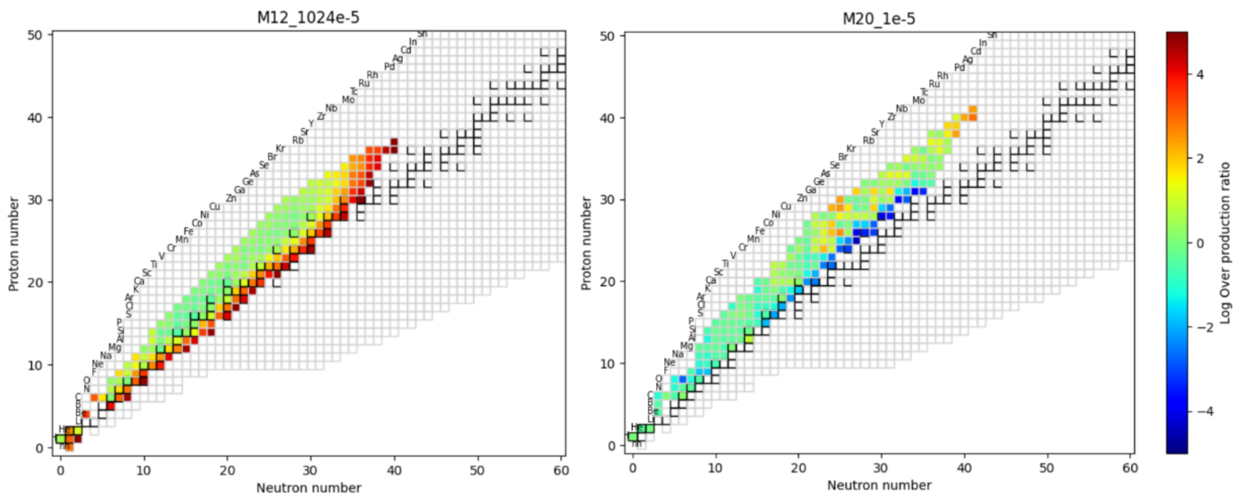

Figure 5.10: Left: The ratio of isotopic mass fractions for a $2M_\odot$ neutron star inside a $12M_\odot$ companion envelope accreting $1024 \times 10^{-5} M_\odot s^{-1}$ and an angular momentum of $5 \times 10^{17} cm^2 s^{-1}$. The ratio of mass fraction at the peak over mass fraction ten time-steps before the peak temperature is shown. Right: The ratio of isotopic mass fractions for a $1.5M_\odot$ neutron star inside a $20M_\odot$ companion envelope accreting $1 \times 10^{-5} M_\odot s^{-1}$ and an angular momentum of $5 \times 10^{16} cm^2 s^{-1}$

Non-NSE trajectories can be identified using the same ratio, as shown on the right side of figure 5.10. During the peak temperatures and densities these trajectories result in destruction of isotopes near the valley of stability to produce unstable nuclei.

5.3.1 $1\times10^{-5}M_{\odot}s^{-1}$ accretion rate

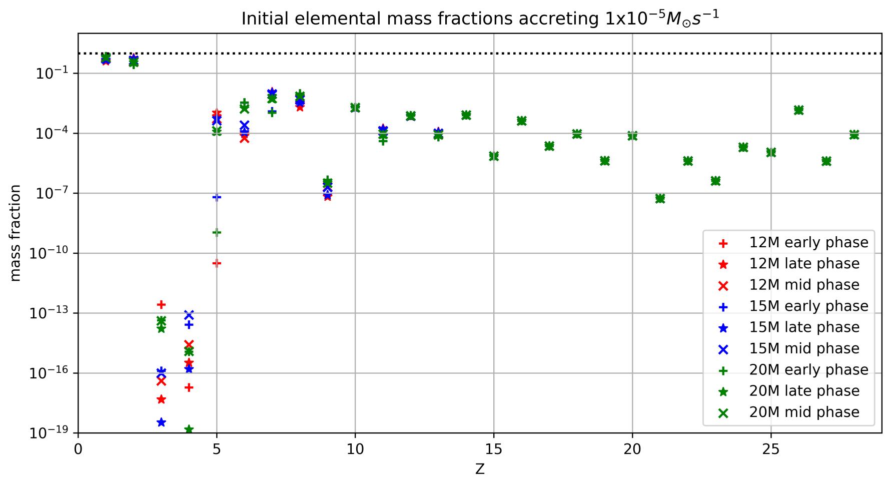

Figure 5.11: Initial elemental mass fractions for each environment for a common envelope accreting $1\times10^{-5}M_{\odot}s^{-1}$. Elements above Sodium are unaffected by the change in orbital position of the neutron star inside the common envelope.

The initial abundance variations for each companion at each phase after expansion are shown in figure 5.11. The initial abundances from [54] are for isotopes up to and including ^{62}Ni. The main differences in the composition from each companion are in elements between lithium and oxygen as the companions cycle through CNO fusion. Using table 5.1 the radial position dictates the composition of the envelope and therefore the composition of the material entering the accretion disk.

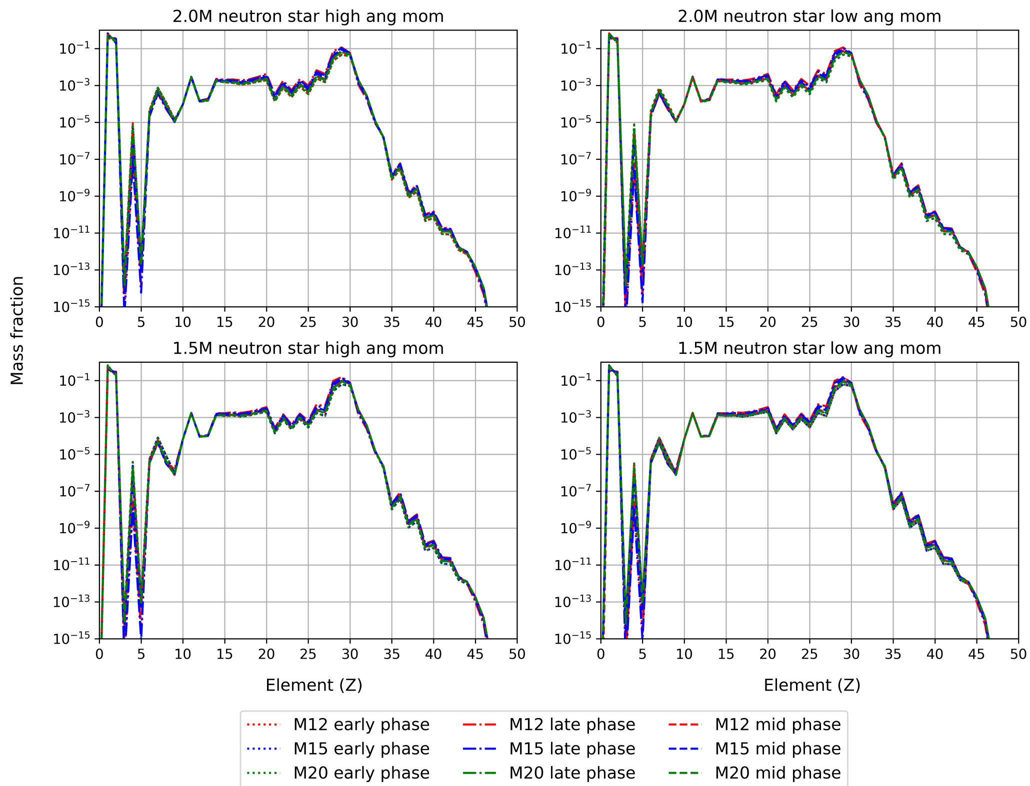

Figure 5.12: Elemental mass fraction distributions for each neutron star mass and angular momentum. Dotted lines represent the early phase expansion, dashed lines represent mid phase expansion and dot-dashed lines represent late phase expansion. Companion masses of 12M$_\odot$ are shown in red, 15M$_\odot$ in blue and 20M$_\odot$ in green.

Figure 5.12 shows the final elemental mass fraction distribution for an accretion rate of $1\times10^{-5}M_{\odot}s^{-1}$ in each environment for the different combinations of neutron star mass and angular momentum. For each of the nine different environments that were studied they all result in a similar mass fraction distribution. Comparing the results from the different neutron star masses the only differences in mass fraction are for the CNO isotopes. When accreting around a 1.5M$_\odot$ neutron star the carbon, nitrogen and oxygen mass fractions are an order of magnitude smaller when compared to the results from the 2.0M$_\odot$ neutron star. Figure 5.13 shows the time spent above 0.1GK for each trajectory. Both of the 1.5M$_\odot$ neutron star trajectories spend more time in this temperature region which then lead to the destruction of CNO isotopes via proton capture reactions. The $2M_{\odot}$ neutron star with $5 \times 10^{17} cm^2 s^{-1}$ has the largest final mass fraction for beryllium. This trajectory spends the least amount of time above 0.1 GK, the $1.5M_{\odot}$ neutron star with $5 \times 10^{16} cm^2 s^{-1}$ has the smallest beryllium mass fraction and spends the most time above 0.1 GK. The beryllium is mostly produced via alpha capture onto ^3He, which is produced via proton capture onto ^2H. Therefore, beryllium production is dependent on the initial hydrogen mass fraction and the destruction of beryllium is dependent on the time spent at high temperature. All the early expansion phase companions have the highest initial hydrogen mass fraction, and these all end with the highest beryllium mass fraction (for each different neutron star mass and angular momentum) and the second-highest initial hydrogen mass fraction is in the $20M_{\odot}$ late expansion phase, which provides the second-highest beryllium mass fractions.

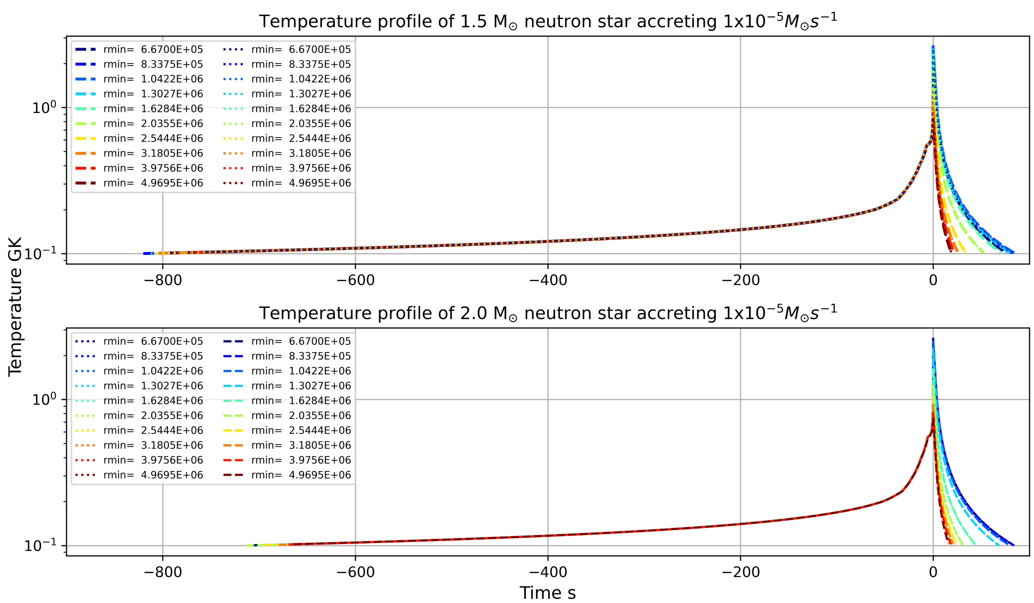

Figure 5.13: Time spent above 1 GK for all $1\times10^{-5} M_{\odot} s^{-1}$ accretion rate trajectories. Dotted lines show trajectories with an angular momentum of $5 \times 10^{17} cm^2 s^{-1}$, dashed lines show trajectories with an angular momentum of $5 \times 10^{16} cm^2 s^{-1}$

Figure 5.14 shows the same as figure 5.12 but for elements with mass fractions over 1×10^{-4}. Overall for each neutron star mass and angular momentum the late phase expansion in companions of $12M_\odot$ and $15M_\odot$ lead to a higher production of elements between silicon and zinc, followed by the mid expansion phase for a $15M_\odot$ companion. The late expansion phase $12M_\odot$ environment has the highest initial helium mass fraction and the lowest initial hydrogen mass fraction, H = 0.402 and He = 0.577, with the late expansion phase $15M_\odot$ environment having the second-highest initial helium and second-lowest hydrogen mass fraction, H = 0.460 and He = 0.519. The early expansion phases produce the lowest mass fraction of elements in this range and contains the highest initial fraction of hydrogen and lowest initial fraction of helium, H = 0.706 and He = 0.273. This indicates that elements in this region are predominantly produced via alpha capture reactions and the variation in mass fractions for these elements are a result of different initial helium mass fractions. There is less separation in the elemental mass fractions over the $1.5M_\odot$ neutron star trajectories, again this is due to the trajectory spending more time over 0.1GK. The variation in angular momentum does not impact the resulting mass fractions indicating that the proton and alpha capture reactions occur as the material rapidly heats up to the peak temperature. For this accretion rate the temperature in the accretion disk during this period is below 0.1GK.

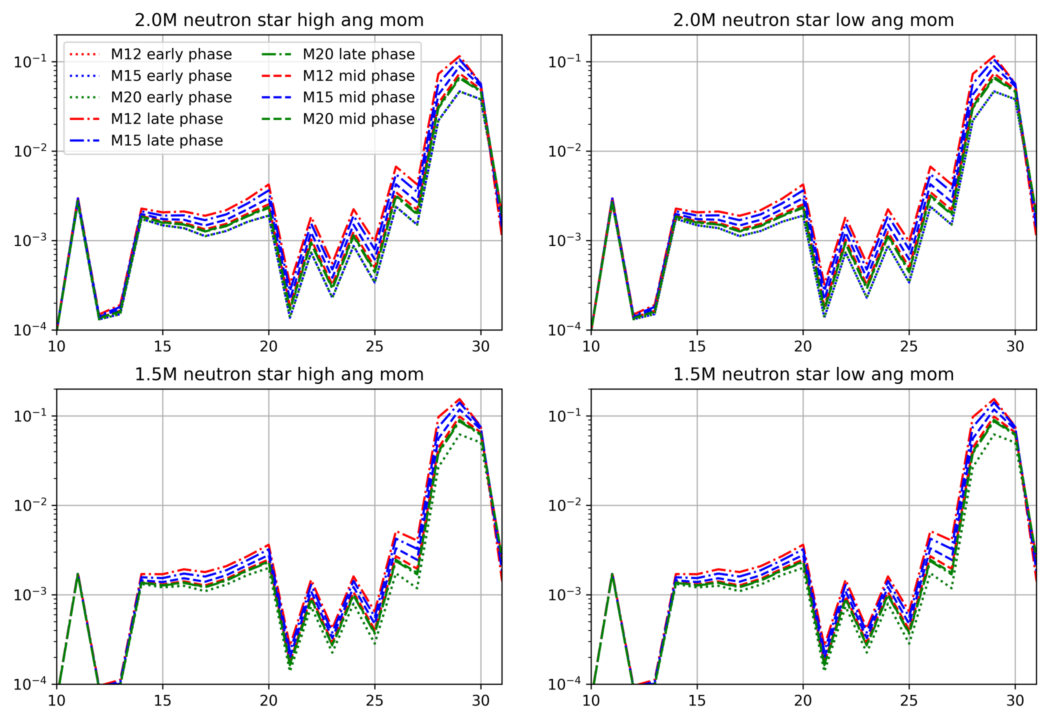

Figure 5.14: Elemental mass fraction distributions greater than 1×10^{-5} for each neutron star mass and angular momentum. Dotted lines represent the early phase expansion, dashed lines represent mid phase expansion and dot-dashed lines represent late phase expansion. Companion masses of $12\mathrm{M}_{\odot}$ are shown in red, $15\mathrm{M}_{\odot}$ in blue and $20\mathrm{M}_{\odot}$ in green.

5.3.2 $2{\times}10^{-5}M_{\odot}s^{-1}$ accretion rate

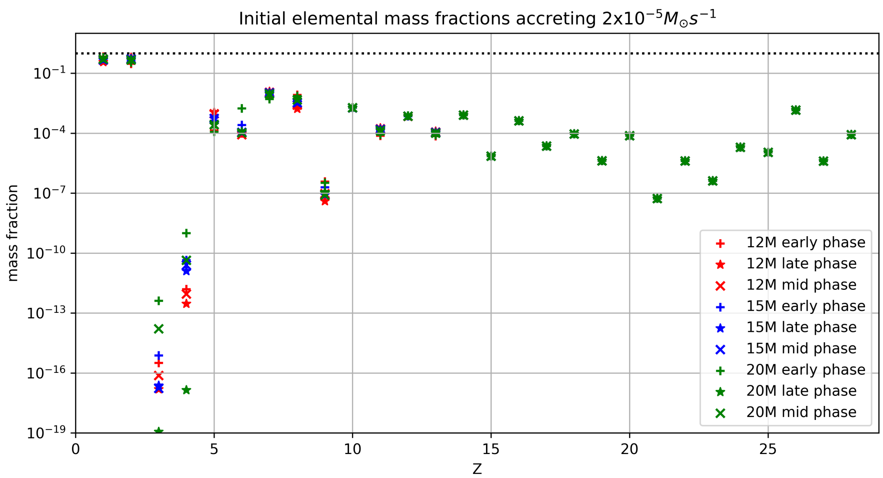

Figure 5.15: Initial elemental mass fractions for each environment for a common envelope accreting $2{\times}10^{-5}M_{\odot}s^{-1}$.

The initial elemental mass fractions used for the $2{\times}10^{-5}M_{\odot}s^{-1}$ accretion rate are shown in figure 5.15. To achieve this accretion rate the neutron star must be much closer to the companion core for each environment, figures 5.7, 5.8 and 5.9 show the accretion rate change as a function of radial distance for each companion mass and age. For each environment the neutron star must be approximately $0.5R_{\odot}$ closer to the companion core to achieve the $2{\times}10^{-5}M_{\odot}s^{-1}$ mass transfer. For the 15M$_{\odot}$ companion midway through the expansion phase this results in the neutron star entering the boundary between the hydrogen envelope and the helium envelope, accreting an almost even mixture of hydrogen and helium (H = 0.460 and He = 0.519). The main changes in all environments are in the fractions of CNO isotopes and the ratio of hydrogen to helium, which then impact the type of nucleosynthesis possible as a lower hydrogen mass fractions lead to less proton capture reactions.

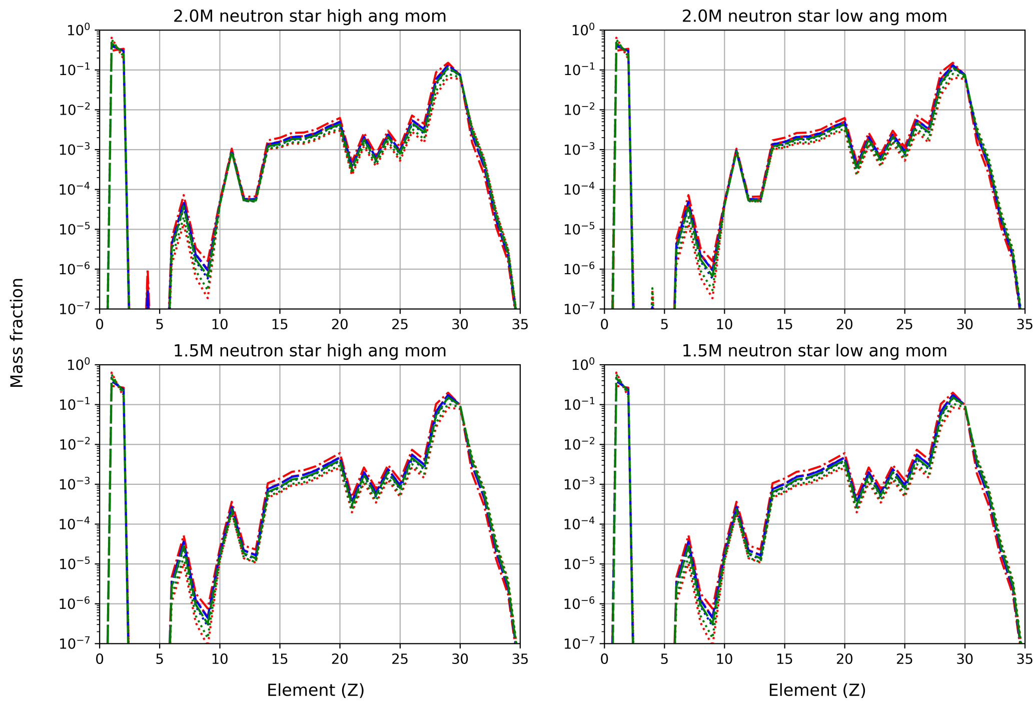

Figure 5.16: Elemental mass fraction distributions greater than $1{\times}10^{-7}$ for each neutron star mass and angular momentum. Dotted lines represent the early phase expansion, dashed lines represent mid phase expansion and dot-dashed lines represent late phase expansion. Companion masses of $12\mathrm{M}_{\odot}$ are shown in red, $15\mathrm{M}_{\odot}$ in blue and $20\mathrm{M}_{\odot}$ in green.

The resulting elemental mass fractions from each environment are very similar, as shown in figure 5.16. The distribution once again peaks around the iron group, but unlike the $1{\times}10^{-5} M_{\odot} s^{-1}$ accretion rate trajectory the mass fraction of CNO elements are not impacted by the neutron star mass. This is because the time spent above 0.1GK is the same for both neutron star masses. Figure 5.16 also shows that the late phase expansion for each companion mass produce higher mass fractions of CNO elements and elements between silicon and cobalt, and the elemental distributions produced by the mid expansion phase are the same for each companion mass. This is because the initial mass fractions for the mid-expansion phase environments are all very similar, with the smallest hydrogen mass fraction (for the $12\mathrm{M}_{\odot}$ companion) being 94% of the largest hydrogen mass fraction (for the $20\mathrm{M}_{\odot}$ companion). This figure also shows the correlation between beryllium mass fraction and time spent at high temperatures, as seen for the $1{\times}10^{-5}M_{\odot}s^{-1}$ accretion rate.

Figure 5.17 shows the strongest flux reactions to occur in each environment for a 2.0$M_{\odot}$ neutron star with $5 \times 10^{17}cm^2s^{-1}$ angular momentum. The main reaction channels used are proton captures, with very little variation as a result of companion mass or age. The early phases reach further into the proton rich region of the nuclear chart after nickel leading to the reduced mass fraction of elements leading up to the iron peak. In all environments it is clear that rapid proton capture drives nucleosynthesis as the successive proton captures are the dominant reaction. This is indicative of the rp-process. This is supported by the production of proton rich isotopes, such as ^{44}Ti and ^{56}Ni, in each environment, however the full rp-process is not achieved as the mass fractions of isotopes in the tin-tellurium region are unaffected. It is likely due to the lack of heavy isotopes of seed nuclei and the short period of time at the peak of the trajectory. The trajectory also shows α capture reactions on ^{22}Mg and ^{30}S. However, compared to 1.3 they are at a much lower flux, this is due to the very short time spent above 1GK in each trajectory.

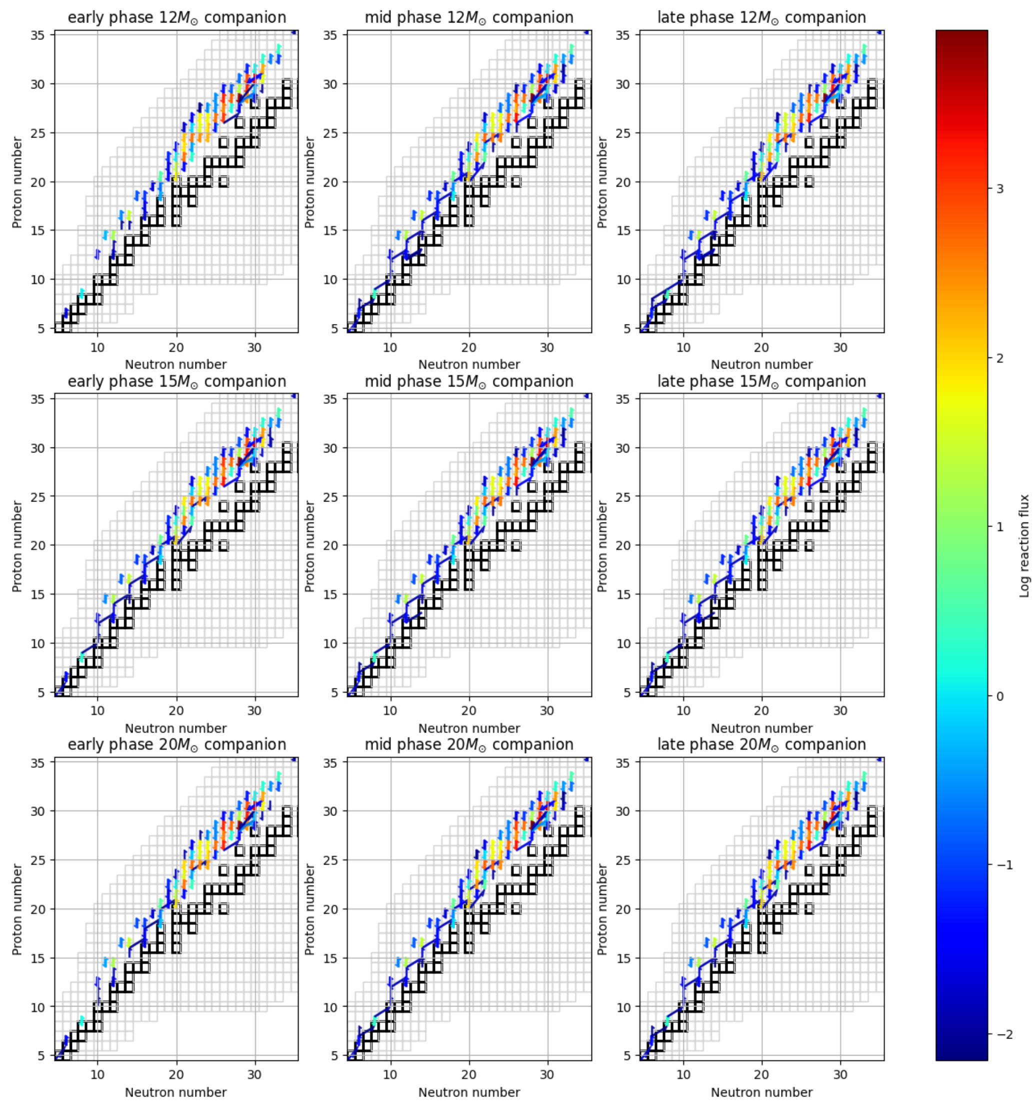

Figure 5.17: Final integrated flux ($\Sigma\frac{dY}{dt}$) for a $2M_\odot$ neutron star with $5 \times 10^{17} cm^2 s^{-1}$ for each companion mass and phase after expansion. The integrated flux shows the total amount of material that has flowed through that reaction channel over the course of the trajectory.

5.3.3 $4{\times}10^{-5}M_{\odot}s^{-1}$ accretion rate

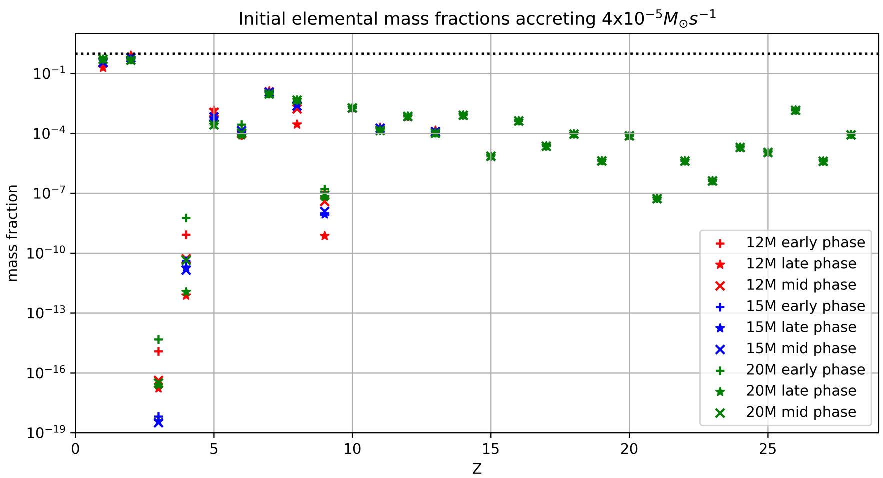

Figure 5.18: Initial elemental mass fractions for each environment for a common envelope accreting $4{\times}10^{-5}M_{\odot}s^{-1}$.

The initial mass fractions for the $4{\times}10^{-5}M_{\odot}s^{-1}$ accretion rate trajectory are shown in figure 5.18. This is again similar to the previous two elemental distributions, but the late phases contain more helium than hydrogen and the early and medium phases have almost equal fractions of hydrogen and helium. As with the previous two accretion rates, the mass fractions for elements above neon do not change across the different environments. Figure 5.19 shows the final elemental abundances for the $4{\times}10^{-5}M_{\odot}s^{-1}$ accretion rate. At this accretion rate the 12M$_{\odot}$ companion during the late expansion phase leads to higher fractions of elements between nitrogen and nickel, while also under producing elements between zinc and ruthenium. The 1.5M$_{\odot}$ neutron star trajectory in the same companion mass and age produces a very similar distribution to the 2.0M$_{\odot}$ trajectory but with a higher mass fraction of carbon. This is due to the longer time spent orbiting the neutron star at the edge of the accretion disk, at 0.11Gk, in which the triple α reaction produces ^{12}C. The distributions produced by the other environments (15M$_{\odot}$ and 20M$_{\odot}$ all phases and early and mid phase for 12M$_{\odot}$) all produce distributions similar to the previous two accretion rates, producing proton rich material predominantly via proton capture reactions but also through α capture reactions.

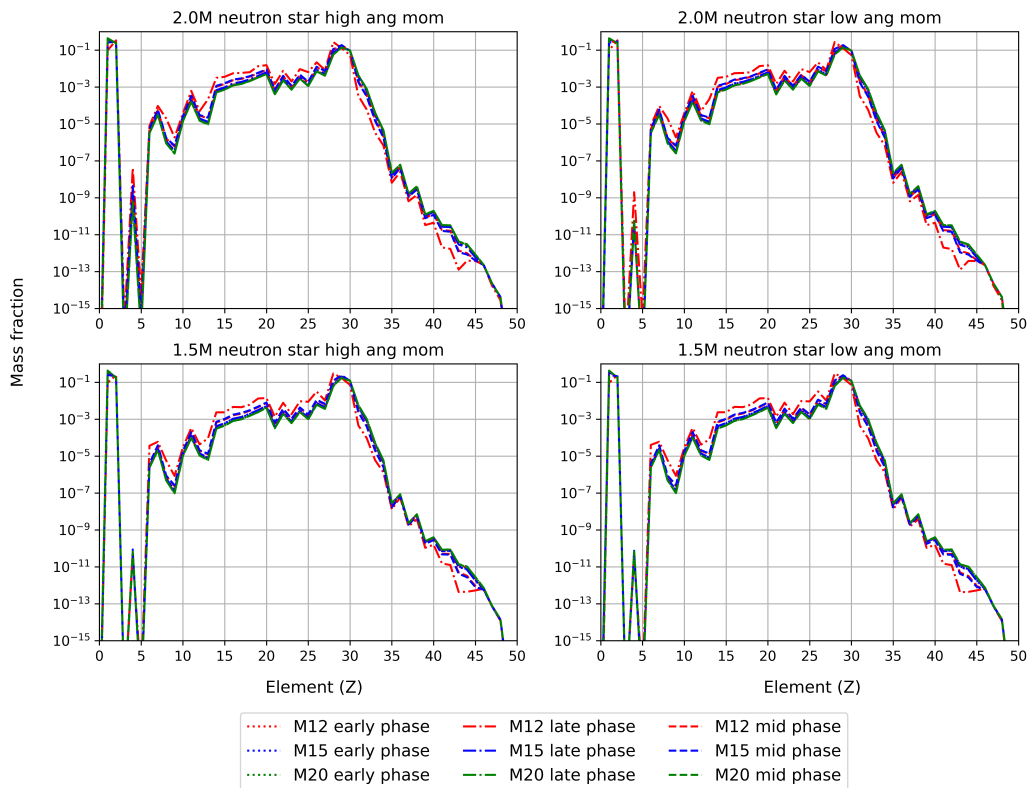

Figure 5.19: Elemental mass fraction distributions greater than $4\times10^{-5} M_{\odot} s^{-1}$ for each neutron star mass and angular momentum. Dotted lines represent the early phase expansion, dashed lines represent mid phase expansion and dot-dashed lines represent late phase expansion. Companion masses of $12M_{\odot}$ are shown in red, $15M_{\odot}$ in blue and $20M_{\odot}$ in green.

Figure 5.20 shows the final reaction flux for a $2M_{\odot}$ neutron star inside the three different mass companions during the late phase expansion. It is clear that the composition of the material accreted from the $12M_{\odot}$ companion causes the difference in the final elemental mass fractions as the high fraction of helium leads to more α capture reactions close to the valley of stability compared to the $15M_{\odot}$ and $20M_{\odot}$ companions. In all environments the (p,γ) reaction channels are the strongest and the α capture reactions onto ^{22}Mg and ^{30}S do occur but at a much lower flux. The differences seen

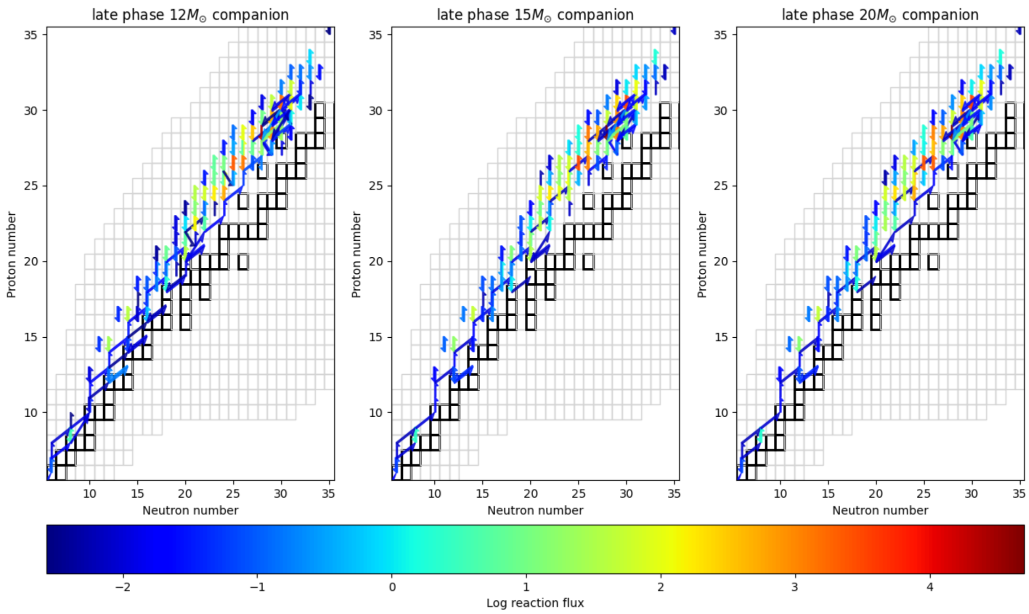

Figure 5.20: Final integrated reaction fluxes $(\Sigma \frac{dY}{dt})$ for each companion mass in the late phase of expansion.

in the reaction flux when compared to 1.3 are due to the different composition of the material. The common envelope environments all have a higher initial fraction of helium compared to the study conducted in [60]. These trajectories also spend a much shorter time at extreme temperatures (grater than 1GK) when compared to the study conducted in [60]. However, the reaction pathways seen in the common envelope accretion disks are the same as those seen in 1.3 and so the rp-process does occur at this accretion rate.

5.3.4 $8\times10^{-5}M_{\odot}s^{-1}$ accretion rate

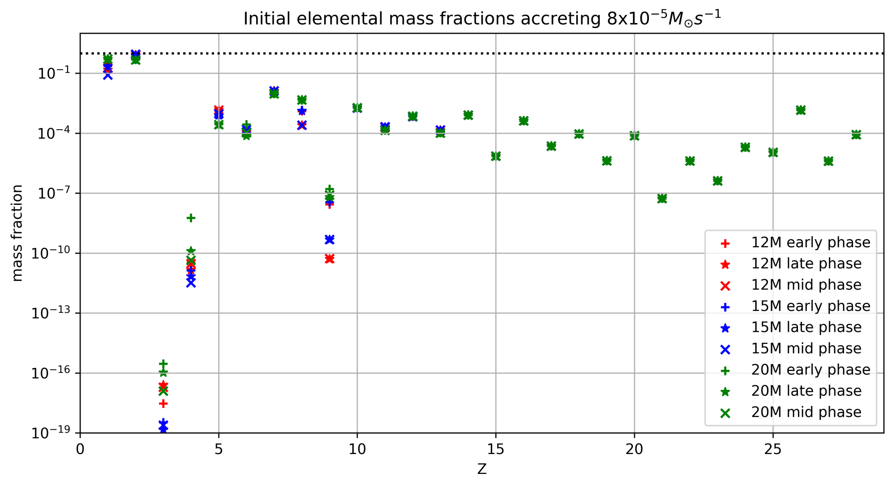

Figure 5.21: Initial elemental mass fractions for each environment for a common envelope accreting $8\times10^{-5}M_{\odot}s^{-1}$.

The initial mass fractions for the $8\times10^{-5}M_{\odot}s^{-1}$ accretion rate, displayed in figure 5.21, reveal a continued decrease in the hydrogen mass fraction as the accretion rates increase. This trend is observed for a neutron star located closer to the centre of the companion, compared to the previous accretion rate. Figures 5.7 and 5.8 shows that, for 12 and 15M$_{\odot}$ companion masses, the mid and late phase expansion environments see the neutron star accreting material from the helium envelope. This suggests that the main reaction mechanism that will occur for this accretion rate will be α captures, not proton capture reactions as seen in the previous accretion rates.

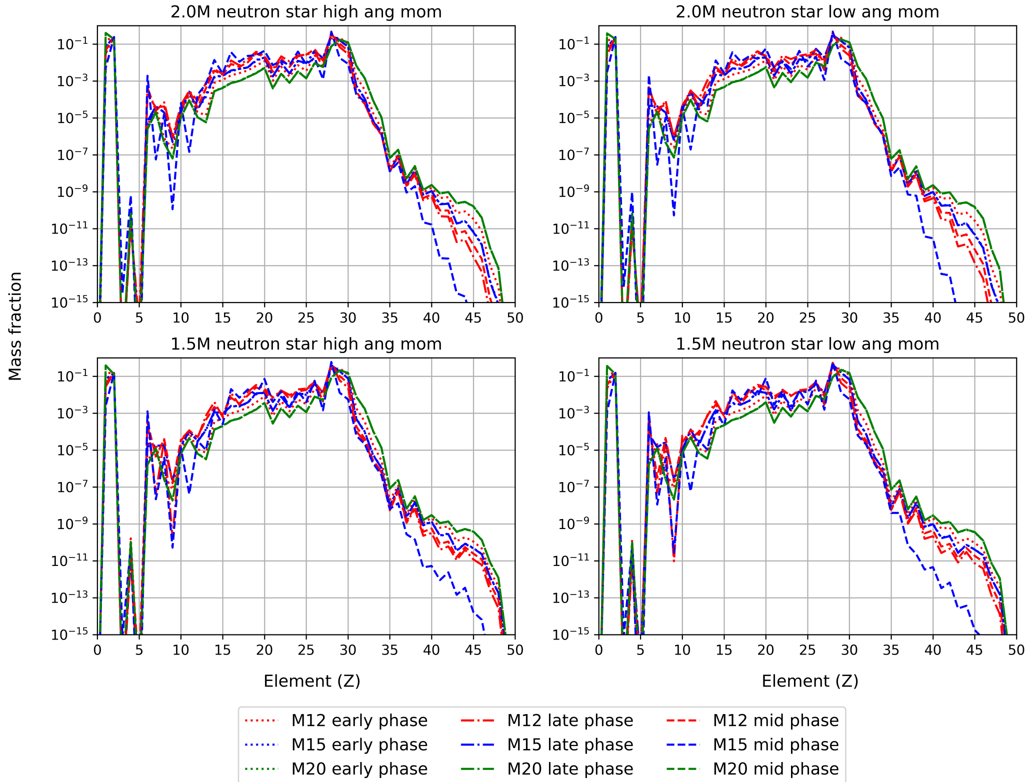

Figure 5.22: Elemental mass fraction distributions greater than $8{\times}10^{-5}M_{\odot}s^{-1}$ for each neutron star mass and angular momentum. Dotted lines represent the early phase expansion, dashed lines represent mid phase expansion and dot-dashed lines represent late phase expansion. Companion masses of 12M$_{\odot}$ are shown in red, 15M$_{\odot}$ in blue and 20M$_{\odot}$ in green.

Figure 5.22 shows the resulting elemental mass distribution for each environment and there are significant differences depending on the companion mass and age after companion expansion. The 20M$_{\odot}$ companion produces the same elemental distribution regardless of age, which is the same distribution up to nickel as the previous three accretion rates. However, it now produces much higher fractions of elements above zirconium as a result of the higher temperatures being reached and the relatively higher mass fraction of hydrogen when compared to the 12 and 15M$_{\odot}$ companions. For the 15M$_{\odot}$ companion, both the early and mid phase environments provide the same mass fraction distribution as both of these environments have the same initial mass fraction distribution, as seen in figures 5.21 and 5.8. For these phases in the $15M_{\odot}$ companion the material partially enters NSE, as shown by the sharp peak at nickel, but contributions from larger inner radii (with lower peak temperatures) are not in NSE resulting in some material beyond nickel being produced. As the material falls towards the neutron star the contributions from inner radii close to the neutron star provide NSE elemental distributions, but the contributions from inner radii further away do not reach NSE and so provide elemental mass fractions for isotopes beyond the iron peak that would not normally be seen if the whole trajectory had entered NSE. This is seen more in the $15M_{\odot}$ companion environment than in the $12M_{\odot}$ companion. As α captures are closer to stability a small amount of material to continues to fuse beyond nickel along stability, resulting in a higher fraction of bromine to cadmium when compared to lower accretion rates. Figure 5.23 shows the final integrated flux for a $2M_{\odot}$ neutron star with angular momentum of $5 \times 10^{17} cm^2 s^{-1}$ in each companion environment. This clearly shows the change in nucleosynthesis for the mid phase $15M_{\odot}$ companion. This environment has the lowest initial hydrogen mass fraction and so results in significantly more α capture, this is due to the position of the neutron star inside the common envelope that is needed to achieve this accretion rate (as seen in figure 5.8). This figure also highlights the lack of α capture reaction in the $20M_{\odot}$ environment. The α capture reactions that do occur are around the nickel peak, whereas in both the 12 and $15M_{\odot}$ environments there are α capture reactions occurring between low mass stable nuclei. This traps material in the lower mass region leading to lower production of elements above nickel.

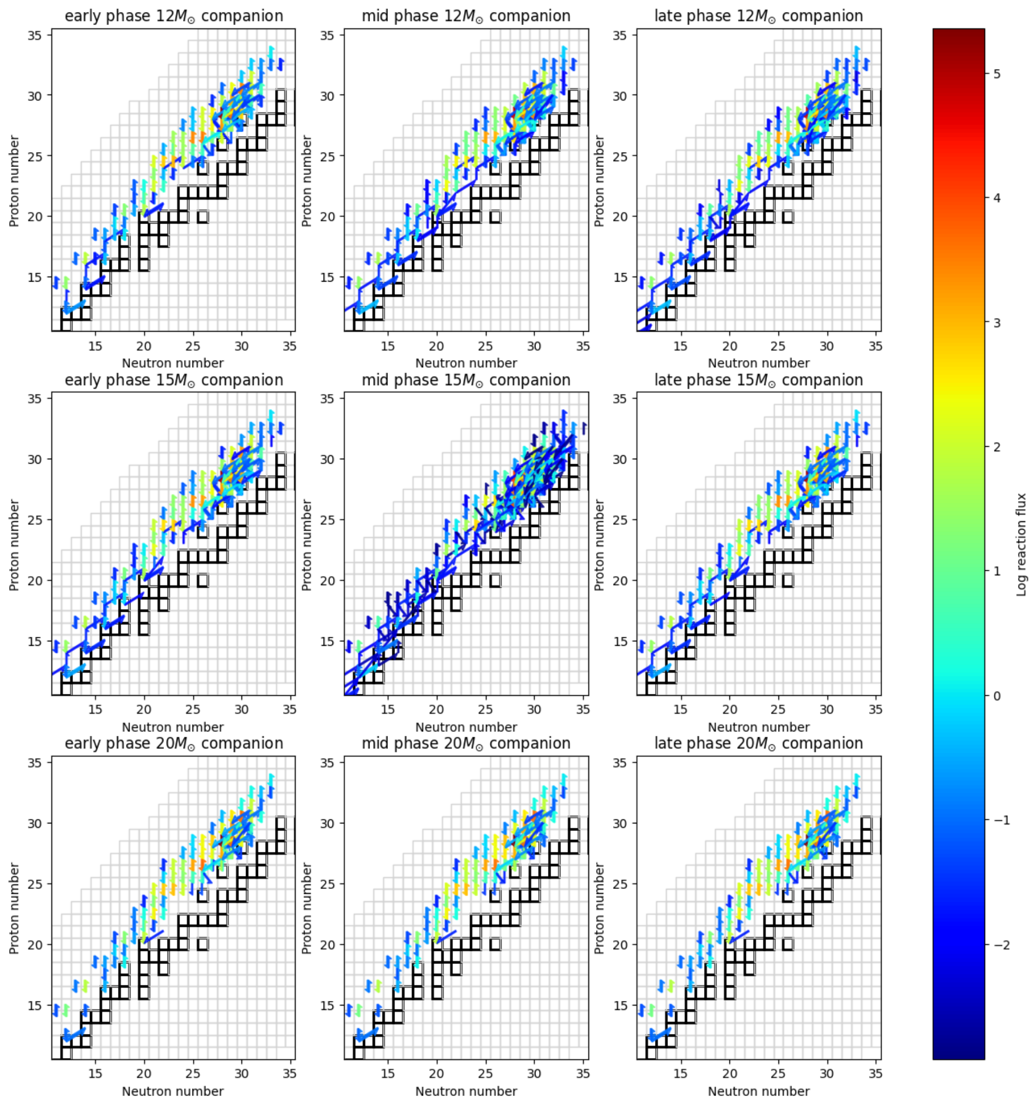

Figure 5.23: Integrated flux $(\Sigma \frac{dY}{dt})$ for a $2M_{\odot}$ neutron star with angular momentum of $5 \times 10^{17} cm^2 s^{-1}$ for each companion mass and phase after companion expansion.

5.3.5 $16\times10^{-5}M_{\odot}s^{-1}$ accretion rate

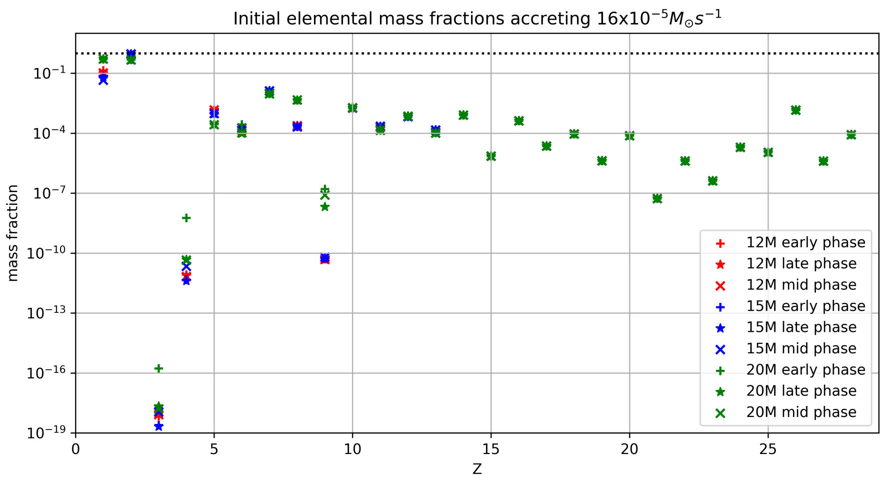

Figure 5.24: Initial elemental mass fractions for each environment for a common envelope accreting 16×10^{-5} M$_{\odot}s^{-1}$. Elements above

The initial mass fractions for the 16×10^{-5} M$_{\odot}s^{-1}$ accretion rate are very similar to the previous 8×10^{-5} M$_{\odot}s^{-1}$ for 12 and 15M$_{\odot}$ companions. From figures 5.7 and 5.8 it is clear that this is due to the sharp increase in the accretion rate relative to the decrease in hydrogen mass fraction. This increase is due to the 8-32$\times10^{-5}$ M$_{\odot}s^{-1}$ accretion rates occurring near the boundary between the hydrogen and helium layers in the 12 and 15M$_{\odot}$ companions. The 20M$_{\odot}$ companion still has an almost equal amount of hydrogen and helium at this accretion rate as the density in this environment is much higher at the bottom of the hydrogen envelope.

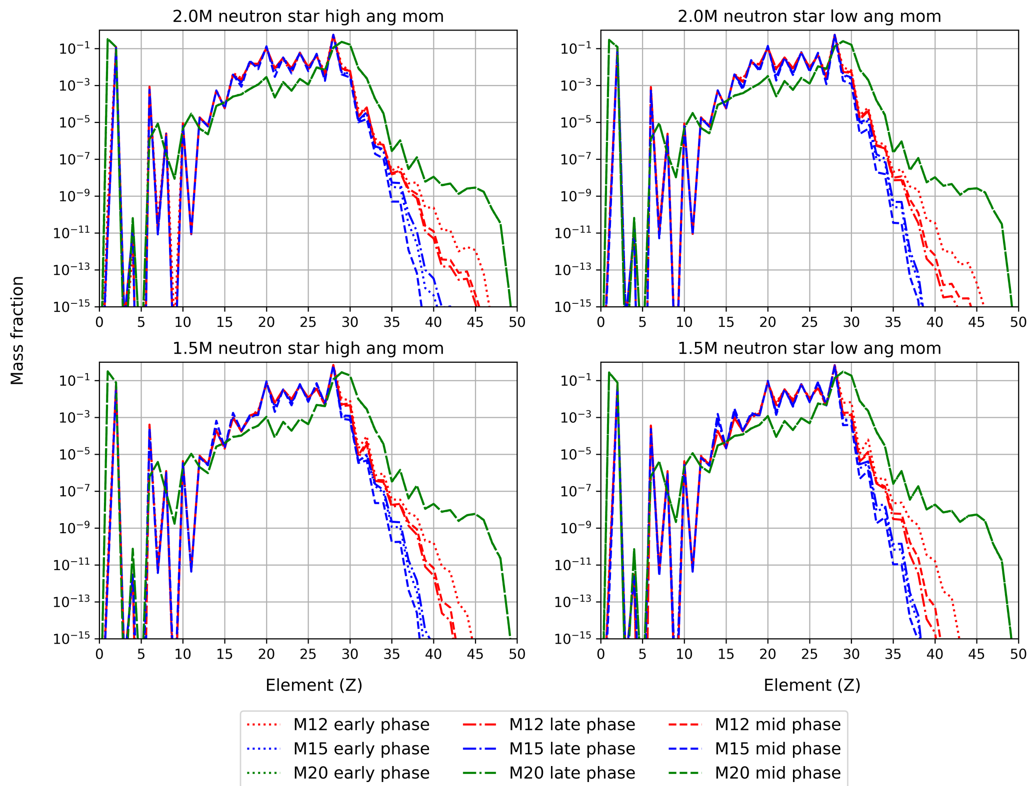

Figure 5.25: Elemental mass fraction distributions greater than $16{\times}10^{-5}M_{\odot}s^{-1}$ for each neutron star mass and angular momentum. Dotted lines represent the early phase expansion, dashed lines represent mid phase expansion and dot-dashed lines represent late phase expansion. Companion masses of 12M$_{\odot}$ are shown in red, 15M$_{\odot}$ in blue and 20M$_{\odot}$ in green.

At this accretion rate the final elemental mass fractions for the 12 and 15M$_{\odot}$ companions show evidence of NSE nucleosynthesis. This is clear from the sharp peak at nickel, followed by the low production of elements beyond the iron peak. In both of these environments, helium has the highest initial mass fraction and so successive α capture reactions are dominant, resulting in material close to the valley of stability being produced. Proton capture reactions do occur but due to the much lower initial hydrogen mass fraction they are much less frequent and are also competing with α capture reactions as a result of the high helium mass fraction. Leading up to the peak temperature these environments produce small fractions of elements heavier than nickel, but much less compared to the 20M$_\odot$ as alpha capture reactions in this mass region have much smaller cross-sections when compared to the proton capture reactions seen in the 20M$_\odot$.

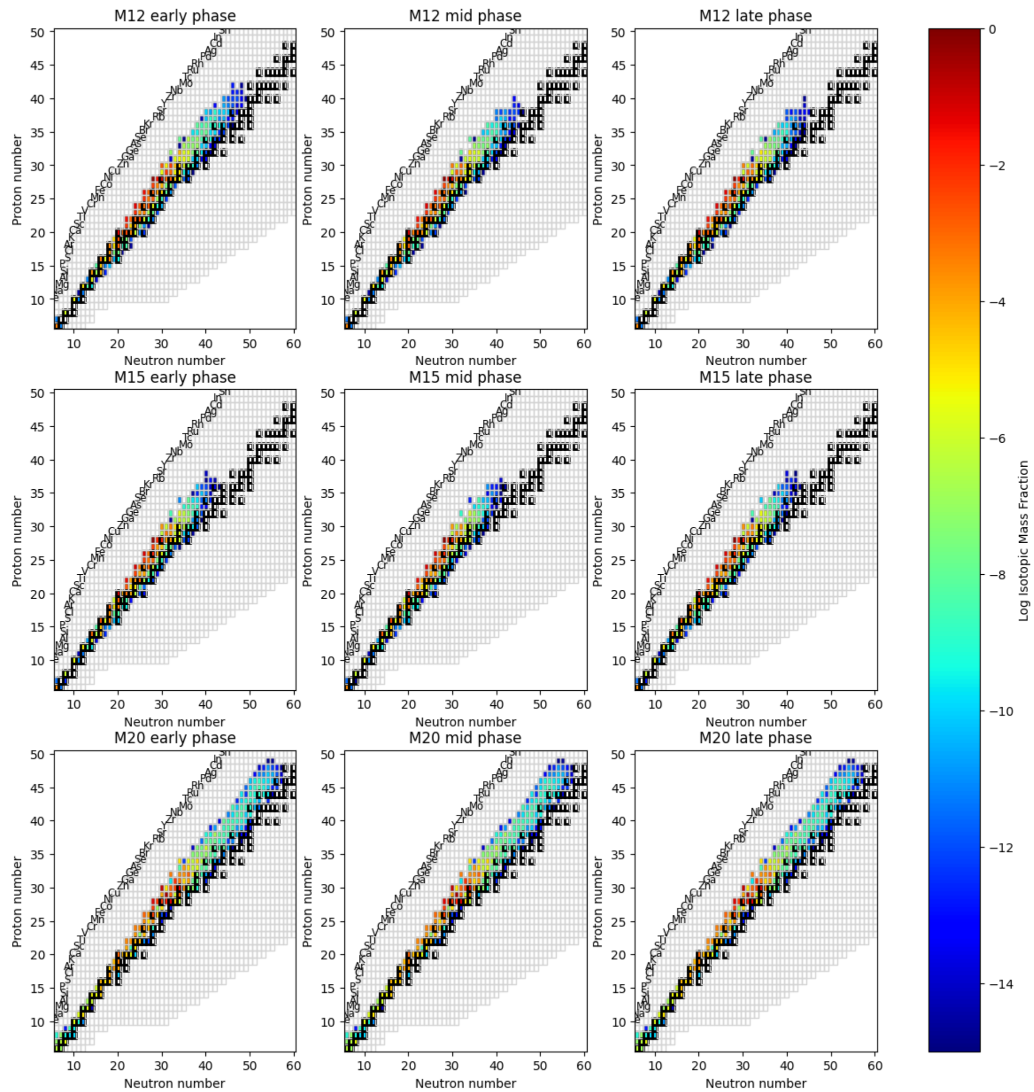

Figure 5.26: Final isotopic mass fraction distribution for a 1.5M$_\odot$ neutron star with angular momentum of $5 \times 10^{16} cm^2 s^{-1}$ for each companion environment.

Like in the previous accretion rate the 20M$_\odot$ companion environment produces lower mass fractions of elements between neon and nickel as proton capture reactions are still dominant. As these have a lower energy threshold than α captures more material in the 20M$_\odot$ environment is pushed beyond nickel compared to the 12 and 15M$_\odot$ environments. Figure 5.26 shows the final isotopic mass fraction distribution for each companion environment, and it is clear that the higher hydrogen mass fraction in the 20M$_\odot$ environment leads to synthesis of isotopes beyond nickel due to the large cross-sections for proton capture reactions compared to the smaller cross-sections for alpha capture reactions. The variation in the initial composition results in different distribution of isotopic mass fractions and is more impactful than each environment entering NSE. This is because each environment is only in NSE for a short time, approximately 5 seconds, and so full equilibrium is not reached.

5.3.6 32$\times 10^{-5} M_\odot s^{-1}$ accretion rate

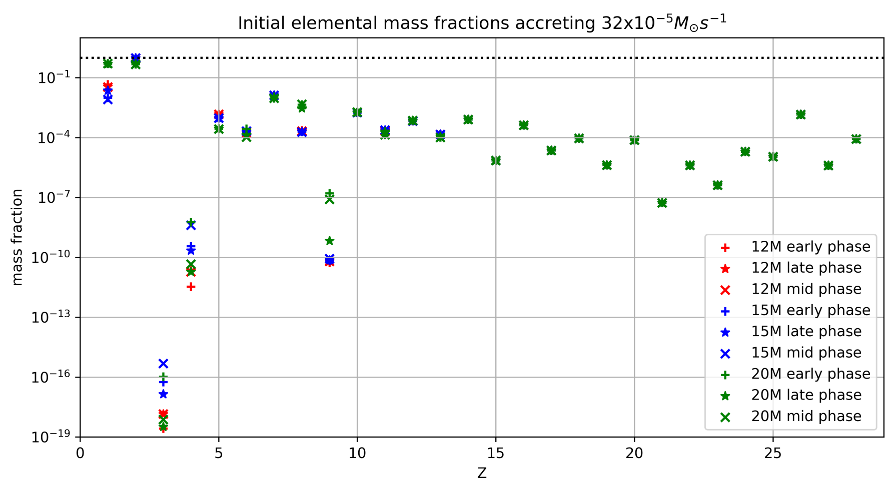

Figure 5.27: Initial elemental mass fractions for each environment for a common envelope accreting 32×10^{-5} M$_\odot s^{-1}$.

The initial mass fractions for the 32×10^{-5} M$_\odot s^{-1}$ accretion rate, shown in figure 5.27 in a 20M$_\odot$ companion environment are very similar to the previous accretion rate, however both the 12 and 15M$_\odot$ environments have a smaller initial fraction of hydrogen than in the previous accretion rates.

The 12M$_\odot$ companion has nearly identical initial mass fractions in at each phase after expansion. As the initial mass fractions are similar to the previous environment, but the peak temperatures reached are much higher than the previous accretion rate this will likely lead to similar reaction channels being used but lead to NSE in more environments.

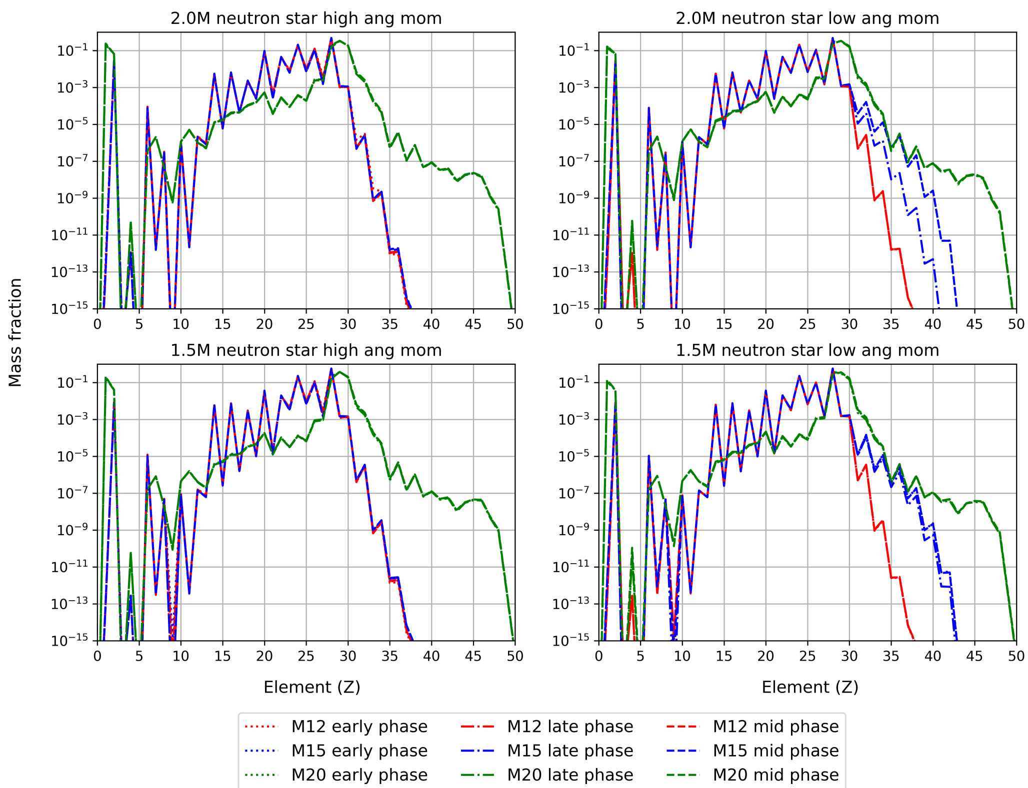

Figure 5.28: Elemental mass fraction distributions greater than $32{\times}10^{-5}M_\odot s^{-1}$ for each neutron star mass and angular momentum. Dotted lines represent the early phase expansion, dashed lines represent mid phase expansion and dot-dashed lines represent late phase expansion. Companion masses of 12M$_\odot$ are shown in red, 15M$_\odot$ in blue and 20M$_\odot$ in green.

The final elemental mass fractions for each environment accreting $32{\times}10^{-5}$ M$_\odot s^{-1}$ are shown in figure 5.28. For a 12M$_\odot$ companion there is almost no difference in elemental mass fraction as a result of age, angular momentum and neutron star mass. The only difference is for a 2M$_\odot$ neutron star with an angular momentum of $5 \times 10^{17} cm^2 s^{-1}$ during the early expansion phase of a 12M$_\odot$ companion, which results in slightly higher fractions of gallium and arsenic. This is due to the short period of time spent in the peak temperature region compared to the other neutron star masses and angular momenta for the same environment and even though it is dominated by NSE the short period of time spent at this temperature means equilibrium is not fully achieved.

For both neutron star masses inside a 15M$_\odot$ companion, varying the angular momentum of the material in the accretion disk generates different mass fractions for elements above zinc. From this it is clear that the time spent in the accretion disk before falling towards the neutron star plays a significant role in the production of elements beyond the iron peak. Further investigation into the reaction flux reveals that NSE dominates during the peak temperatures, but leading up to the peak temperature fusion is not just restricted to the proton rich side of the valley of stability. This is because the high helium mass fraction leads to (α, n) reactions that produce neutrons, which are then captured onto seed nuclei. This process occurs in the accretion disk before reaching the maximum temperature and as the low angular momentum trajectories spend much more time in the disk this leads to the higher fraction of elements above nickel.

Figure 5.29 shows the integrated flux for 1.5M$_\odot$ neutron star with angular momentum of $5 \times 10^{16} cm^2 s^{-1}$ at the point where the temperature reaches 0.5GK during the evolution of the trajectory. From this it is clear that in each environment the dominant reaction channels in the lead up to 0.5GK change as a result of the initial mass fractions of hydrogen and helium.

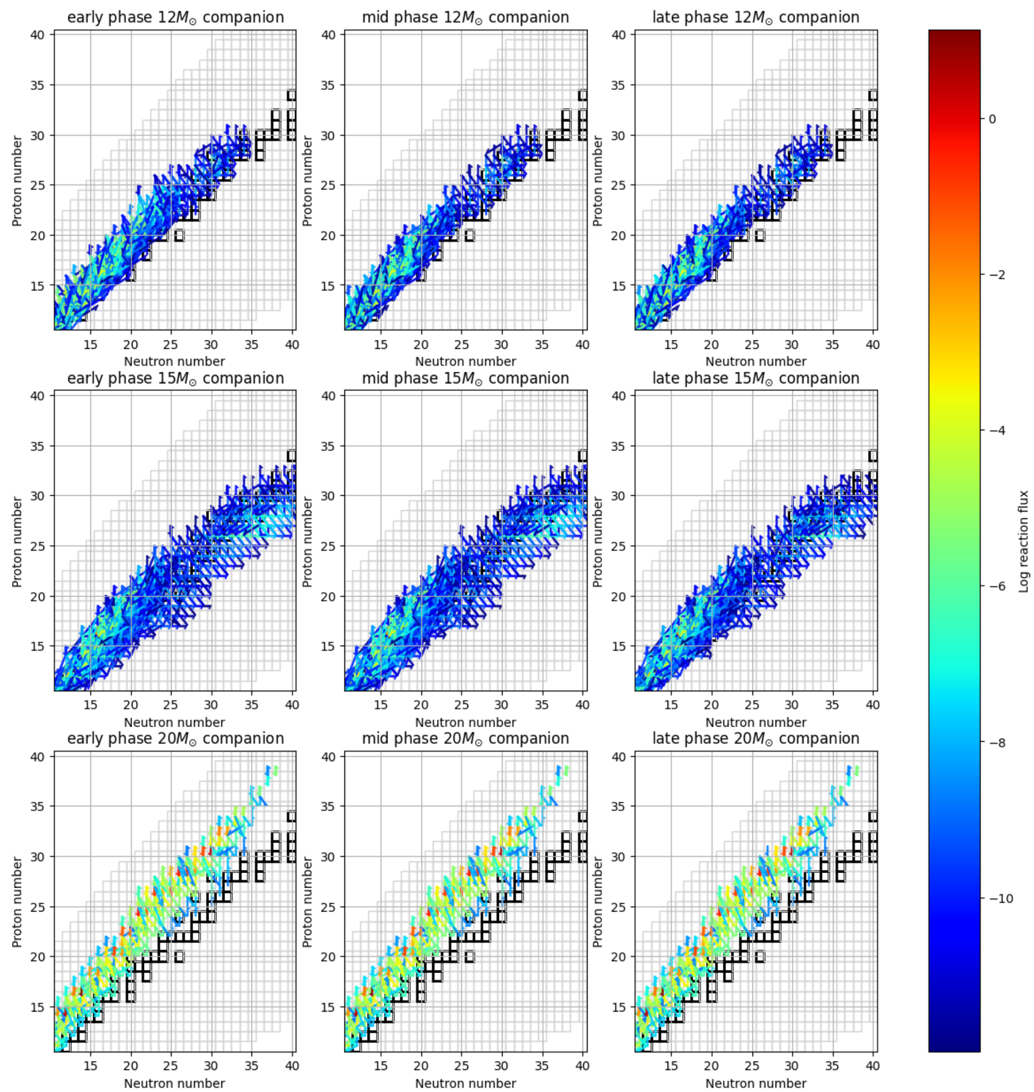

Figure 5.29: Integrated flux $(\Sigma \frac{dY}{dt})$ for 2.0M$_\odot$ neutron star with angular momentum of $5 \times 10^{16} cm^2 s^{-1}$ at 0.5GK in each companion environment and age.

The type of nucleosynthesis seen in each environment is mostly the same when looking at the different phases beyond expansion, for example in the 20M$_\odot$ environment it is clear that proton capture reactions drive nucleosynthesis in the accretion disk at every age beyond expansion. When comparing the same expansion phases across different mass companions the main reaction channels used are different depending on the mass. A neutron star inside a 12M$_\odot$ companions envelope undergoes alpha, proton and neutron capture reactions, with the most nucleosynthesis occurring within the proton rich region between silicon and calcium. However, the same trajectory inside the 15M$_\odot$ environments have a high flux of neutron capture reactions along N=26. This indicates that a higher fraction of neutrons are produced in the 15M$_\odot$ environments when compared to the 12 and 20M$_\odot$ environments and leads to a higher production of elements between zinc and technicum when compared to the 12M$_\odot$. Further investigation reveals that the $^{25}Mg(\alpha,n)^{28}Si$ reaction produces a high fraction of neutrons in the 15M$_\odot$ environment. The 20M$_\odot$ environment also highlights the impact of a high hydrogen mass fraction in the initial composition as this has much higher reaction fluxes across the reaction channels as capturing protons required less energy when compared to capturing α particles.

5.3.7 $64\times10^{-5}M_\odot s^{-1}$ accretion rate

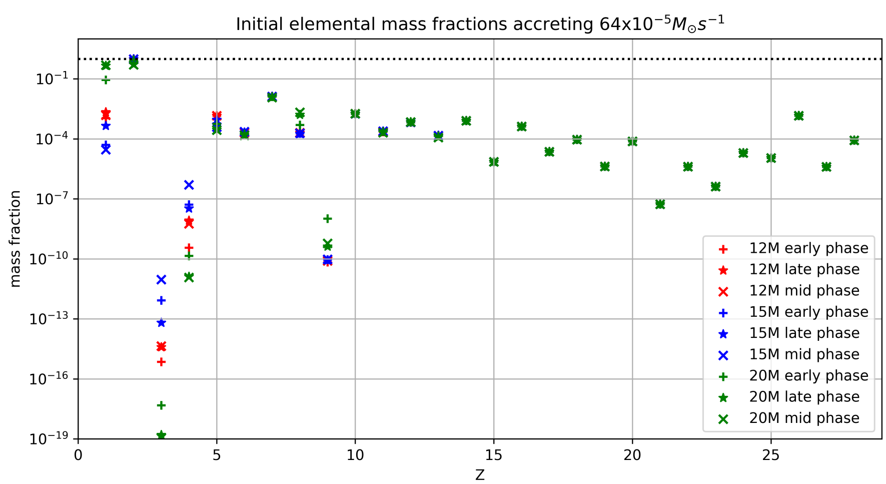

Figure 5.30: Initial elemental mass fractions for each environment for a common envelope accreting 64×10^{-5} M$_\odot s^{-1}$.

The initial mass fractions for the $64{\times}10^{-5}$ M$_\odot s^{-1}$ accretion rate trajectory are shown in figure 5.30. The 12 and 15M$_\odot$ environments both continue to reduce the amount of hydrogen available but also experience an increase of lithium and beryllium as the point of accretion moves further into the companion envelope helium shell, this is due to helium particles fusing with hydrogen and other helium particles to produce lithium and beryllium in the helium envelope. The 20M$_\odot$ early phase is also accreting material from the hydrogen/helium boundary, resulting in a higher fraction of lithium and beryllium when compared to the other 20M$_\odot$ initial mass fractions.

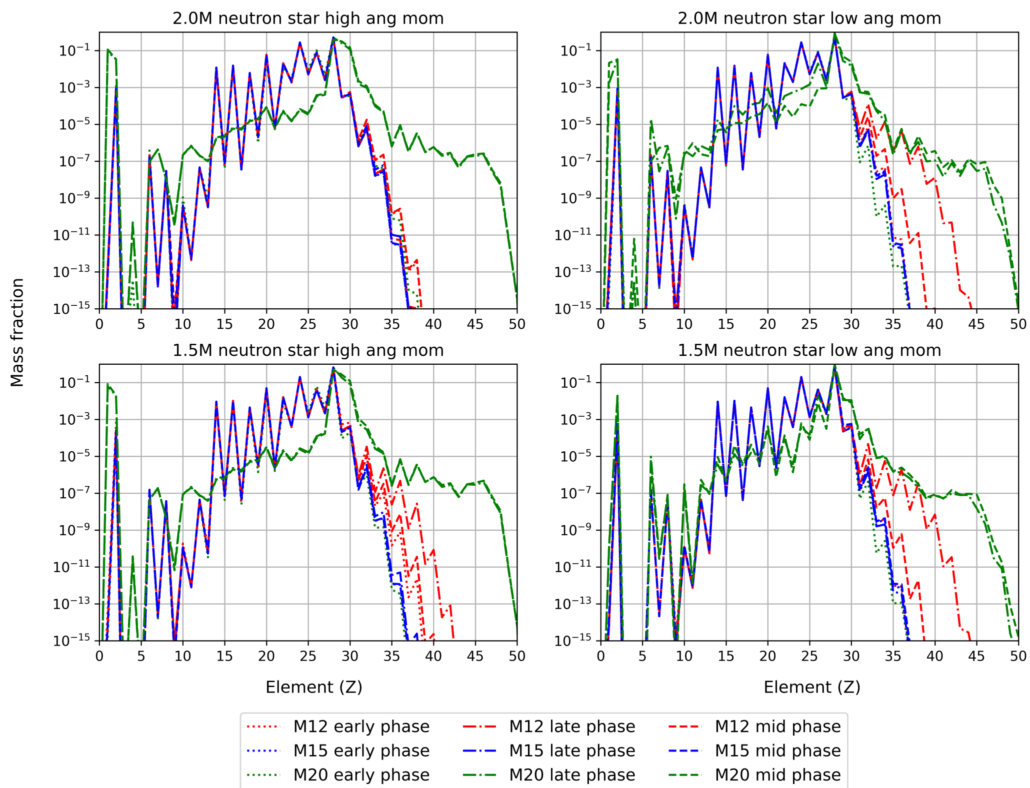

Figure 5.31: Elemental mass fraction distributions greater than $64{\times}10^{-5}M_\odot s^{-1}$ for each neutron star mass and angular momentum. Dotted lines represent the early phase expansion, dashed lines represent mid phase expansion and dot-dashed lines represent late phase expansion. Companion masses of 12M$_\odot$ are shown in red, 15M$_\odot$ in blue and 20M$_\odot$ in green.

Figure 5.31 shows the final elemental mass fractions for the $64{\times}10^{-5}$ $\mathrm{M}_{\odot}s^{-1}$ accretion rate trajectory. This is the first accretion rate at which every environment reaches NSE. The early, mid and late stage expansions for the 12 and 15$\mathrm{M}_{\odot}$ companions provide the same elemental mass fraction up to nickel as in the previous environments (except for beryllium as this is destroyed via alpha capture reactions). But the 20$\mathrm{M}_{\odot}$ environments provide very different results. All the 20$\mathrm{M}_{\odot}$ companion environments enter NSE for every neutron star trajectory, as shown by the high fraction of nickel. However, the early expansion phase for the 20$\mathrm{M}_{\odot}$ companion results in α capture reactions along stability, like that seen in the 12 and 15$\mathrm{M}_{\odot}$ environments for the previous two accretion rates, and produce low fractions of elements heavier than nickel due to the low initial fraction of hydrogen. However, the mid and late stage environments result in rapid proton capture in the lead up to the peak temperature, as seen in figure 5.32, at which point it enters NSE, shown in figure 5.34

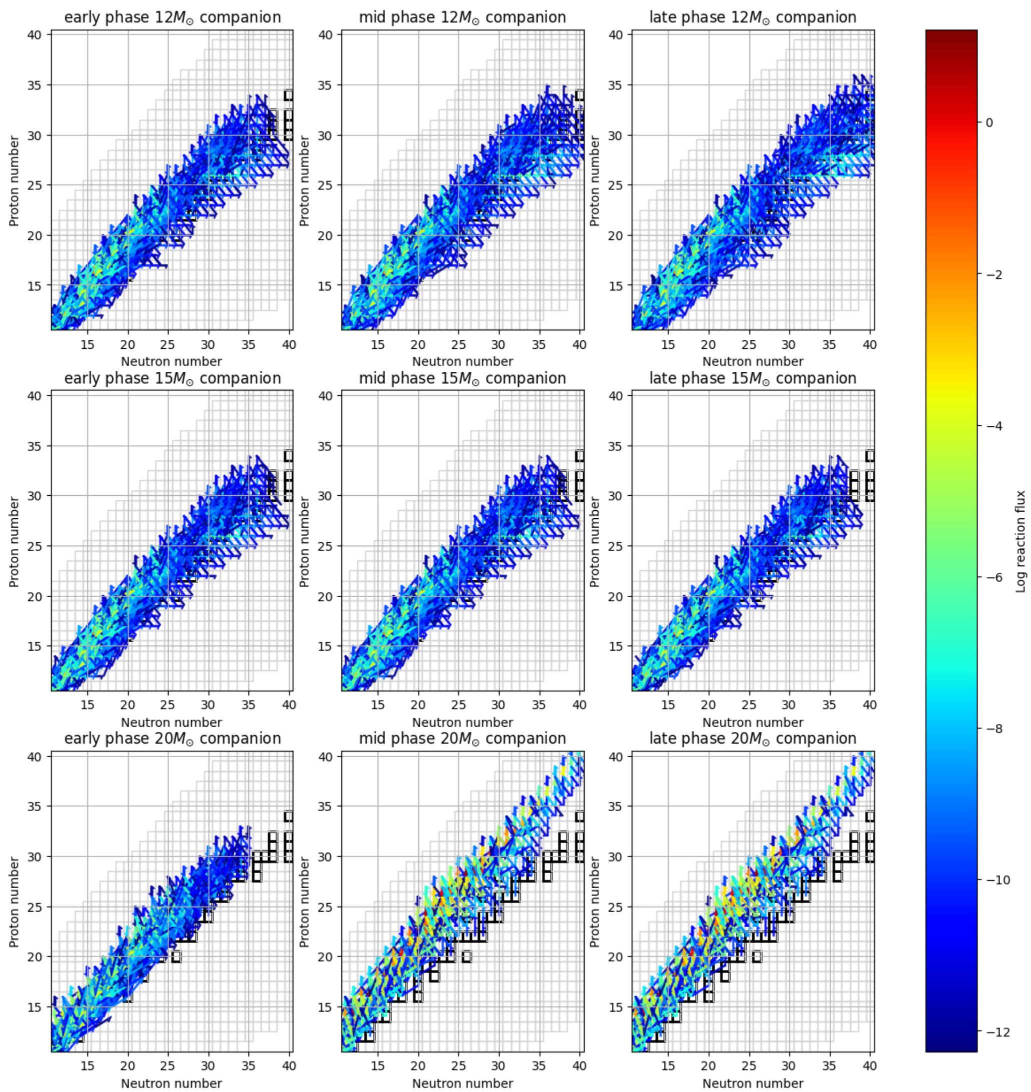

Figure 5.32: Integrated reaction fluxes ($\Sigma\frac{dY}{dt}$) up to 1GK from the $64{\times}10^{-5}$ $\mathrm{M}_{\odot}s^{-1}$ accretion rate trajectory with angular momentum of $5 \times 10^{16} cm^2 s^{-1}$ in each companion environment.

Figure 5.32 also highlights the different nucleosynthetic pathways used as material is accreted from the helium envelope. For a 20$\mathrm{M}_{\odot}$ companion this is the first accretion rate that has an initial hydrogen mass fraction below 0.1. This occurs during the early expansion phase and produces the same mass fraction distribution, for elements up to nickel, that is seen in both the 12 and 15M$_\odot$ environments. However when looking at the reaction fluxes it is clear that there are far fewer neutron capture reactions occurring in the early expansion of a 20M$_\odot$. The highest flux value for a neutron capture reaction in the lead up to 1GK occurs during in the envelope of a 15M$_\odot$ companion in the mid phase after expansion. Leading up to 1GK, this environment produces 3$\times$ as many (n,p) reactions when compared with a 12M$_\odot$ environment at the same expansion phase, and 4719$\times$ as many (n,p) reactions as a 20M$_\odot$ at the same phase. These neutron capture reactions are only possible if neutrons are available and as neutrons are not included in the initial mass fraction they must be produced during the evolution of the trajectory. The main production sight for neutrons, leading up to 1GK, is via the ^{22}Ne(α,n)^{25}Mg and ^{25}Mg(α,n)^{28}Si reactions and occurs due to the high initial helium mass fraction.

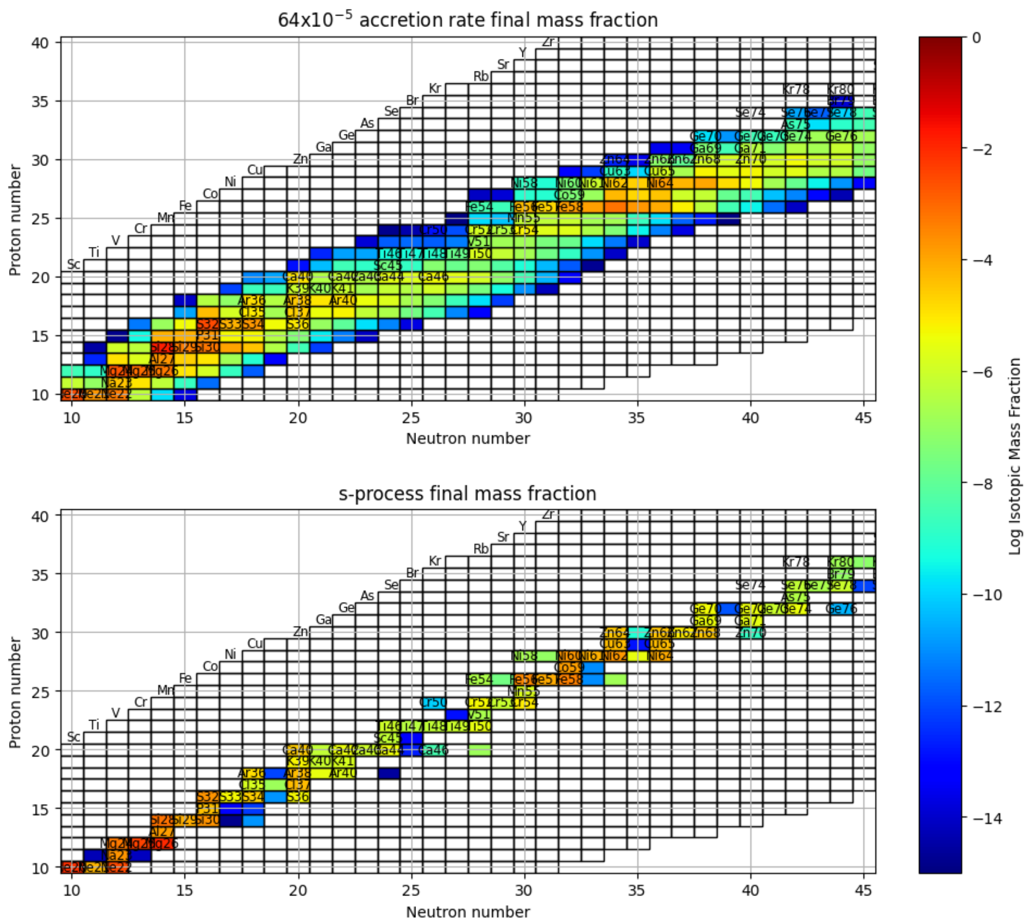

Figure 5.33: Final isotopic mass fractions for a common envelope accretion disk around a $2M_{\odot}$ neutron star in a $15M_{\odot}$ companion envelope during the mid expansion phase (Top) and for an s-process trajectory (bottom).

Figure 5.33 shows a comparison between the common envelope isotopic distribution for an accretion disk around a $2M_{\odot}$ neutron star in a $15M_{\odot}$ companion envelope during the mid phase of expansion and an s-process trajectory isotopic mass fraction distribution. While the trajectories have a very different temperature and density evolution, neutron capture reactions occur in both environments. The isotopic distribution produced by the common envelope follows the valley of stability but not as closely as the s-process due to the much higher temperature inside the common envelope. The higher temperatures allow successive neutron captures to occur before decaying back towards stability. This does not occur in the s-process as the lower temperature results in β^+ decay before another neutron capture reaction. The distribution of iron group isotopes also differs, with the s-process producing stable isotopes of iron, cobalt and nickel. The common envelope produces neutron rich isotopes of these elements, that would decay to stable iron group elements if allowed to cool from this point, however these are then destroyed during the peak temperature via (n,p) and (n,α) reactions.

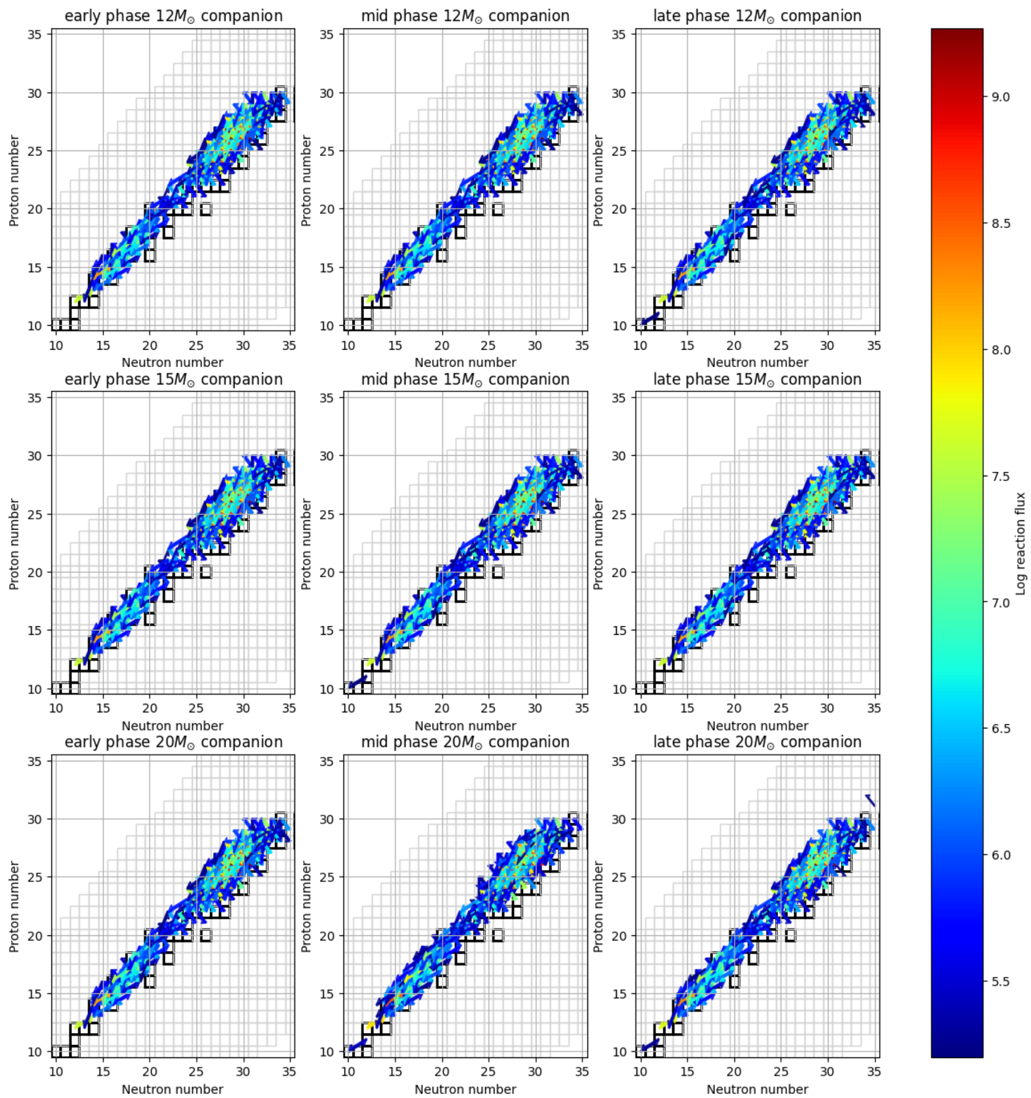

Figure 5.34: Final integrated reaction fluxes ($\Sigma\frac{dY}{dt}$) from the $64{\times}10^{-5}$ $M_{\odot}s^{-1}$ accretion rate trajectory in each companion environment.

The final integrated flux for the $64{\times}10^{-5}$ $M_{\odot}s^{-1}$ accretion rate are shown in figure 5.34. This shows reaction with flux within four orders of magnitude of the most powerful reaction, and it is clear that even in environments where neutron captures occur leading up to the peak temperature the dominant reaction pathways are on the proton rich side of stability.

5.3.8 $128\times10^{-5}M_{\odot}s^{-1}$ accretion rate

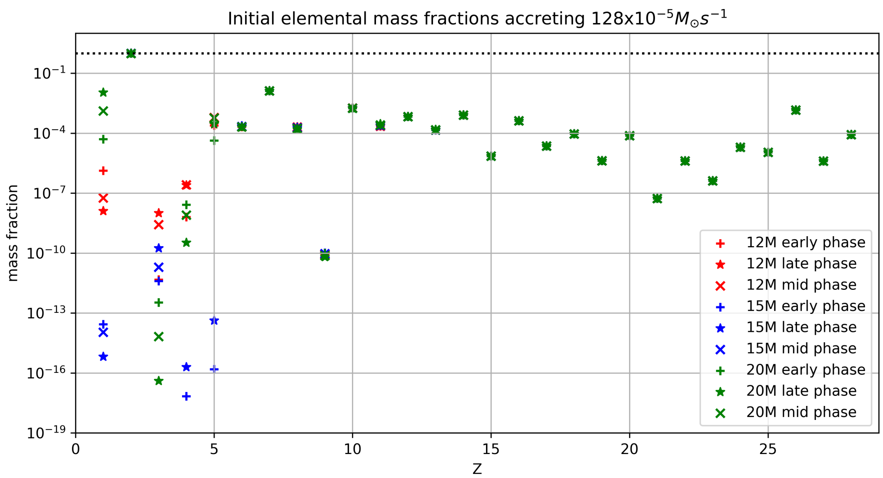

Figure 5.35: Initial elemental mass fractions for each environment for a common envelope accreting 128×10^{-5} $M_{\odot}s^{-1}$. Elements above

The initial mass fraction distribution for the 128×10^{-5} $M_{\odot}s^{-1}$ accretion rate is displayed in figure 5.35. Each environment accretes material that between 96.95% and 98.1% helium by mass. This means that every environment is now accreting material from the helium envelope, which will result in the system being dominated by α capture reactions. As all the environments are accreting material from the helium shell of the companion stars there is little variation in elements heavier than carbon. A small fraction of high energy alpha particles can continue to fuse with carbon to form oxygen however as the temperature is too low for this to have a large impact on the carbon and oxygen mass fractions.

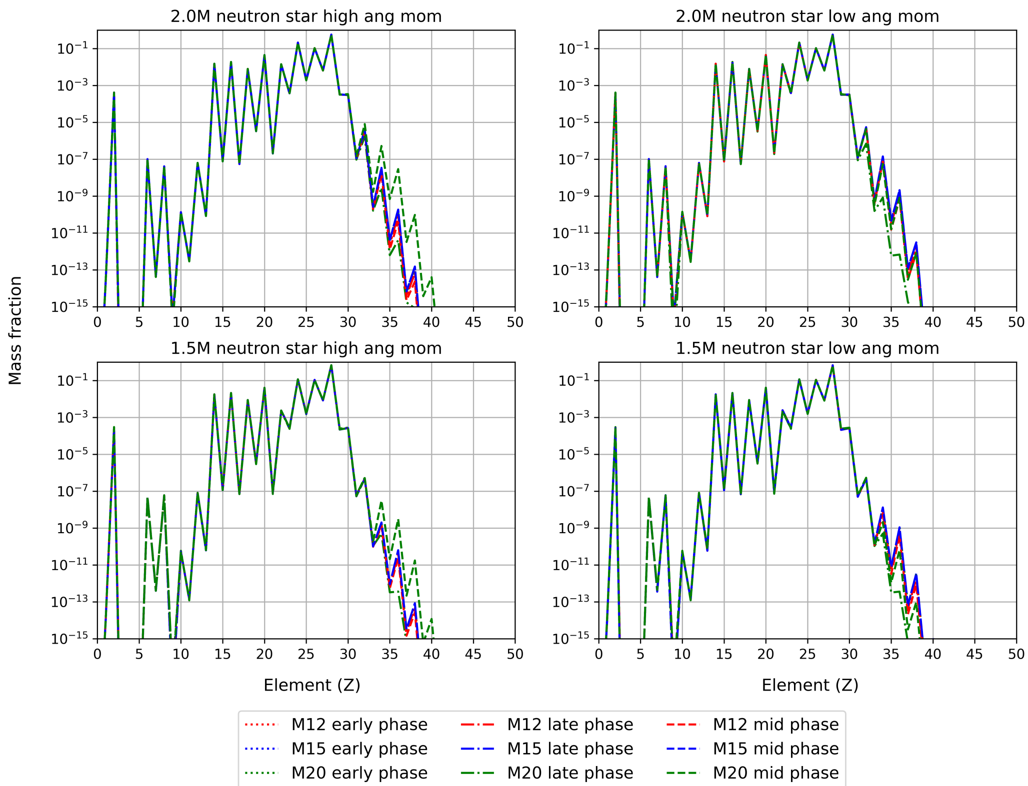

Figure 5.36: Elemental mass fraction distributions between greater than $128{\times}10^{-5}$ M$_\odot s^{-1}$ accretion rate for each neutron star mass and angular momentum. Dotted lines represent the early phase expansion, dashed lines represent mid phase expansion and dot-dashed lines represent late phase expansion. Companion masses of 12M$_\odot$ are shown in red, 15M$_\odot$ in blue and 20M$_\odot$ in green.

The final elemental mass fraction distributions in figure 5.36 all show identical mass fractions up to zinc from neutron star mass and angular momenta inside each companion mass and age. When the material in the accretion disk is closest to the neutron star the material spends enough time at high temperature to fully achieve NSE for low mass elements. A closer look into the region beyond zinc shows that there are trends in environment, angular momentum and neutron star mass. The most obvious difference occurs when the angular momentum, and as a result the time spent in the accretion disk, is varied. This is clearest in both the 12 and

$15M_{\odot}$ environments and is seen in all phases after the companion begins expansion.

Table 5.2: Elemental ratios for elements which vary in mass fraction across low angular momenta trajectories ($5 \times 10^{16} cm^2 s^{-1}$) over high angular momenta trajectories ($5 \times 10^{17} cm^2 s^{-1}$) for common envelopes inside a 12 and $15M_{\odot}$ companions

Element	$2.0M_{\odot}$ neutron star		$1.5M_{\odot}$ neutron star	
	average elemental ratio for $12M_{\odot}$ across all ages	average elemental ratio for $15M_{\odot}$ across all ages	average elemental ratio for $12M_{\odot}$ across all ages	average elemental ratio for $15M_{\odot}$ across all ages
	X_{low}/X_{high}	X_{low}/X_{high}	X_{low}/X_{high}	X_{low}/X_{high}
Ge	1.452	1.391	0.985	0.992
As	2.166	2.316	1.314	1.420
Se	4.733	4.134	5.702	6.537
Br	12.382	11.470	7.048	8.392
Kr	14.798	11.327	16.472	17.340
Rb	16.980	17.736	17.197	20.041
Sr	28.908	20.301	36.869	40.729

The average elemental ratios shown in table 5.2 highlight the difference as a result of neutron star mass and angular momentum. It is clear that higher Z elements have a larger difference in mass fraction in each binary system environment. Strontium is the final element to have a mass fraction greater than 1×10^{-15} in every environment, and it also has the largest mass fraction difference as a result of angular momentum. The $2.0M_{\odot}$ neutron star trajectories produce very similar mass fraction ratios for germanium, arsenic, selenium, bromine and rubidium in both the 12 and $15M_{\odot}$ environments, whereas krypton and strontium are both under produced in the $12M_{\odot}$ companion high angular momentum trajectory, leading to a higher ratio. The $1.5M_{\odot}$ trajectories in the $12M_{\odot}$ companion do not result in the same ratios as the $2.0M_{\odot}$. This is because the $1.5M_{\odot}$ neutron star trajectories spend longer in the accretion disk for both angular momenta, this produces larger amounts of the seed nuclei required to produce these elements as the heaviest of these elements (krypton, rubidium and strontium) are produced primarily via proton captures during the peak temperature. This explains why the elemental mass fractions are very similar for both neutron star masses with high angular momentum. Germanium, arsenic, selenium and bromine are all produced via different

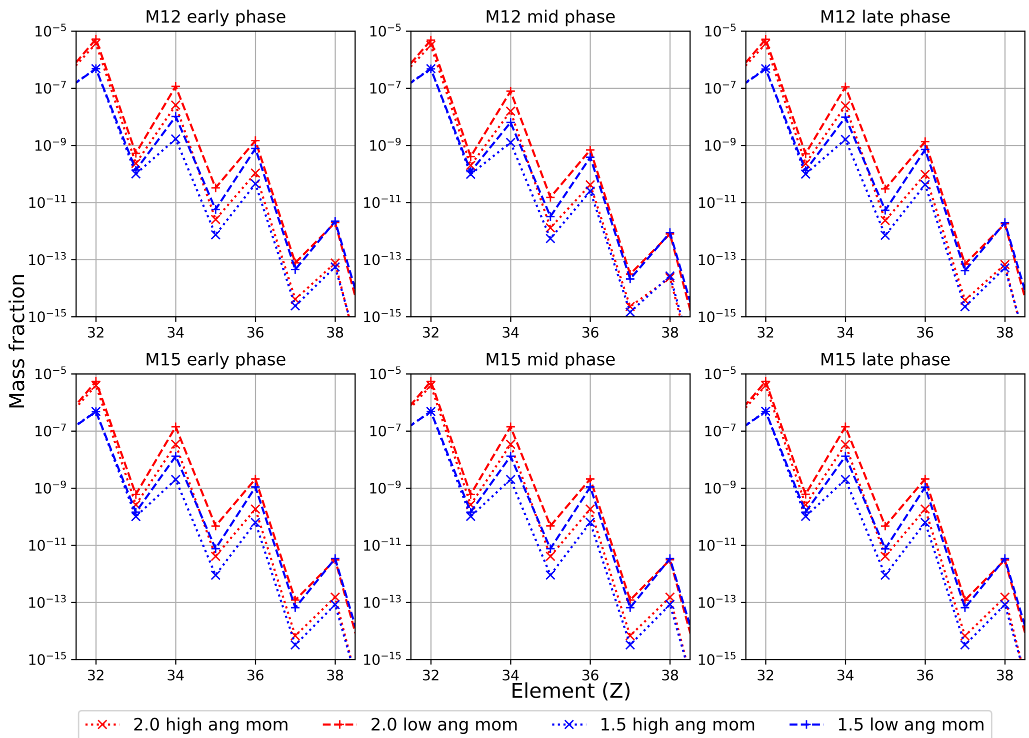

Figure 5.37: Elemental mass fraction distributions greater than $1{\times}10^{-15}$ for the $128{\times}10^{-5}$ $\mathrm{M}_{\odot}s^{-1}$ for each neutron star mass and angular momentum. Dotted lines represent the early phase expansion, dashed lines represent mid phase expansion and dot-dashed lines represent late phase expansion. Companion masses of $12\mathrm{M}_{\odot}$ are shown in red, $15\mathrm{M}_{\odot}$ in blue and $20\mathrm{M}_{\odot}$ in green.

methods, with isotopes being produced via α capture and neutron capture reactions in the lead up to the peak temperature, which are then also partially destroyed when the system reaches NSE.

Figure 5.37 shows the elemental mass fractions for a $12\mathrm{M}_{\odot}$ and $15\mathrm{M}_{\odot}$ companion for elements between germanium and strontium. It is important to note that bromine, krypton, rubidium and strontium result in elemental mass fractions that fall bellow the uncertainty threshold (depending on the neutron star mass and angular momentum).

5.3.9 $256{\times}10^{-5} M_{\odot} s^{-1}$ accretion rate

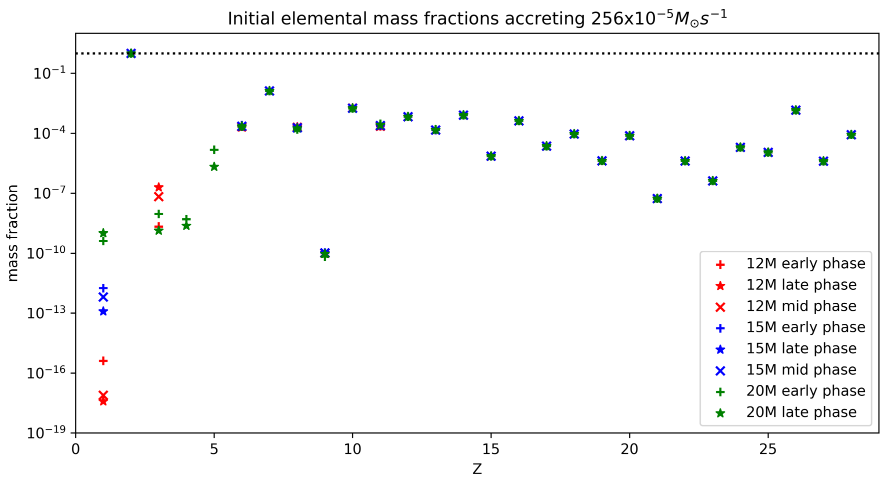

Figure 5.38: Initial elemental mass fractions for each environment for a common envelope accreting $256{\times}10^{-5}$ $\mathrm{M}_{\odot}s^{-1}$. Elements above

Figure 5.38 shows the initial mass fractions for each companion for the $256{\times}10^{-5}$ $\mathrm{M}_{\odot}s^{-1}$ accretion rate trajectory. This accretion rate is the first that is not reached in one of the companion environments. The 20$\mathrm{M}_{\odot}$ companion midway through expansion cannot achieve an accretion rate of this magnitude and so was not included in the analysis. The other eight environments all have identical initial mass fractions for elements beyond carbon. The 12$\mathrm{M}_{\odot}$ has the lowest initial hydrogen mass fraction and does not contain any beryllium or boron. The 15$\mathrm{M}_{\odot}$ does not contain any lithium, beryllium or boron. The innermost radii of this trajectory reach temperatures beyond 10GK, and are therefore beyond the temperature range of NuGrid. This means that the innermost radii cannot be included in the final averaged mass fractions and so the results from this accretion rate are averaged over all inner radii with a peak temperature below 10GK.

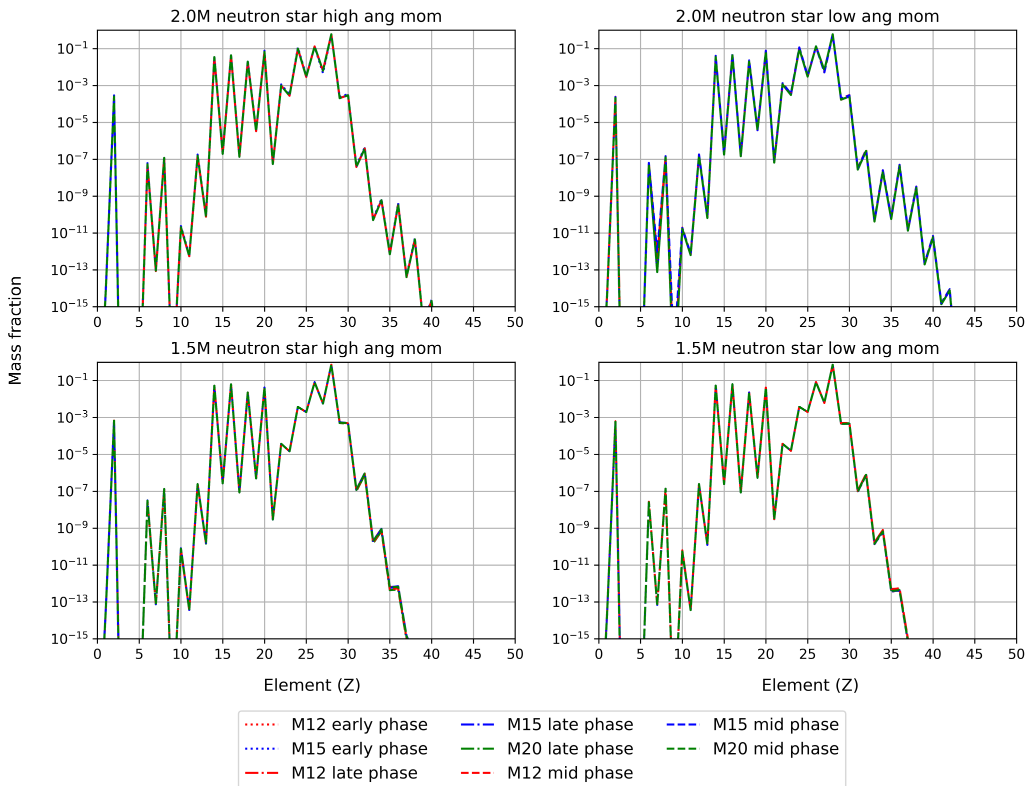

Figure 5.39: Elemental mass fraction distributions greater than $256\times10^{-5}M_{\odot}s^{-1}$ for each neutron star mass and angular momentum. Dotted lines represent the early phase expansion, dashed lines represent mid phase expansion and dot-dashed lines represent late phase expansion. Companion masses of 12M$_{\odot}$ are shown in red, 15M$_{\odot}$ in blue and 20M$_{\odot}$ in green.

Figure 5.39 shows the elemental mass fractions for each environment. For the 1.5M$_{\odot}$ neutron star trajectories the resulting elemental mass fraction distribution is nearly identical in every environment and for both angular momenta values, unlike the previous accretion rate where there were significant differences in elements beyond zinc. The mass fraction distribution from the 2.0M$_{\odot}$ neutron star trajectories are the same in each environment, but not identical for the different values of angular momentum and do not match the distribution from the 1.5M$_{\odot}$ neutron star. This indicates that the 2.0M$_{\odot}$ neutron star trajectories do not reach full NSE. The higher mass neutron star accelerates the material towards the centre of the accretion disk faster, resulting in less time spent in the NSE temperature region. Figure 5.40 shows the time spent above 1GK for each neutron star mass and angular momenta. Both $1.5M_{\odot}$ neutron star trajectories reach 1GK 5 seconds before the $2.0M_{\odot}$ neutron star trajectory. The difference in initial mass fractions from each environment do not impact the resulting nucleosynthesis as the hydrogen mass fraction is extremely small compared to the helium in every environment. This leads to α particle reaction channels such as (α, γ), (α, n) and (α, n) dominating the reaction flux.

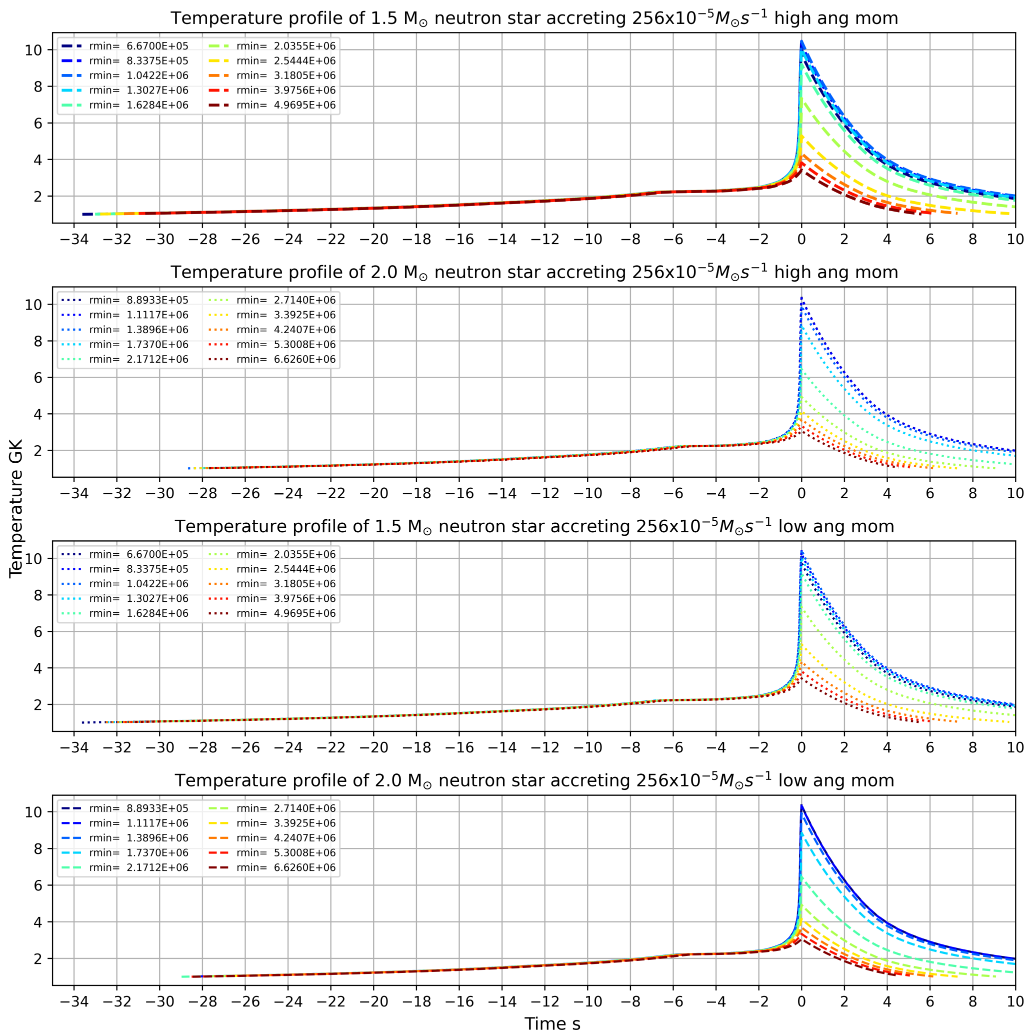

Figure 5.40: Time spent above 1GK for each neutron star mass and angular momenta for the $256{\times}10^{-5}$ M$_\odot s^{-1}$ accretion rate trajectory. The peak temperature is normalised to t=0.

5.3.10 $512\times10^{-5}M_{\odot}s^{-1}$ accretion rate

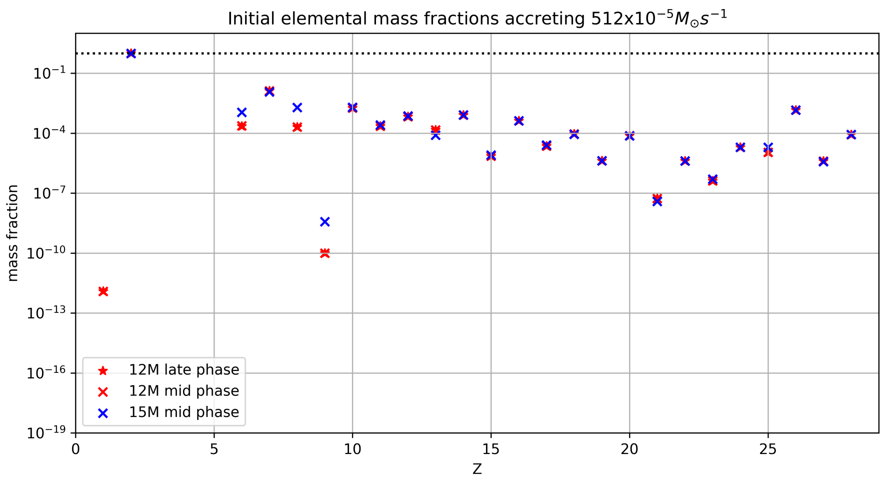

Figure 5.41: Initial elemental mass fractions for each environment for a common envelope accreting 512×10^{-5} $M_{\odot}s^{-1}$.

This accretion rate requires extremely dense material to be accreted from the companion to reach the mass transfer limit of 512×10^{-5} $M_{\odot}s^{-1}$. Figures 5.7 and 5.8 show that the required separation of the neutron star and the companion core are less than $2\times10^{-1}R_{\odot}$ at the end of the neutron star plunge in phase. This is only achieved in the late and mid phase of expansion of a 12$M_{\odot}$ companion and during the mid expansion phase of a 15$M_{\odot}$ companion. Figure 5.41 shows the initial mass fractions of these three environments and there are significant mass fraction differences as a result of companion mass. Both the 12 and 15$M_{\odot}$ common envelopes accrete material from the helium shell, however in the 15$M_{\odot}$ companion there is no hydrogen present in the initial mass fractions. It also has a higher fraction carbon, nitrogen and aluminium and a lower fraction of fluorine when compared to the 12$M_{\odot}$ initial mass fractions.

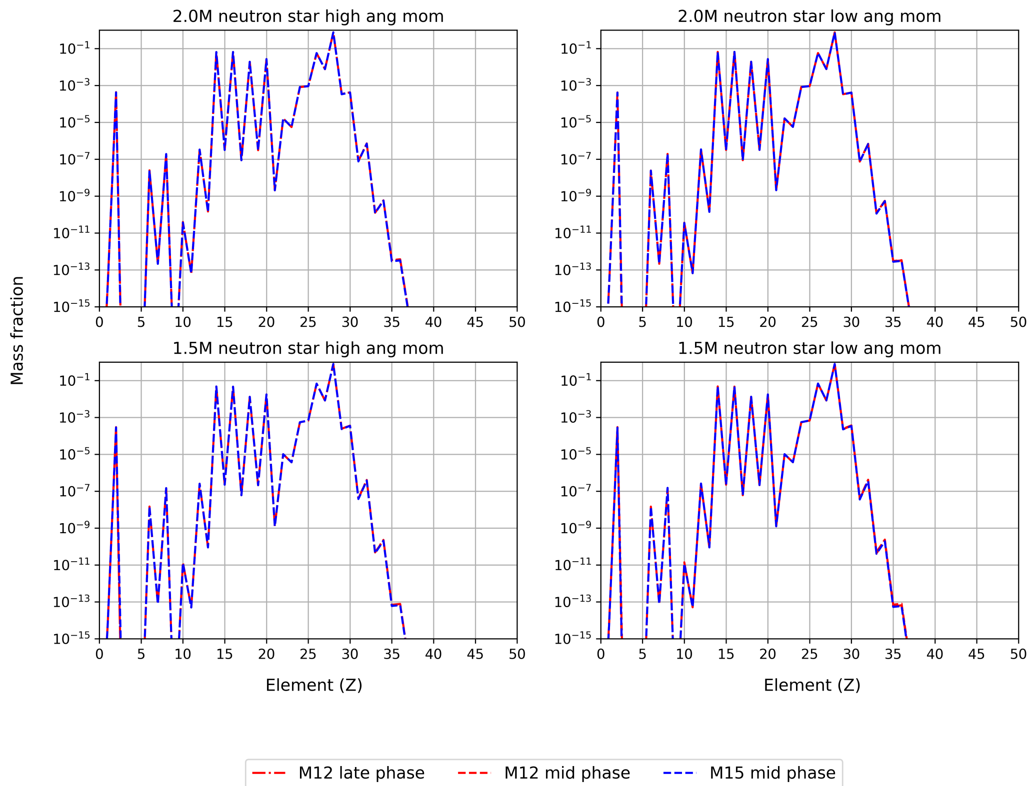

Figure 5.42: Elemental mass fraction distributions greater than $512{\times}10^{-5} M_{\odot} s^{-1}$ for each neutron star mass and angular momentum. Dotted lines represent the early phase expansion, dashed lines represent mid phase expansion and dot-dashed lines represent late phase expansion. Companion masses of 12M$_{\odot}$ are shown in red, 15M$_{\odot}$ in blue and 20M$_{\odot}$ in green.

This accretion rate reaches NSE in every environment, as shown by the large peak in nickel and the destruction of odd Z light elements up to silicon. Each neutron star mass and angular momenta result in the same distribution up to zinc, however the mass fraction of elements beyond zinc vary with neutron star mass. Table 5.3 shows the final elemental mass fractions for elements between gallium and krypton and also shows the ratio of mass fraction produced by a 2M$_{\odot}$ over the mass fraction produced by a 1.5M$_{\odot}$ neutron star. The table shows that the 2M$_{\odot}$ neutron star trajectories lead to between 1.73-5.17$\times$ the mass fraction of elements between gallium and krypton. As bromine and krypton are bellow $1{\times}10^{-12}$

they are bellow the elemental uncertainty the largest variation is selenium. Overall the different common envelope environments produce extremely similar mass fraction distributions for this accretion rate as a result of the high temperatures that are reached.

Table 5.3: Elemental mass fractions for elements between gallium and krypton for each neutron star mass, angular momentum and companion mass.

Element	High angular momentum					
	elemental mass fraction 2M$_\odot$ NS inside 12M$_\odot$ companion	elemental mass fraction 1.5M$_\odot$ NS inside 12M$_\odot$ companion	$\frac{X_{2M\odot}}{X_{1.5M\odot}}$	elemental mass fraction 2M$_\odot$ NS inside 15M$_\odot$ companion	elemental mass fraction 1.5M$_\odot$ NS inside 15M$_\odot$ companion	$\frac{X_{2M\odot}}{X_{1.5M\odot}}$
Ga	7.94×10^{-8}	4.03×10^{-8}	1.97	7.62×10^{-8}	3.78×10^{-8}	2.01
Ge	7.17×10^{-7}	4.03×10^{-7}	1.78	6.98×10^{-7}	3.80×10^{-7}	1.84
As	1.25×10^{-10}	4.74×10^{-11}	2.63	1.21×10^{-10}	4.34×10^{-11}	2.78
Se	5.87×10^{-10}	2.26×10^{-10}	2.60	5.70×10^{-10}	2.07×10^{-10}	2.76
Br	3.37×10^{-13}	6.82×10^{-14}	4.94	2.94×10^{-13}	5.99×10^{-14}	4.90
Kr	3.74×10^{-13}	7.60×10^{-14}	4.92	3.26×10^{-13}	6.67×10^{-14}	4.88
Element	low angular momentum					
	elemental mass fraction 2M$_\odot$ NS inside 12M$_\odot$ companion	elemental mass fraction 1.5M$_\odot$ NS inside 12M$_\odot$ companion	$\frac{X_{2M\odot}}{X_{1.5M\odot}}$	elemental mass fraction 2M$_\odot$ NS inside 15M$_\odot$ companion	elemental mass fraction 1.5M$_\odot$ NS inside 15M$_\odot$ companion	$\frac{X_{2M\odot}}{X_{1.5M\odot}}$
Ga	7.52×10^{-8}	3.96×10^{-8}	1.90	7.31×10^{-8}	3.57×10^{-8}	2.05
Ge	6.89×10^{-7}	3.99×10^{-7}	1.73	6.73×10^{-7}	3.61×10^{-7}	1.86
As	1.19×10^{-10}	4.64×10^{-11}	2.56	1.13×10^{-10}	4.04×10^{-11}	2.80
Se	5.61×10^{-10}	2.21×10^{-10}	2.54	5.33×10^{-10}	1.92×10^{-10}	2.77
Br	2.99×10^{-13}	6.48×10^{-14}	4.61	2.77×10^{-13}	5.32×10^{-14}	5.20
Kr	3.31×10^{-13}	7.22×10^{-14}	4.59	3.07×10^{-13}	5.94×10^{-14}	5.17

5.3.11 $1024{\times}10^{-5}M_{\odot}s^{-1}$ accretion rate

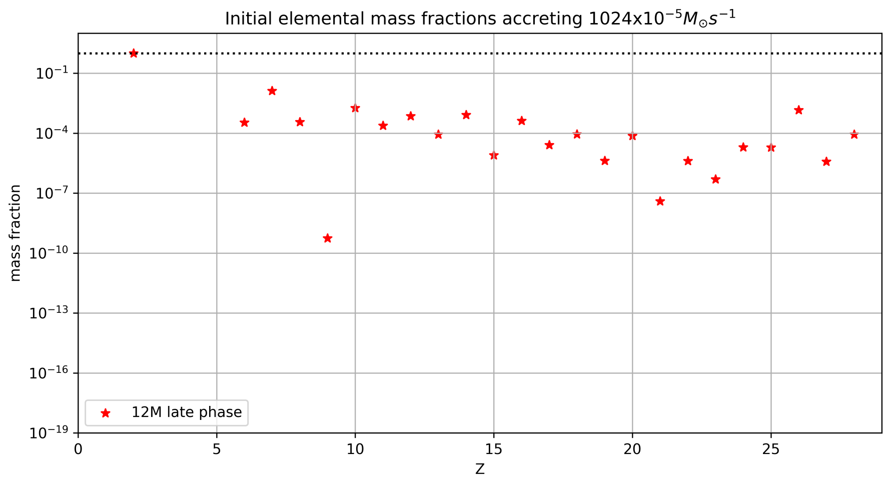

Figure 5.43: Initial elemental mass fractions for each environment for a common envelope accreting $1024{\times}10^{-5}$ $M_{\odot}s^{-1}$. Elements above

The only environment able to generate an accretion rate of $1024{\times}10^{-5}$ $M_{\odot}s^{-1}$ is the $12M_{\odot}$ companion during the late phase of expansion. Like the $15M_{\odot}$ companion environment in the last accretion rate, this has no hydrogen, lithium, beryllium or boron in the initial composition.

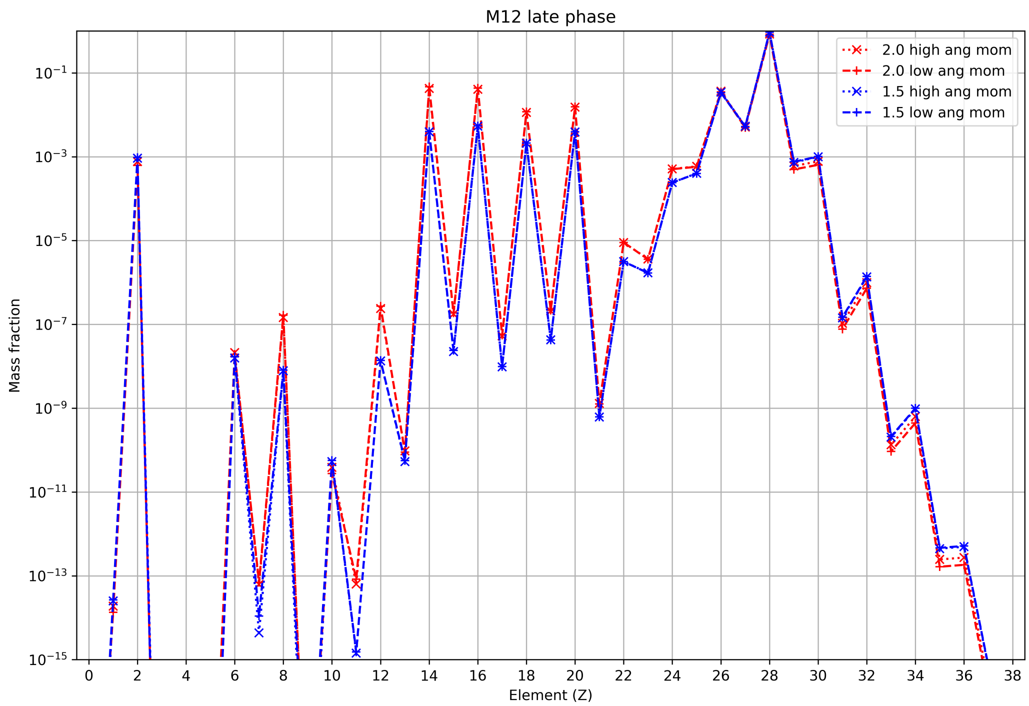

Figure 5.44: Elemental mass fraction distributions greater than $1024{\times}10^{-5}M_{\odot}s^{-1}$ for each neutron star mass and angular momentum. Dotted lines represent the early phase expansion, dashed lines represent mid phase expansion and dot-dashed lines represent late phase expansion. Companion masses of 12M$_{\odot}$ are shown in red, 15M$_{\odot}$ in blue and 20M$_{\odot}$ in green.

The final elemental mass fraction distribution for each trajectory inside the 12M$_{\odot}$ companion are shown in figure 5.44. As this accretion rate is only relevant for the 12M$_{\odot}$ companion each neutron star mass and angular momentum trajectory can be plotted on one figure. This highlights the differences due to neutron star mass, unlike the previous environments where the higher neutron star mass results in larger mass fractions of elements beyond nickel however this environment shows the 1.5M$_{\odot}$ neutron star producing higher fractions of elements from copper to krypton. It also underproduces elements leading up to nickel when compared to the 2.0M$_{\odot}$ trajectories. Further investigation into the flux before NSE shows that the different neutron star mass trajectories lead to different reaction pathways. Figure 5.45 shows the integrated reaction flux at 2GK in for each neutron star mass and angular momentum. This occurs before NSE and shows the flux from all reactions within 5 orders of magnitude of the strongest reaction channel. The most obvious difference is seen in the high angular momentum 1.5$M_\odot$ neutron star flux, which does not show the same variety of reactions occurring with the CNO region as the other environments. The 1.5$M_\odot$ neutron star with low angular momentum has the same flux in the CNO region as the 2$M_\odot$ neutron star trajectories but results in the same mass fraction distribution as the 1.5$M_\odot$ high angular momentum. Therefore, for this accretion rate the reaction pathways that occur before the peak temperature are not important as it undergoes NSE. The time spent in NSE does impact the mass fraction distribution as the 2$M_\odot$ spends less time in NSE and produces higher fractions of elements bellow nickel, whereas the 1.5$M_\odot$ neutron star spends more time in NSE and produces higher fractions of elements above nickel.

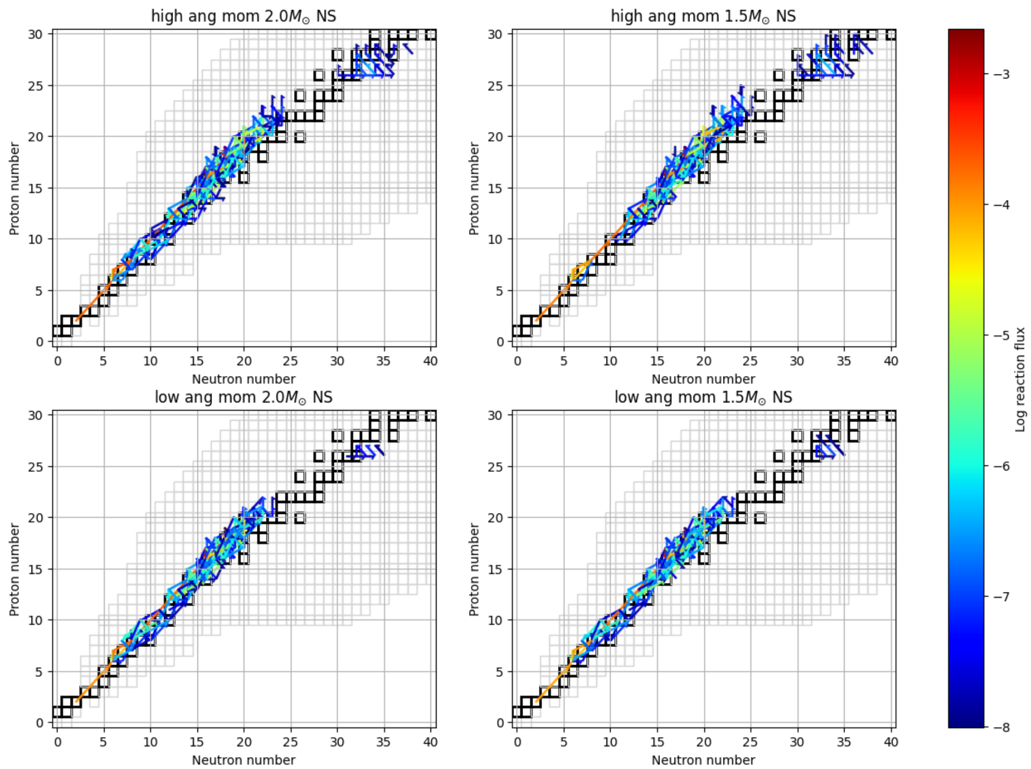

Figure 5.45: Integrate reaction fluxes ($\Sigma\frac{dY}{dt}$) at 2GK in for each neutron star mass and angular momentum inside the 12 M$_\odot$ companion during the late expansion phase.

5.4 Nucleosynthesis in Z=0.02 solar like material

Due to the use of initial mass fractions taken from [54] the nucleosynthesis is limited as all isotopes beyond ^{62}Ni were not included in the network used to calculate the evolution of the companion. As the companion stars are solar like in composition, with Z=0.02, it is important to include the heavy isotopes seen in solar composition to understand how this would impact further nucleosynthesis. Trajectories that enter NSE will not be investigated because during NSE the resulting mass fraction distribution is dependent on the availability of protons, neutrons or α particles, otherwise known as the electron fraction. This will result in the same elemental mass fraction distribution as the heavy seed nuclei will be destroyed during NSE. Four environments were rerun with solar seed nuclei. Each environment was chosen to further investigate the different nucleosynthetic processes that were seen when using the [54] initial mass fractions.

5.4.1 The rp-process in a 1.5M$_{\odot}$ neutron star accreting 32$\times$10^{-5} M$_{\odot}s^{-1}$ from a 20M$_{\odot}$ companion.

To understand the impact that heavy seed nuclei have on the common envelope the trajectories were rerun with the initial mass fractions extending up to uranium. The mass fractions for elements between copper and uranium are taken from the solar composition used in [31]. Including these elements the initial mass fraction is greater than 1 by 3.419×10^{-6}. This was then re-normalised, so the total mass fraction is equal to 1. The normalised initial mass fraction is shown in figure 5.46 by the red crosses. The same mass fraction for the heavy seed nuclei is used for all environments that were investigated. All heavy seed nuclei above iron are not produced during the lifetime of the companion star but are from previous astrophysical events, such as core collapse supernovae or merger events, that occur before the formation of the binary system. Therefore, only stable nuclei are included as unstable heavy seeds will have decayed. The initial composition consists of 51% hydrogen, 46% helium with the rest made up from seed nuclei. The maximum temperature of this trajectory is 6.1GK, so rapid proton captures are expected to occur, but the trajectory will also be within the NSE temperature range for a short time.

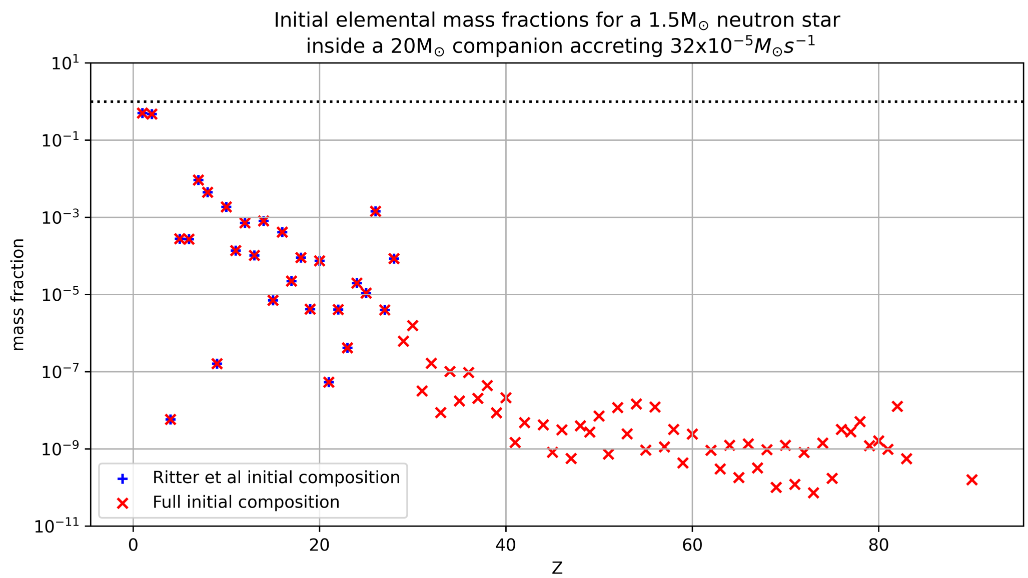

Figure 5.46: The initial mass fractions used for a 1.5M$_{\odot}$ neutron star inside a 20M$_{\odot}$ companion accreting 32$\times$10^{-5}$M_{\odot}s^{-1}$. Each elemental mass fraction has been normalised, so the total is equal to one. Red Xs show the new initial composition, blue crosses show the initial mass fractions used in the previous tests, taken from [54].

The successive proton captures seen in the 20M$_{\odot}$ environments in figure 5.29 indicate rapid proton capture is occurring inside the common envelope. The extended initial composition, as seen in figure 5.46, will allow these proton captures onto intermediate and heavy isotopes much earlier in the trajectory. Figure 5.47 shows the finial isotopic mass fractions for each initial composition. Including heavy seed nuclei allow production of proton rich nuclei all the way up to bismuth and polonium. Comparing both initial compositions it is clear that including the trace amounts of stable heavy nuclei result in proton capture reactions well beyond nickel.

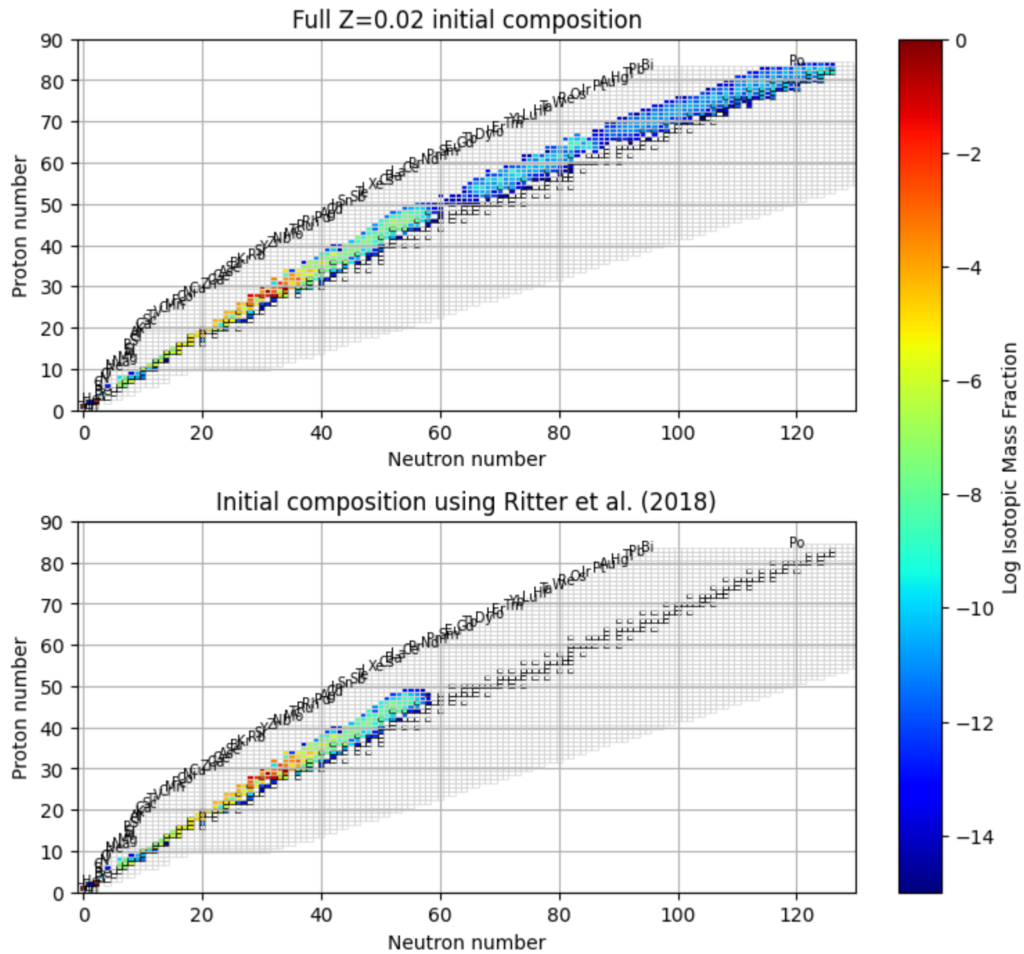

Figure 5.47: Isotopic mass fractions for a 1.5M$_\odot$ neutron star accreting $32{\times}10^{-5}M_\odot s^{-1}$ from a 20M$_\odot$ companion using [54] initial mass fractions (bottom) and including seed nuclei for Z>28 (Top).

The distribution of isotopes below tin are very similar in both cases. Figure 5.48 shows the ratio of final isotopic mass fraction for the full initial composition compared to only the [54] initial composition. This ratio is only for isotopes with a mass fraction greater than $1{\times}10^{-15}$ in both scenarios. This shows that the final mass fraction is the same for isotopes below atomic mass = 94 for both initial mass fractions. The extra seed nuclei between ^{62}Ni and atomic mass = 94 do not contribute to the production of these isotopes but increase the fraction of the tin, indium and cadmium isotopes that are produced.

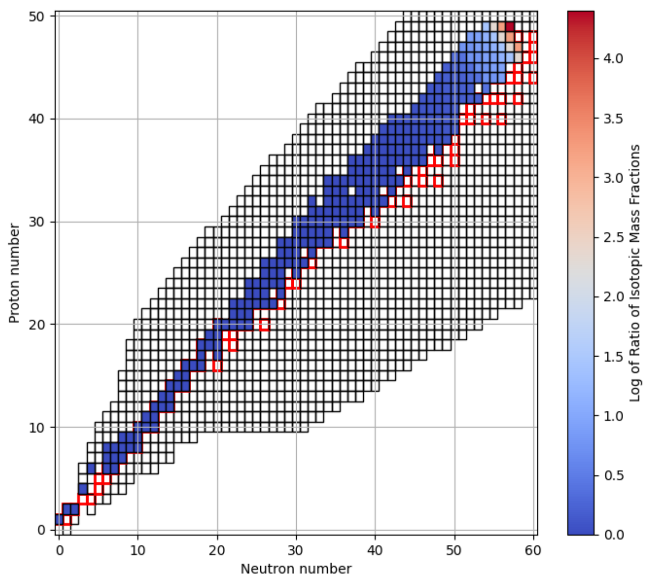

Figure 5.48: The ratio of isotopic mass fraction produced using [54] with solar seed nuclei over the isotopic mass fraction produced using only the initial mass fractions taken from [54]. The ratio is only for isotopes with a mass fraction greater than $1{\times}10^{-15}$ in both scenarios.

Once again looking at the reaction flux before the peak temperature it is clear that the rapid proton capture process is occurring inside this environment, but with the inclusion of seed nuclei above ^{62}Ni the full rp-process pathway is in use, up to the tin tellurium cycle. Figure 5.49 shows the reaction flux produced from both initial compositions when the temperature reaches 1GK. When using the full distribution of solar seed rp-process nucleosynthesis is clearly the dominant reaction pathway, but for isotopes beyond Z=50 the proton captures only occur on stable isotopes. This is due to much smaller mass fraction of stable isotopes in this region and the much higher energy required to capture a proton onto these heavy nuclei. This combined with the short half-life of the unstable proton rich nuclei results in single proton captures followed by β decay back to stability.

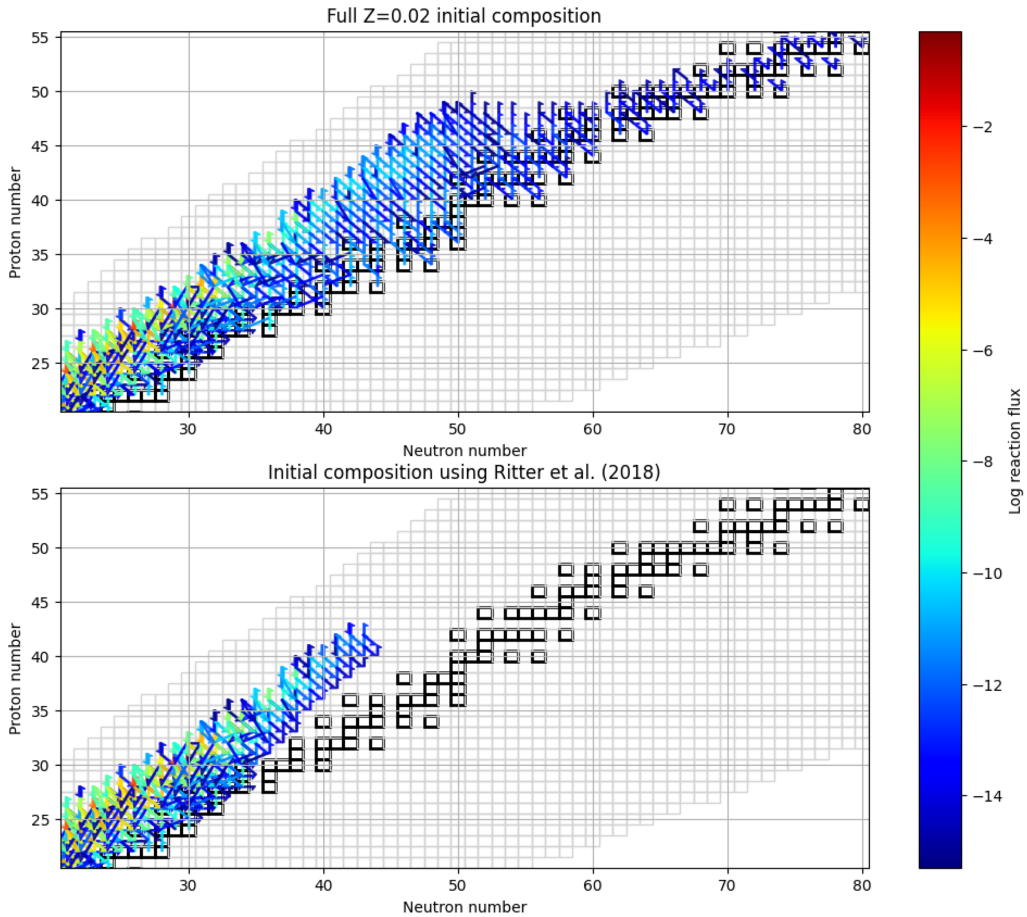

Figure 5.49: Reaction flux ($fracdYdt$) at 1GK for a 1.5M$_\odot$ neutron star accreting 32×10^{-5} M$_\odot s^{-1}$ from a 20M$_\odot$ using [54] including solar seed nuclei (Top) and using only initial mass fractions from [54].

Comparing the reaction fluxes and isotopic mass fractions produced from both initial compositions shows that the inclusion of solar seed nuclei do not change the mass fractions of isotopes below nickel and do not change the reaction pathways that are used. Using the full range of solar seed nuclei also produce a wide range of proton rich heavy isotopes. This shows that the common envelope accretion disk is a possible site for the rapid proton capture process to occur and figure 5.47 shows that proton rich material can be ejected out of the disk at the end of the trajectory.

5.4.2 Neutron capture processes in a 1.5M$_\odot$ neutron star accreting 32×10^{-5} M$_\odot s^{-1}$ from a 15M$_\odot$ companion.

The 15M$_\odot$ companion accreting $32\times10^{-5} M_\odot s^{-1}$ showed evidence of slow neutron captures before the trajectory reached peak temperature. The neutrons are produced via (α,n) reactions will be able to capture onto heavy nuclei much earlier in the trajectory evolution as these heavy isotopes will already be in the material. Figure 5.50 shows the isotopic mass fractions produced using just [54] initial mass fractions (bottom) and the [54] with heavy seed nuclei. The extended initial composition produces much heavier isotopes on both the proton and neutron rich side of stability.

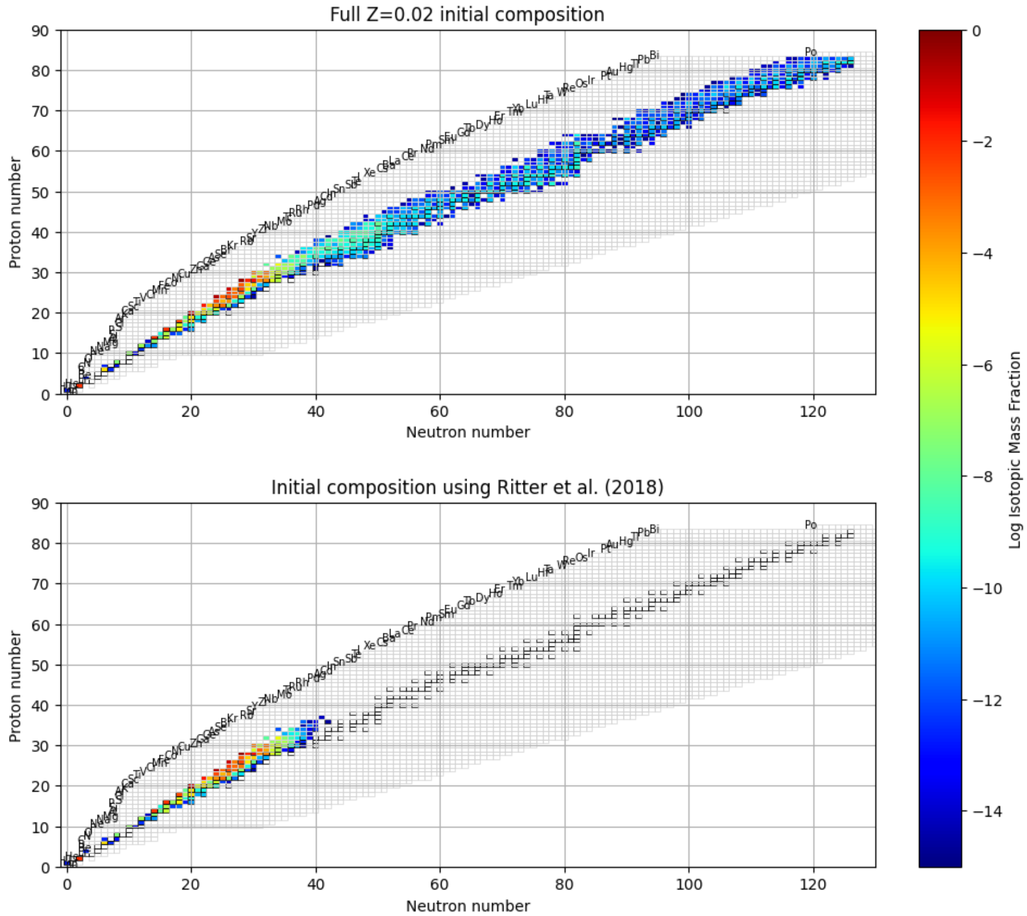

Figure 5.50: Isotopic mass fractions for a 1.5M$_\odot$ neutron star accreting $32{\times}10^{-5}M_\odot s^{-1}$ from a 15M$_\odot$ companion using [54] initial mass fractions (bottom) and including seed nuclei for Z>28 (Top).

This trajectory showed evidence of slow neutron captures leading up to the peak temperature, in which it entered NSE and resulted in the same mass fraction distribution as all NSE trajectories. The heavy seed nuclei are not destroyed during NSE and provide a base for proton, neutron and α capture reactions. The same final mass fraction distribution is seen for elements below atomic mass = 68 as seen in figure 5.51. Like in the 20M$_\odot$ test, the final isotopic mass fraction from the network with all seed nuclei do not change the type of nucleosynthesis that occurs but allow the material to reach much heavier isotopes using the same types of reactions.

For all isotopes below ^{62}Ni the resulting mass fractions are within 1%, showing that the inclusion of the heavy seed nuclei do not impact the types of nucleosynthesis that occur in the low mass region.

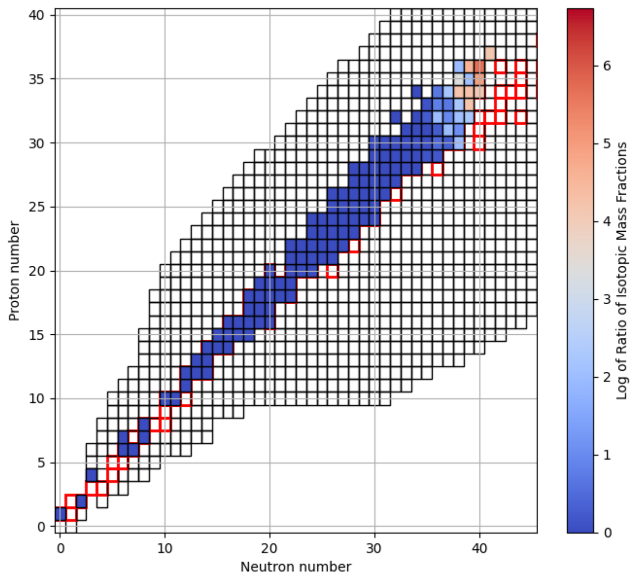

Figure 5.51: The ratio of isotopic mass fraction produced using [54] with solar seen nuclei over the isotopic mass fraction produced using only the initial mass fractions taken from [54]. The ratio is only for isotopes with a mass fraction greater than 1×10^{-15} in both scenarios.

Looking at the reaction flux at 1GK in figure 5.52 shows that there are neutrons available which lead to neutron captures on all stable isotopes in the climb up to the peak temperature, which was also seen in 5.29 for the $15M_{\odot}$ environment.

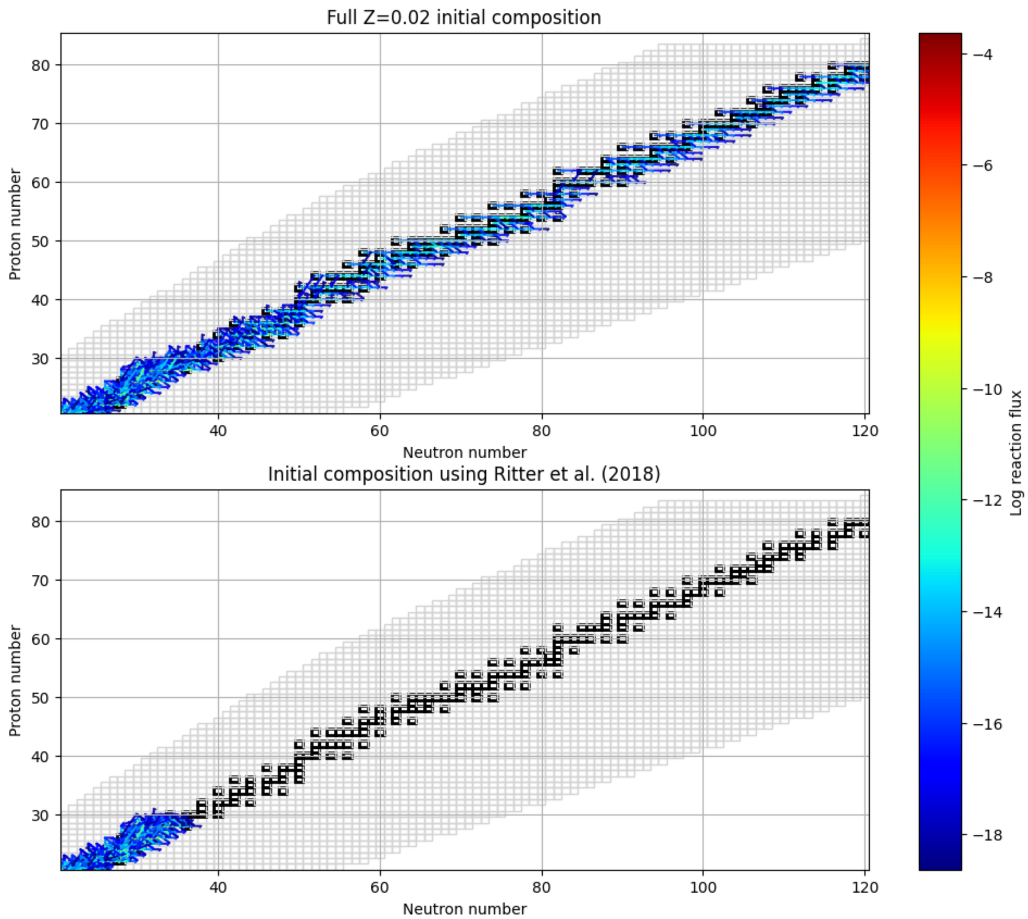

Figure 5.52: Reaction flux ($\frac{dY}{dt}$) at 1GK for a 1.5M$_\odot$ neutron star accreting 32$\times$10^{-5} M$_\odot s^{-1}$ from a 15M$_\odot$ using [54] including solar seed nuclei (Top) and using only initial mass fractions from [54].

5.4.3 The α-process from a 1.5M$_\odot$ neutron star accreting 8×10^{-5} M$_\odot s^{-1}$ from a 12M$_\odot$ companion.

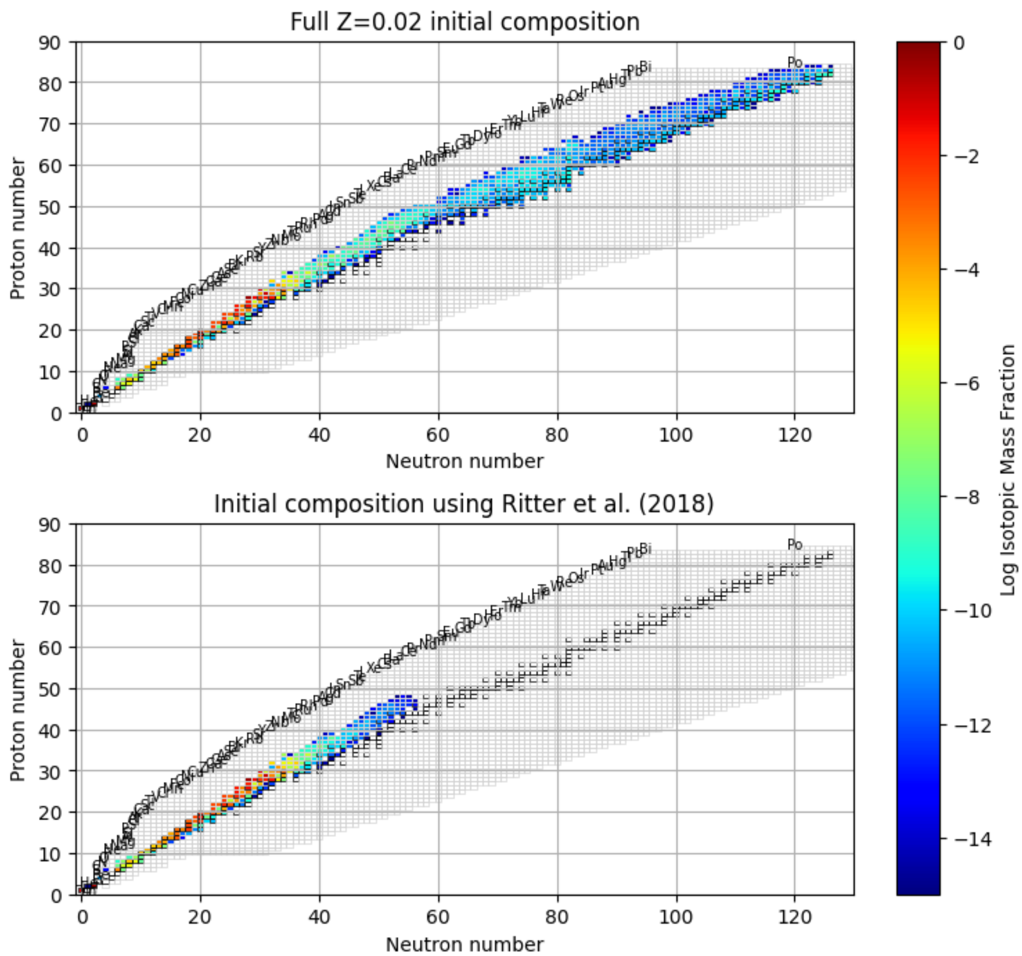

Figure 5.53: Isotopic mass fractions for a 1.5M$_\odot$ neutron star accreting $8\times10^{-5}M_\odot s^{-1}$ from a 12M$_\odot$ companion using [54] initial mass fractions (bottom) and including seed nuclei for Z>28 (Top).

With the full solar seed nuclei the final isotopic mass fraction distribution once again produces heavy elements such as bismuth and polonium. The alpha capture process that is seen in figure 5.23 is extended, with alpha and proton capture reactions occurring beyond nickel. When compared to the $20M_\odot$ rp-process environment the final isotopic distribution is not as far into the proton rich area of the isotopic chart. This is because the initial composition of the material in this environment contains more helium, He = 80.2%, than hydrogen, H = 17.7%.

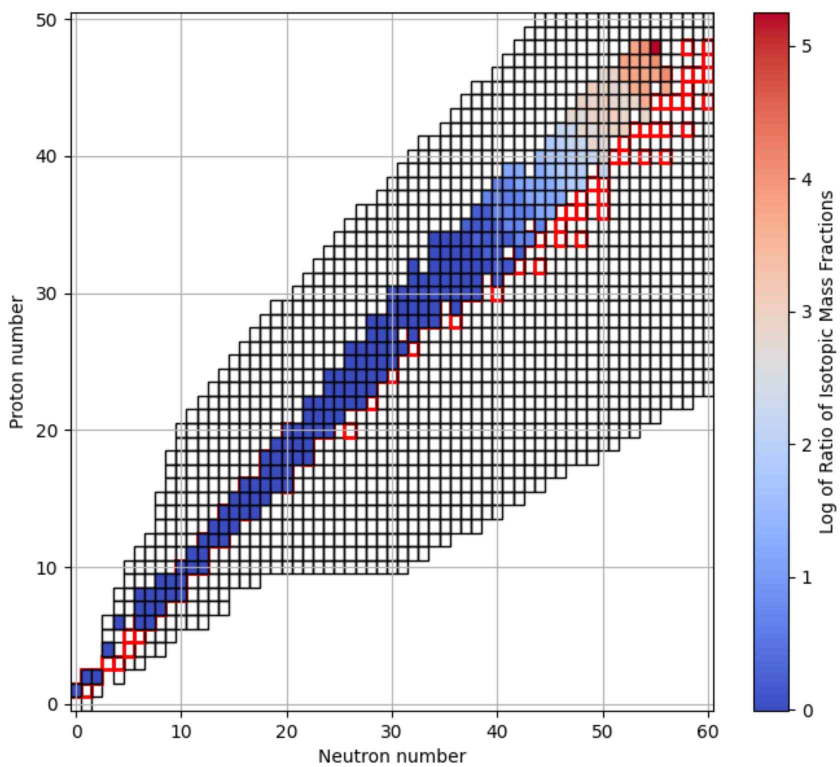

Figure 5.54: The ratio of isotopic mass fraction produced using [54] with solar seen nuclei over the isotopic mass fraction produced using only the initial mass fractions taken from [54]. The ratio is only for isotopes with a mass fraction greater than 1×10^{-15} in both scenarios.

Figure 5.54 shows the ratio of isotopes with a mass fraction greater than 1×10^{-15} in both environments, dividing the isotopic mass fraction produced from the full initial composition by the isotopic mass fraction produced when using only [54] initial mass fractions. The ratio shows that the only differences in isotopic mass fractions are for isotopes heavier than nickel. The different initial mass fractions lead to very similar distributions of isotopes below nickel. Table 5.4 shows the final isotopic mass fractions of isotopes within two orders of magnitude of the largest mass fraction. Of these isotopes the largest mass fraction difference is seen in ^{52}Fe. The final mass fractions produced using each initial composition are within 1% for isotopes within the largest two orders of magnitude, which shows that adding in the heavy seed nuclei has not changed the resulting mass fraction distributions for elements bellow and including zinc.

Table 5.4: Isotopic mass fractions for elements between gallium and krypton for each neutron star mass, angular momentum and companion mass.

Isotope	isotopic mass fraction using Z=0.02 seed nuclei	isotopic mass fraction using [54]	$\frac{X_{Full}}{X_{Ritter}}$
^{1}H	0.0402542	0.0402371	100.04232%
^{4}He	0.1525724	0.1525747	99.998479%
^{39}K	0.0216995	0.0216989	100.00277%
^{40}Ca	0.0119336	0.0119376	99.966461%
^{46}Ti	0.0122077	0.0122023	100.04447%
^{50}Cr	0.0109626	0.0109602	100.02213%
^{51}Mn	0.0209730	0.0210054	99.845509%
^{52}Fe	0.0161483	0.0163051	99.038294%
^{54}Fe	0.0316973	0.0316309	100.21006%
^{55}Co	0.0124434	0.0124418	100.01228%
^{56}Ni	0.4005458	0.4005200	100.00644%
^{57}Ni	0.0268331	0.0268332	99.999741%
^{59}Ni	0.0135491	0.0135448	100.03143%
^{60}Ni	0.0208910	0.0208793	100.05595%
^{60}Cu	0.1021150	0.1020571	100.05671%
^{60}Zn	0.0406080	0.0405855	100.05546%

5.5 Summary of common envelope accretion disk data

The accretion disk inside a common envelope can eject material back into the common envelope after it undergoes a variety of different nucleosynthetic processes. The distance at which the material is ejected leads to different isotope production, with material close to the centre of the accretion disk reaching the highest temperatures. For low accretion rates this results in more proton capture reactions, and for higher accretion rates the material enters NSE faster.

The link between accretion rate and binary separation leads to the largest difference in nucleosynthesis. The main type of reaction to occur is dependent on the fractions of hydrogen and helium in the initial composition and this is calculated from the separation of the companion and neutron star. Higher accretion rates ($> 64 \times 10^{-5} M_{\odot} s^{-1}$) occur in the helium envelope and lead to alpha capture and, in some cases, neutron capture. The lower accretion rates ($< 8 \times 10^{-5} M_{\odot} s^{-1}$) are mostly composed of hydrogen and so result in successive proton captures.

Including an extended network of solar seed nuclei above nickel did not change the mass fraction of isotopes below nickel. Including the seed nuclei produced heavy isotopes in all environments for accretion rates that were run with full initial abundances. The distribution of heavy isotopes produced is dependent on the type of nucleosynthesis that dominates the simulation. For an accretion disk accreting $32 \times 10^{-5} M_{\odot} s^{-1}$ inside a $20\mathrm{M}_{\odot}$ companion, proton capture reactions dominate the nucleosynthetic pathways which result in production of proton rich isotopes. The $15\mathrm{M}_{\odot}$ companion scenario undergoes many (α, n) reactions. This produces a mixture isotopes distributed across both sides of the valley of stability as free neutrons produced via (α, n) are then captured onto heavy nuclei making neutron rich isotopes, while alpha capture reactions continue to produce proton rich nuclei.

It is likely that including the full network of seed nuclei for every possible combination of neutron star mass, angular momentum, companion mass and companion age will produce heavy isotopes dependent on the initial mass fractions of hydrogen and helium.

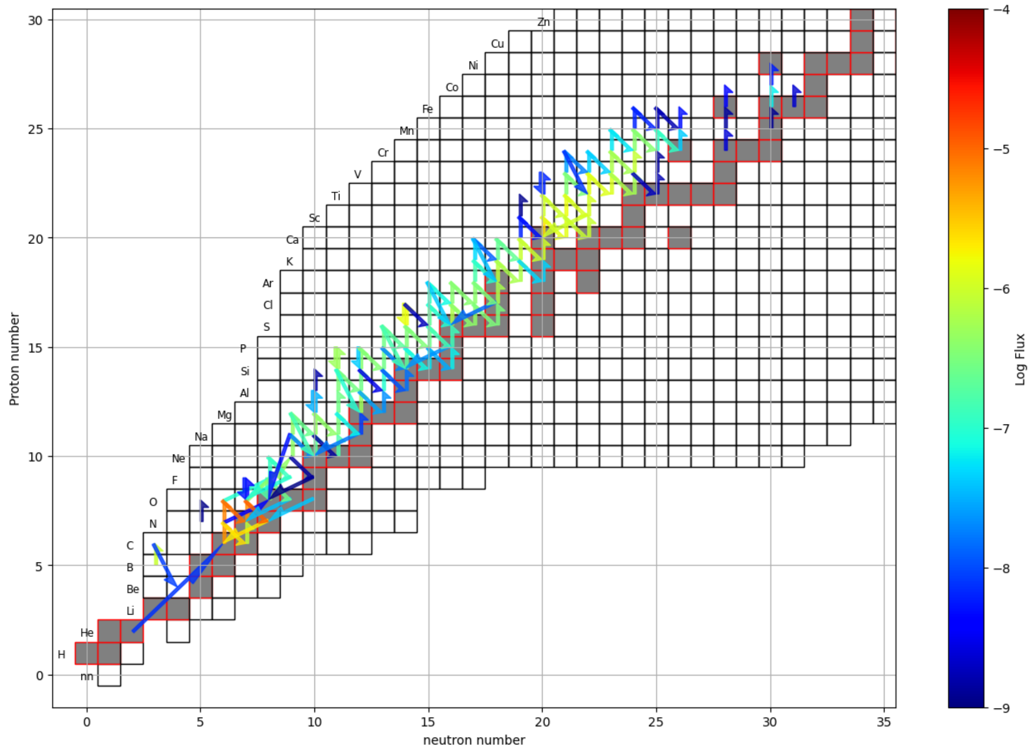

Figure 5.55: Instantaneous reaction flux ($\frac{dY}{dt}$)for a 2M$_\odot$ neutron star inside a 20M$_\odot$ companion accreting $32 \times 10^{-5} M_\odot s^{-1}$.

Figure 5.55 shows the non-intergrated reaction flux for a single time-step during common envelope accretion around a 2M$_\odot$ neutron star accreting hydrogen rich material from a 20M$_\odot$ companion at $32 \times 10^{-5} M_\odot s^{-1}$. This clearly shows the reaction pathway, following successive proton captures, however it does not include the expected (α, p) reactions at ^{18}Ne, ^{22}Ne and ^{30}S as the common envelope trajectories spend much less time above 1GK compared to the studies conducted in [60]. Instead, material β^- decays back to stable isotopes before continuing proton capture reactions. This type of nucleosynthesis is seen in all environments with hydrogen rich initial mass fractions and as these occur at low accretion rates the final mass fraction distribution consists of proton rich material, as seen in figure 5.47.

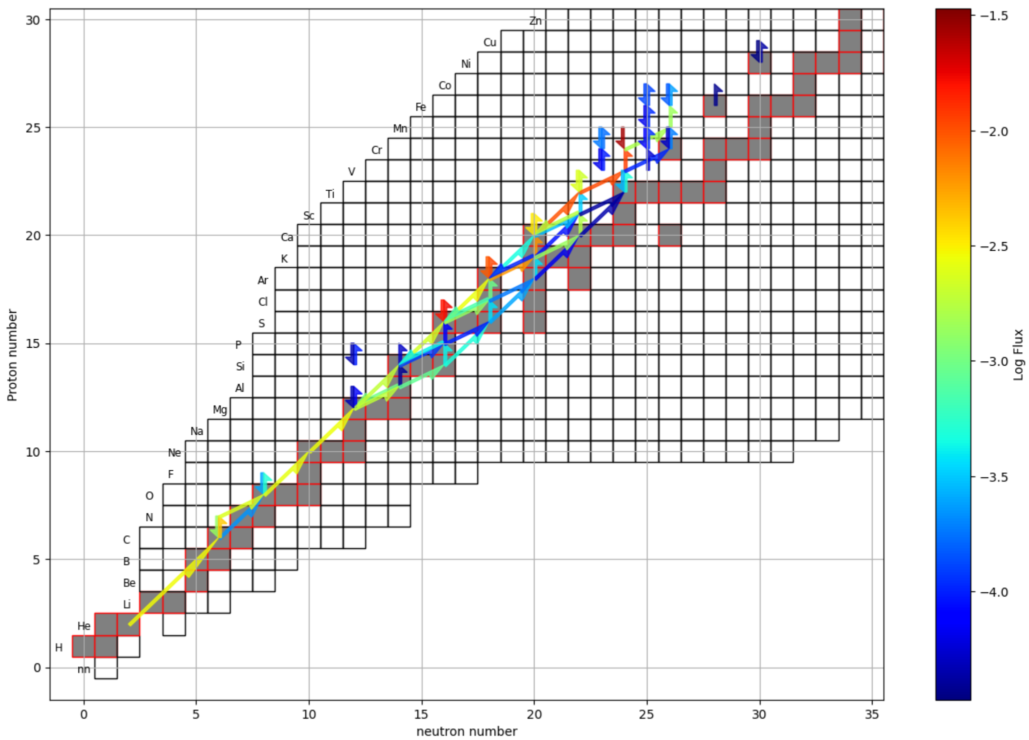

Figure 5.56: Instantaneous reaction flux ($\frac{dY}{dt}$) for a $2M_{\odot}$ neutron star inside a $15M_{\odot}$ companion accreting $32 \times 10^{-5} M_{\odot} s^{-1}$.

Figure 5.56 shows the reaction pathways inside the common envelope accretion disk around a $2M_{\odot}$ neutron star accreting helium rich material from a $15M_{\odot}$ companion at $32 \times 10^{-5} M_{\odot} s^{-1}$. This clearly shows the flow of (α, γ) and (α, p) reactions which create heavy isotopes. It also shows proton capture reactions, however this is not rapid proton capture as the initial fraction of hydrogen is too small to follow the expected reaction pathways seen in [60]. All environments accreting material from the helium envelope show evidence of this type of nucleosynthesis however for many of these accretion rates the temperatures reach into NSE and the material does not reach past nickel.

Chapter 6

Conclusions and future work

In this work three main projects were addressed. The first investigated the impact of using different generations of nuclear physics libraries when modelling different astrophysical scenarios. For simple scenarios such as the hydrostatic burn trajectory this had very little impact as the reaction rates used in these environments are experimentally determined and extensively studied. However, when modelling more extreme scenarios such as an X-ray burst or r-process the different versions of Reaclib produce differences greater than an order of magnitude in isotopic and elemental mass fractions. When updating to the latest version of JINA Reaclib 2021 the X-ray burst trajectory shows differences in elements between iodine and praseodymium and the r-process trajectory shows differences in elements beyond nickel, with the difference getting larger as proton number increases. When the supplementary libraries of KADoNiS, Illiadis 2001 and VITAL were removed and JINA Reaclib 2021 was used the r-process environment showed that including the outdated supplementary libraries under produced all elements above boron by an order of magnitude. When using only Reaclib 2021 the elemental mass fraction distribution was much closer to and expected r-process distribution. This highlights the importance of using updated nuclear physics data when modelling astrophysical environments. This was further reinforced when removing the outdated reaction rate data from NuGrid.

The second project then compared the use of different post processing nucleosynthesis networks for modelling different astrophysical environments. With each network adapted to have the same network limits and reaction rate libraries, differences between each network were still significant depending on the environment. Lower temperature trajectories, such as the simple hydrodynamic, weak s-process and $8 \times 10^{-5} M_{\odot} s^{-}$ produced very similar elemental mass fractions from each PPN code, with all elements greater than carbon, other than Technetium and promethium, resulting in mass fractions within an order of magnitude. The extreme temperature trajectories such as the X-ray burst, r-process and high accretion rate common envelope all saw extreme differences in at least one of the codes. SkyNet overproduced intermediate mass elements between neon and titanium when simulating an X-ray burst, but under produced elements between magnesium and tin when modelling an r-process trajectory. Clear communication between users and developers of these codes must be maintained to ensure the appropriate code is used for a chosen environment. A publication using only one code to model a scenario may come to a completely different result to another investigating the same scenario using a different code.

The final project investigated the type of nucleosynthesis that might occur inside a neutron star common envelope. The variation in angular momentum does not change the elemental or isotopic mass fraction distributions for accretion rates bellow $4 \times 10^{-5} M_{\odot} s^{-1}$. The variation in angular momentum is only seen in accretion rates that reach NSE, as shown in figures 5.28 and 5.31, as reaching NSE depends on both the time and temperature of the system and varying angular momentum varies the time spent in the accretion disk.

The smaller neutron star mass also means that the material spent less time in the accretion disk before being ejected however this does impact trajectories that do not reach NSE. For accretion rates up to $8 \times 10^{-5} M_{\odot} s^{-1}$ the boron mass fraction is consistently higher in the shorter, $2M_{\odot}$ trajectories. For trajectories that entered NSE the neutron star mass, like the angular momenta, impacts the time spent in the accretion disk and so the larger neutron star mass trajectories result in lower mass fractions of isotopes beyond Nickel as these are produced in the disk before the peak temperature.

The accretion rate feeding the disk had a substantial impact on the type of nucleosynthesis that occurred. All accretion rates greater than $64 \times 10^{-5} M_{\odot} s^{-1}$ reached temperatures and densities high enough to enter NSE. The highest accretion rates spent long enough at NSE to reach equilibrium producing identical mass fraction distributions from different neutron star masses and different angular momenta. The most varied nucleosynthesis occurred in accretion rates lower than $64 \times 10^{-5} M_{\odot} s^{-1}$. For these accretion rates the separation of the neutron star and the companion core result in material being accreted from near the hydrogen/helium boundary. Therefore, for a single accretion rate, different companions will result in different types of nucleosynthesis, as shown in the $32 \times 10^{-5} M_{\odot} s^{-1}$ accretion rate trajectory where a $15\mathrm{M}_{\odot}$ companion results in slow neutron captures, while a $20\mathrm{M}_{\odot}$ companion results in rapid proton captures. For combinations of accretion rate and companion mass and age that have initial compositions with large hydrogen mass fractions rapid proton capture occurs, this is the case for all environments for accretion rates up to $4 \times 10^{-5} M_{\odot} s^{-1}$, and in the $20\mathrm{M}_{\odot}$ environment up to $32 \times 10^{-5} M_{\odot} s^{-1}$. Neutron capture reactions occur in the accretion disk in both the 12 and $15\mathrm{M}_{\odot}$ environments for accretion rates greater than $32 \times 10^{-5} M_{\odot} s^{-1}$ however for accretion rates that reach NSE (greater than $64 \times 10^{-5} M_{\odot} s^{-1}$) the neutron rich products are destroyed to reach equilibrium. Overall the accretion disk around a neutron star inside a common envelope can produce a wide variety of different nucleosynthetic methods depending on the companion mass, age and metallicity. Low accretion rates produce very proton rich nuclei and high accretion rates result in nuclear statistical equilibrium.

Investigation into the reaction rate libraries revealed that there are still reaction rates used in post processing nucleosynthesis networks that are from outdated publications and do not use the most accurate rate, however many users of post processing codes might not be aware. Different PPN codes use different libraries, not all of which use the most up-to-date libraries available, in some cases this is a choice for backward comparisons of other variables with previous tests. However, users must be aware of which reaction rate library is in use and so communication between nuclear physicists creating the nuclear physics packages and users of network codes must be consistent for users to understand where weaknesses may occur in astrophysical modelling. Therefore, more comparisons and investigations into the impact that updated reaction rate data can have on previously studied astrophysical environments must be undertaken.

Future work should involve a sensitivity study to identify which reaction rates lead to the largest variation in isotopic distributions and consistent communication should be maintained between experimental nuclear physics and theoretical astrophysics. A project investigating how energy generated during the common envelope accretion phase must also be completed as this will be impactful for future models.

The code comparison also revealed the lack of similar studies that have been undertaken for newly developed software, with few of the previous example being [36] and [53]. NuGrid is a multipurpose code that has been used extensively since 2007, yet there are no publications comparing the results produced by NuGrid with other software. Future work should be done extending the code comparison conducted in this project to understand how the convergence methods used in each code differ.

The common envelope isotopic and elemental distributions presented in this project provide an initial step toward understanding the role of common envelopes in the broader context of galactic chemical evolution. A reaction rate sensitivity study using realistic reaction rate uncertainties should be conducted to better understand the possible variation in isotopic and elemental distribution of material ejected into the common envelope as it is unclear from this project the impact that reaction rate uncertainty may have on the resulting isotopic and elemental distributions. A subsequent population study will be required to identify the likely combinations of neutron stars and companions that lead to the formation of common envelopes and to determine the frequency of such events. Once these studies are complete, yield data can be derived and integrated with population synthesis models to assess the overall contribution of common envelopes to galactic chemical evolution.

The trajectories used in this project were designed only considering the energy contribution from the hydrodynamic process and do not include any potential contributions from nuclear energy generation. A future study investigating the energy generated during the common envelope phase should be conducted as this will influence the temperature evolution of the common envelope trajectories.

A comprehensive investigation of the full evolutionary process of a common envelope is necessary to quantify both the total mass and the composition of material ejected throughout its lifetime. This project investigated the nucleosynthesis that can occur during the slow spiral phase of the common envelope, however the wide variety of neutron star binaries that can evolve into common envelopes pose potential sites for different types of element formation during different points of their evolution.

Bibliography

[1] Benjamin P Abbott, Rich Abbott, TDea Abbott, Fausto Acernese, Kendall Ackley, Carl Adams, Thomas Adams, Paolo Addesso, Rana X Adhikari, Vaishali B Adya, et al. GW170817: Observation of gravitational waves from a binary neutron star inspiral. *Physical review letters*, 119(16):161101, 2017.

[2] E. G. Adelberger, A. García, R. G. Hamish Robertson, K. A. Snover, A. B. Balantekin, K. Heeger, M. J. Ramsey-Musolf, D. Bemmerer, A. Junghans, C. A. Bertulani, J.-W. Chen, H. Costantini, P. Prati, M. Couder, E. Uberseder, M. Wiescher, R. Cyburt, B. Davids, S. J. Freedman, M. Gai, D. Gazit, L. Gialanella, G. Imbriani, U. Greife, M. Hass, W. C. Haxton, T. Itahashi, K. Kubodera, K. Langanke, D. Leitner, M. Leitner, P. Vetter, L. Winslow, L. E. Marcucci, T. Motobayashi, A. Mukhamedzhanov, R. E. Tribble, Kenneth M. Nollett, F. M. Nunes, T.-S. Park, P. D. Parker, R. Schiavilla, E. C. Simpson, C. Spitaleri, F. Strieder, H.-P. Trautvetter, K. Suemmerer, and S. Typel. Solar fusion cross sections. II. The pp chain and CNO cycles. *Reviews of Modern Physics*, 83(1):195–245, April 2011.

[3] Carmen Angulo. NACRE: A European Compilation of Reaction rates for Astrophysics. In *Experimental Nuclear Physics in Europe: Facing the next millennium*, volume 495 of *American Institute of Physics Conference Series*, pages 365–366. AIP, November 1999.

[4] Carmen Angulo, Marcel Arnould, Marc Rayet, Pierre Descouvemont, D Baye, C Leclercq-Willain, Alain Coc, Slimane Barhoumi, P Aguer, Claus Rolfs, et al. A compilation of charged-particle induced thermonuclear reaction rates. *Nuclear Physics A*, 656(1):3–183, 1999.

[5] Georg Bader and Peter Deuflhard. A semi-implicit mid-point rule for

stiff systems of ordinary differential equations. *Numerische Mathematik*, 41(3):373–398, 1983.

[6] G P A Berg, Y Fujita, J Görres, M N Harakeh, K Hatanaka, A Long, R Neveling, F D Smit, R Talwar, A Tamii, and M Wiescher. High precision measurements for the rp-process. *Journal of Physics: Conference Series*, 387(1):012003, sep 2012.

[7] H. Bondi. On spherically symmetrical accretion. *Monthly Notices of the Royal Astronomical Society*, 112(2):195–204, 1952.

[8] Eric Burns. Neutron star mergers and how to study them. *Living Reviews in Relativity*, 23(1):4, 2020.

[9] Georgeann R. Caughlan and William A. Fowler. Thermonuclear Reaction Rates V. *Atomic Data and Nuclear Data Tables*, 40:283, January 1988.

[10] Roger A. Chevalier. Neutron Star Accretion in a Stellar Envelope. *The Astrophysical Journal*, 411:L33, jul 1993.

[11] AI Chugunov, HE Dewitt, and DG Yakovlev. Coulomb tunnelling for fusion reactions in dense matter: Path integral Monte Carlo versus mean field. *Physical Review D*, 76(2):025028, 2007.

[12] Richard H. Cyburt, A. Matthew Amthor, Ryan Ferguson, Zach Meisel, Karl Smith, Scott Warren, Alexander Heger, R. D. Hoffman, Thomas Rauscher, Alexander Sakharuk, Hendrik Schatz, F. K. Thielemann, and Michael Wiescher. The JINA REACLIB database: its recent updates and impact on type-I X-ray bursts. *The Astrophysical Journal Supplement Series*, 189(1):240, jun 2010.

[13] L Damone, Massimo Barbagallo, Mario Mastromarco, A Mengoni, L Cosentino, E Maugeri, S Heinitz, D Schumann, R Dressler, F Käppeler, et al. The ^{7}Be(n,p)^{7}Li reaction and the cosmological lithium problem: measurement of the cross section in a wide energy range at n_TOF (CERN). *Physical review letters*, 121(4):042701, 2018.

[14] Pierre Descouvemont, Abderrahim Adahchour, Carmen Angulo, Alain Coc, and Elisabeth Vangioni-Flam. Compilation and R-matrix analysis

of Big Bang nuclear reaction rates. *Atomic Data and Nuclear Data Tables*, 88(1):203–236, 2004.

[15] I Dillmann, M Heil, F Käppeler, R Plag, T Rauscher, and F-K Thielemann. KADoNiS- The Karlsruhe Astrophysical Database of Nucleosynthesis in Stars. In *Proceedings of the International Conference on Nucleosynthesis in Stars*, volume 819, pages 123–127. American Institute of Physics, 03 2006.

[16] Michal Dominik, Krzysztof Belczynski, Christopher Fryer, Daniel Holz, Emanuele Berti, Tomasz Bulik, Ilya Mandel, and R. O'Shaughnessy. Double Compact Objects I: The Significance Of The Common Envelope On Merger Rates. *Astrophysical Journal*, 759, 02 2012.

[17] Lori Downen, Christian Iliadis, Art Champagne, Thomas Clegg, Alain Coc, and Jordi José. Hydrogen Burning of ^{29}Si and Its Impact on Presolar Stardust Grains from Classical Novae. *The Astrophysical Journal*, 928(2):128, apr 2022.

[18] Urs Frischknecht, Raphael Hirschi, Marco Pignatari, André Maeder, George Meynet, Cristina Chiappini, Friedrich-Karl Thielemann, Thomas Rauscher, Cyril Georgy, and Sylvia Ekström. S-process production in rotating massive stars at solar and low metallicities. *Monthly Notices of the Royal Astronomical Society*, 456(2):1803–1825, 12 2015.

[19] Chris L. Fryer, Willy Benz, and Marc Herant. The Dynamics and Outcomes of Rapid Infall onto Neutron Stars. *The Astrophysical Journal*, 460:801, April 1996.

[20] Christopher L. Fryer, Falk Herwig, Aimee Hungerford, and F. X. Timmes. Supernova Fallback: A Possible Site for the r-Process. *The Astrophysical Journal*, 646(2):L131, jul 2006.

[21] George M Fuller, William A Fowler, and Michael J Newman. Stellar weak interaction rates for intermediate mass nuclei. III-Rate tables for the free nucleons and nuclei with A= 21 to A= 60. *The Astrophysical Journal Supplement Series*, 48(3):279, 1982.

[22] George Gamow. The quantum theory of nuclear disintegration. *Nature*, 122(3082):805–806, 1928.

[23] C. William Gear. The automatic integration of ordinary differential equations. *Communications of the ACM*, 14(3):176–179, 1971.

[24] H J Haubold and A M Mathai. The Maxwell — Boltzmannian Approach to the Nuclear Reaction Rate Theory. *Fortschritte der Physik/Progress of Physics*, 33(11-12), 1985.

[25] C. Iliadis, C. Angulo, P. Descouvemont, M. Lugaro, and P. Mohr. New reaction rate for $^{16}\mathrm{O}(p,\gamma)^{17}\mathrm{F}$ and its influence on the oxygen isotopic ratios in massive AGB stars. *Phys. Rev. C*, 77:045802, Apr 2008.

[26] C. Iliadis, R. Longland, A.E. Champagne, and A. Coc. Charged-particle thermonuclear reaction rates: III. Nuclear physics input. *Nuclear Physics A*, 841(1–4):251–322, October 2010.

[27] Christian Iliadis, John M D'Auria, Sumner Starrfield, William J Thompson, and Michael Wiescher. Proton-induced thermonuclear reaction rates for A= 20-40 nuclei. *The Astrophysical Journal Supplement Series*, 134(1):151, 2001.

[28] N. Ivanova, S. Justham, X. Chen, O. De Marco, C. L. Fryer, E. Gaburov, H. Ge, E. Glebbeek, Z. Han, X.-D. Li, G. Lu, T. Marsh, P. Podsiadlowski, A. Potter, N. Soker, R. Taam, T. M. Tauris, E. P. J. van den Heuvel, and R. F. Webbink. Common envelope evolution: where we stand and how we can move forward. *The Astronomy and Astrophysics Review*, 21(1), February 2013.

[29] N. Ivanova, Ph. Podsiadlowski, and H. Spruit. Common-Envelope Evolution: the Nucleosynthesis in Mergers of Massive Stars, 2001.

[30] Natasha Ivanova, S Justham, X Chen, O De Marco, CL Fryer, E Gaburov, H Ge, E Glebbeek, Z Han, X-D Li, et al. Common envelope evolution: where we stand and how we can move forward. *The Astronomy and Astrophysics Review*, 21:1–73, 2013.

[31] James Keegans, Christopher Lee Fryer, Samuel W Jones, Benoit Côté, Kryzstoff Belczynski, Falk Herwig, Marco Pignatari, Allison M Laird, and C Aa Diget. Nucleosynthetic yields from neutron stars accreting in binary common envelopes. *Monthly Notices of the Royal Astronomical Society*, 485(1):620–639, 2019.

[32] FG Kondev and S Naimi. The NUBASE 2016 evaluation of nuclear properties. *Chinese physics C*, 41(3):030001, 2017.

[33] K. Langanke and G. Martínez-Pinedo. Rate tables for the weak processes of pf-shell nuclei in stellar environments. *Atomic Data and Nuclear Data Tables*, 79(1):1–46, 2001.

[34] Karlheinz Langanke and G Martınez-Pinedo. Shell-model calculations of stellar weak interaction rates: II. Weak rates for nuclei in the mass range A= 45- 65 in supernovae environments. *Nuclear Physics A*, 673(1-4):481–508, 2000.

[35] Bruce Leasure, David J Kuck, Sergei Gorlatch, Murray Cole, Gregory R Watson, Alain Darte, David Padua, Utpal Banerjee, Olaf Schenk, Klaus Gärtner, et al. PARDISO. *Encyclopedia of Parallel Computing*, pages 1458–1464, 2011.

[36] Jonas Lippuner and Luke F Roberts. SkyNet: a modular nuclear reaction network library. *The Astrophysical Journal Supplement Series*, 233(2):18, 2017.

[37] B Longfellow, A Gade, BA Brown, WA Richter, D Bazin, PC Bender, M Bowry, B Elman, E Lunderberg, D Weisshaar, et al. Measurement of key resonances for the Al 24 (p, γ) Si 25 reaction rate using in-beam γ-ray spectroscopy. *Physical Review C*, 97(5):054307, 2018.

[38] R. Longland. Recommendations for Monte Carlo nucleosynthesis sampling. *Astron. Astrophys.*, 548:A30, December 2012.

[39] R. Longland, D. Martin, and J. José. Performance improvements for nuclear reaction network integration. *Astronomy & Astrophysics*, 563:A67, Mar 2014.

[40] Maria Lugaro, Marco Pignatari, René Reifarth, and Michael Wiescher. The s process and beyond. *Annual Review of Nuclear and Particle Science*, 73(1):315–340, 2023.

[41] B. Militzer and E. L. Pollock. Equilibrium contact probabilities in dense plasmas. *Phys. Rev. B*, 71:134303, Apr 2005.

[42] Matthew Ryan Mumpower, Toshihiko Kawano, TM Sprouse, N Vassh, EM Holmbeck, R Surman, and P Möller. β-delayed Fission in r-process Nucleosynthesis. *The Astrophysical Journal*, 869(1):14, 2018.

[43] Matthew Ryan Mumpower, GC McLaughlin, Rebecca Surman, and Andrew W Steiner. Reverse engineering nuclear properties from rare earth abundances in the r process. *Journal of Physics G: Nuclear and Particle Physics*, 44(3):034003, 2017.

[44] Ariadna Murguia-Berthier, Morgan MacLeod, Enrico Ramirez-Ruiz, Andrea Antoni, and Phillip Macias. Accretion Disk Assembly During Common Envelope Evolution: Implications for Feedback and LIGO Binary Black Hole Formation. *The Astrophysical Journal*, 845(2):173, 2017.

[45] N. Nishimura, R. Hirschi, T. Rauscher, A. St. J. Murphy, and G. Cescutti. Uncertainties in s-process nucleosynthesis in massive stars determined by Monte Carlo variations. *Monthly Notices of the Royal Astronomical Society*, 469(2):1752–1767, 03 2017.

[46] Takeshi Oda, Masayuki Hino, Kazuo Muto, Mariko Takahara, and Katsuhiko Sato. Rate tables for the weak processes of sd-shell nuclei in stellar matter. *Atomic Data and Nuclear Data Tables*, 56(2):231–403, 1994.

[47] B. M. Oginni, C. Iliadis, and A. E. Champagne. Theoretical evaluation of the reaction rates for $^{26}\mathrm{Al}(n,p)^{26}\mathrm{Mg}$ and $^{26}\mathrm{Al}(n,\alpha)^{23}\mathrm{Na}$. *Phys. Rev. C*, 83:025802, Feb 2011.

[48] B Paczynski. Common envelope binaries. In *Symposium-International Astronomical Union*, volume 73, pages 75–80. Cambridge University Press, 1976.

[49] Marco Pignatari and Falk Herwig. The NuGrid Research Platform: A Comprehensive Simulation Approach for Nuclear Astrophysics. *Nuclear Physics News*, 22(4):18–23, October 2012.

[50] RG Pizzone, Aurora Tumino, Scilla Degl'Innocenti, C Spitaleri, S Cherubini, A Musumarra, and S Romano. Trojan horse estimate of bare nucleus astrophysical s (e)-factor for the li (p, α) he reaction and its

astrophysical implications. *Astronomy & Astrophysics*, 438(3):779–784, 2005.

[51] Robert Popham, Stan E Woosley, and Chris Fryer. Hyperaccreting black holes and gamma-ray bursts. *The Astrophysical Journal*, 518(1):356, 1999.

[52] Thomas Rauscher and F-K Thielemann. Astrophysical reaction rates from statistical model calculations. *arXiv preprint astro-ph/0004059*, 2000.

[53] Moritz Reichert, Christian Winteler, Oleg Korobkin, Almudena Arcones, Julia Bliss, Marius Eichler, Urs Frischknecht, C Fröhlich, Raphael Hirschi, Maximilian Jacobi, et al. The nuclear reaction network WinNet. *The Astrophysical Journal Supplement Series*, 268(2):66, 2023.

[54] C Ritter, F Herwig, S Jones, M Pignatari, C Fryer, and R Hirschi. NuGrid stellar data set – II. Stellar yields from H to Bi for stellar models with MZAMS = 1–25 M$\odot$ and Z = 0.0001–0.02. *Monthly Notices of the Royal Astronomical Society*, 480(1):538–571, 06 2018.

[55] Maximilian Ruffert and Ulrich Anzer. Bondi-Hoyle accretion simulations including velocity gradients. *Astronomy and Astrophysics*, 295:108–112, 1995.

[56] A. L. Sallaska, C. Iliadis, A. E. Champange, S. Goriely, S. Starrfield, and F. X. Timmes. STARLIB: A next-generation reaction-rate library for nuclear astrophysics. *The Astrophysical Journal Supplement Series*, 207(1):18, jul 2013.

[57] H. Schatz, A. Aprahamian, V. Barnard, L. Bildsten, A. Cumming, M. Ouellette, T. Rauscher, F.-K. Thielemann, and M. Wiescher. End Point of the *rp* Process on Accreting Neutron Stars. *Phys. Rev. Lett.*, 86:3471–3474, Apr 2001.

[58] B P Singh, Manoj K Sharma, and R Prasad. Introduction to the history of nuclear reactions and motivation for this book. In *Pre-equilibrium Emission in Nuclear Reactions*, 2053-2563, pages 1–1 to 1–36. IOP Publishing, 2022.

[59] FX Timmes. Integration of nuclear reaction networks for stellar hydrodynamics. *The Astrophysical Journal Supplement Series*, 124(1):241, 1999.

[60] L Van Wormer, J Görres, C Iliadis, M Wiescher, and F-K Thielemann. Reaction rates and reaction sequences in the rp-process. *Astrophysical Journal, Part 1 (ISSN 0004-637X), vol. 432, no. 1, p. 326-350*, 432:326–350, 1994.

[61] R. V. Wagoner. Synthesis of the Elements Within Objects Exploding from Very High Temperatures. *Astrophys. J. Supp.*, 18:247, June 1969.

[62] Meng Wang, G Audi, FG Kondev, WJ Huang, S Naimi, and Xing Xu. The AME 2016 atomic mass evaluation. *Chin. Phys. C*, 41(030003):1674–1137, 2017.

[63] Y al Xu, Kohji Takahashi, Stephane Goriely, Marcel Arnould, Masahisa Ohta, and Hiroaki Utsunomiya. NACRE II: an update of the NACRE compilation of charged-particle-induced thermonuclear reaction rates for nuclei with mass number A¡ 16. *Nuclear Physics A*, 918:61–169, 2013.